THE UNIVERSITY OF CHICAGO

DEFECTS AND DYNAMICS IN BLOCK COPOLYMER THIN FILMS:

A STUDY OF POLYMER PATTERN EVOLUTION WITH

ENVIRONMENTALLY-CONTROLLED ATOMIC FORCE MICROSCOPY

A DISSERTATION SUBMITTED TO THE

FACULTY OF THE DIVISION OF THE PHYSICAL SCIENCES

IN CANDIDACY FOR THE DEGREE OF

DOCTOR OF PHILOSOPHY

DEPARTMENT OF CHEMISTRY

JONATHAN G. RAYBIN

CHICAGO, ILLINOIS

MARCH 2019

The man of science is a poor philosopher.

Albert Einstein

Table of Contents

List of Figures

List of Tables

Abbreviations

5-BSA: *5-bromosalicylic acid*

AFM: *atomic force microscopy*

AuNP: *gold nanoparticle*

AuNR: *gold nanorod*

BCP: *block copolymer*

BODIPY: *1,3,5,7,8-pentamethylpyrromethene-difluoroborate*

BT: *benzenethiol*

CTAB: *bexadecyltrimethylammonium bromide*

DSA: *directed self-assembly*

GISAXS: *grazing-incidence small-angle X-ray scattering*

LER: *line edge roughness*

LPR: *line placement roughness*

LWR: *line width roughness*

P2VP: *poly(2-vinylpyridine)*

PCC: *Pearson correlation coefficient*

PDI: *polydispersity index*

PMMA: *poly(methyl methacrylate)*

PS: *polystyrene*

PS-*b*-PMMA: *poly(styrene-block-methyl methacrylate)*

PSD: *power spectral density*

SERS: *surface-enhanced Raman scattering*

SEM: *scanning electron microscope*

SSD: *slow-scan disabled*

TEM: *transmission electron microscope*

X-PS: *crosslinked polystyrene*

Acknowledgments

I'd like to thank Steve Sibener for welcoming me into his group and for his support over the years; for genuinely understanding us, while trusting in our own abilities.

The Sibener group has been an incredibly close and one-of a-kind community. I appreciate everyone, past and present, for their endless inspiration, entertainment, and commiseration in our time spent underground: thank you to Natalie, Ying, Tuo, Mark, Jay, Gaby, Ryan, Zack, Grant, Wenxin, Tim Csernica, Kathryn, and K2. And thank you to the current group of amazing friends: Sarah Wilson, Caleb, Darren, Jeff, Rachel, Jacob, Tim, Ross, Becca, Michelle, Alli, and Sarah Brown. And, of course, Kevin Gibson for selflessly tolerating all of our late-night antics.

Thank you to Qianqian and Hyung Ju for teaching me everything I know. And to Julia who manages to alternately drive me crazy and keep me sane.

I owe much of this research to the work of our collaborators: Paul Nealey, Philippe-Guyot Sionnest, Xuanxuan, Jiaxing, Moshe, and EW.

Thank you to Qiti and Justin for keeping the AFM, SEM, and everything else running smoothly despite my best efforts. Thank you to John Phillips for supporting my "separate projects," and to Maria for keeping the group running. I am also grateful to Ka Yee Lee and Andrei Tokmakoff for taking the time to serve on my thesis committee and for their helpful comments and critique.

Outside of the group, I'd like to thank all of my friends, including the original members of Group Theory: Garret, Kevin, Philip, and Hunter. Thank you to all the other Moby Dick fans for our late-night debates. I'm also grateful for the time spent in our steadily shrinking board

game and puzzle group including Alex, Wayne, Hunter, Judith, and many others. Thank you to Taylor for always lending an ear.

Finally, I'd like to thank my family for their endless and unconditional support. Thank you to Elizabeth for appreciating and sharing grad school humor, while also modeling how to be a real grown up. And to Carolyn for proving that it is possible to do literally everything, all at the same time. Thank you to Mom for managing to make writing and editing seem inspiring, and for learning how to explain to people what I actually do. And thank you to Dad for inspiring my scientific curiosity and appreciation for the world.

Here's to many more adventures.

Abstract

The ability of block copolymers (BCP) to self-assemble into highly ordered, periodic nanostructures makes them a promising candidate for nanoscale templating applications. In recent years, the refinement of BCP processing methods has enabled the fabrication of essentially defect-free patterns on the wafer scale. However, the dynamics of BCP assembly are still poorly understood, and the most important processing steps are also the least experimentally accessible. In particular, annealing procedures, which enhance BCP mobility for structural reorganization, involve high temperatures or harsh solvent environments that hinder many analytical methods. This thesis presents research on diverse BCP systems involving several different stages of the processing pipeline. Altogether, the differing topics presented here are unified in exploring the preparation and application of BCP patterns under controlled environmental conditions *in situ* with atomic force microscopy (AFM).

On a flat surface, BCP films natively form disordered fingerprint patterns that lack long-range order. Several substrate modification strategies — collectively referred to as directed self-assembly (DSA) — may be used to control the orientation and alignment of a BCP overlayer for the preparation of controlled pattern morphologies. As part of the DSA process, thermal annealing of BCP above its glass transition temperature increases chain mobility and allows for pattern reorganization. *In situ* AFM enables the direct examination of the mechanisms and dynamics of defect healing during thermal annealing. The advent of high-speed AFM imaging has dramatically enhanced the imaging time resolution, allowing fine-grain analysis of structural intermediates in real time and space. In addition to mapping the BCP morphology, high-speed

imaging enables the direct investigation of the interfacial dynamics and the influence of single-chain dynamics.

Alongside thermal annealing, solvent treatment also facilitates polymer mobility and pattern rearrangements. Selective solvents, which have differing affinities for each of the component BCP blocks, partition into the polymer matrix and can produce diverse polymer morphologies with unique functional utility. In one example, solvent-vapor annealing selectively swells one block to produce a highly corrugated surface reconstruction. The resulting nanogrooves may then be used to template the end-to-end alignment of Au nanorods for the preparation of a molecular sensing surface. In a second experiment, BCP nanoislands act as a novel platform for the *in situ* measurement of nanoscale solvent-swelling behavior. By using the solvent as a carrier for fluorescent probes, this process offers a new, kinetically-controlled method for the localized functionalization of polymer surfaces.

Collectively, these experiments demonstrate the utility of *in situ* AFM imaging for studying otherwise inaccessible BCP dynamics, while highlighting the method's flexibility under a wide range of operational environments.

Chapter 1.

Introduction

The investigation of block copolymers (BCP), *i.e.* polymers composed of two or more covalently-linked homopolymer domains, has expanded the available landscape of soft functional materials. The synthetic flexibility of BCP chain chemistry and architecture provides control over the polymer nanostructure and, in turn, its material properties. Since 1975, BCP elastomers have found commercial applications as a synthetic rubber with the composite structure simultaneously providing favorable elasticity and stability.[1] Beyond their bulk material properties, BCPs have attracted significant attention for their native ability to self-assemble into periodic nanopatterns. Accordingly, their technological scope has significantly expanded over the past 40 years to include applications as adhesives, foams, optical gratings, and drug delivery systems.[2-4] In particular, the length scale and regularity of BCP nanopatterns have made them a promising candidate as a templating material for lithographic masks[5,6] or nanoparticle deposition.[7,8] The engineering demands for these applications have required an increased understanding of the structure/function relationships of BCP systems while inspiring interest in the development of methods for controlling their precise nanostructure.

Lithographic applications require hierarchical alignment of the BCP morphology over multiple length scales through a process known as directed self-assembly (DSA).[9] On the length scale of polymer chains, microphase separation determines the self-assembly of periodic nanostructures. Then, on the mesoscale, lithographically-engineered guiding fields are used to control long-range pattern organization. As part of this process, the BCP is annealed *via* thermal treatment or solvent exposure in order to increase chain mobility, so that patterns may access

their equilibrium geometry. Finally, the resulting BCP geometry may be used as a template or lithographic mask in order to transfer the pattern to a hard material for device fabrication.

Although these environmental processing steps are critical to pattern engineering, their role in controlling BCP pattern morphology remains poorly understood due to the experimental challenges associated with accessing extreme thermal or solvent conditions. The objectives of this dissertation are (1) to investigate BCP dynamics during the annealing process to better understand the role of DSA in defect healing and pattern evolution; and (2) to explore new methods for using the BCP nanostructure to control the deposition of functional materials.

Organization

This thesis is organized according to the hierarchical structure of the BCP patterning process as outlined in **Figure 1.1**, with the first section focusing on the alignment of the BCP film during annealing, and the second discussing potential templating applications of these films. While connected under an overarching experimental framework, each chapter may also be treated as a complete, stand-alone work. **Chapter 1** introduces background on BCPs, including defect healing and the DSA process. This introduction also includes a general overview of the experimental methods used throughout this dissertation, which should serve as a rough guide for working with environmentally-controlled atomic force microscopy (AFM). This discussion is supplemented by a closer examination within each chapter of the specific experimental methods applied. Finally, this introduction explores the impact of this research and discusses remaining questions in the field.

Chapters 2 and **3** examine BCP dynamics and pattern evolution during thermal annealing with an emphasis on the influence of DSA templating. First, **Chapter 2** follows the

Figure 1.1.
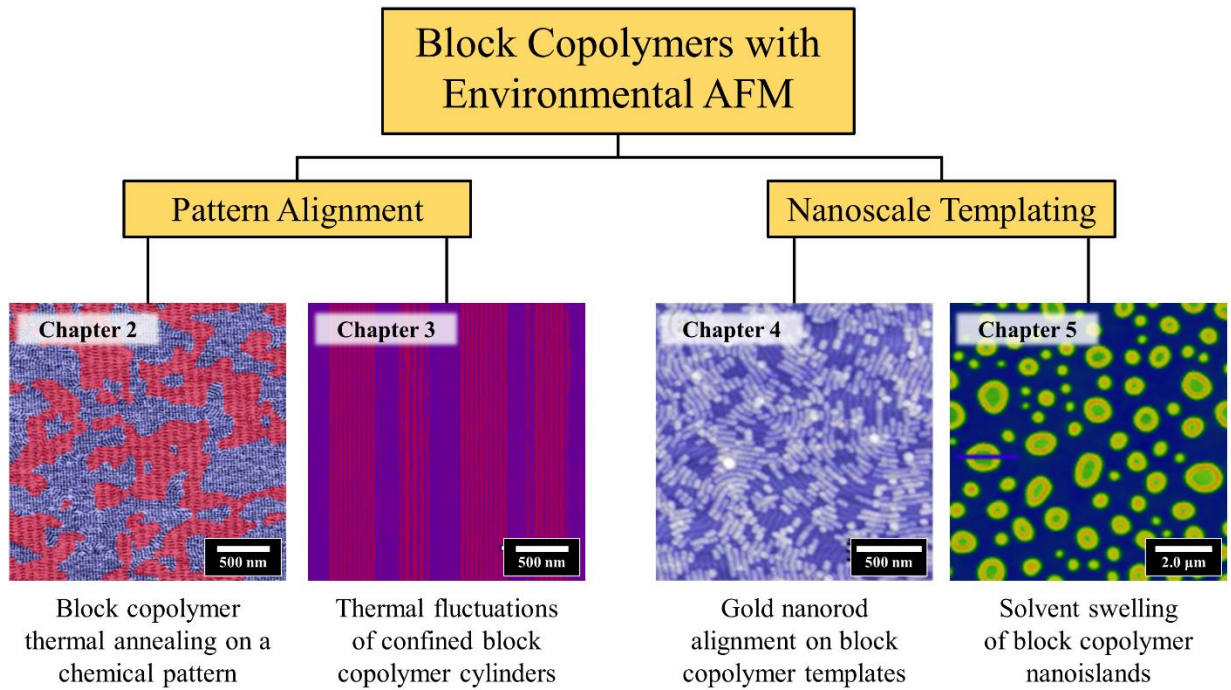
Dissertation outline. Organization of thesis topics under the framework of studying block copolymer structure and dynamics under environmental control.

kinetics of lamellar BCP organization on a chemically-patterned substrate.[10] The assembly

process is mediated by a metastable intermediate structure — coined the stitch morphology —

which determines defect-healing rates. The underlying chemical pattern modifies the potential

energy landscape, creating an accelerated and irreversible pathway to pattern alignment. Next,

Chapter 3 examines interfacial fluctuations of PS-*b*-PMMA cylinders confined in

graphoepitaxial channels. Thermal fluctuations allow the BCP pattern to explore new

connectivity maps and are an intrinsic feature of the defect-healing process. Fluctuations also

give rise to line roughness, the current limiting factor for BCP-templated lithography. By

pushing the boundaries of high-speed AFM imaging, we can use these methods to examine

dynamics on the level of a single polymer chain.

Chapters 4 and **5** discuss the application of BCP patterns as a templating material for

nanoparticles and molecular additives. In **Chapter 4**, solvent-vapor annealing is used to enhance

the corrugation of the BCP pattern.[8] The resulting nanogrooved surfaces are then used to

promote the end-to-end alignment of deposited nanorods, creating an ideal substrate for surface-

enhanced Raman scattering (SERS). The SERS response shows strong anisotropy following the

orientation of hierarchically-organized nanorods. Finally, **Chapter 5** investigates the solvent-

swelling behavior of terraced BCP films when immersed in a selective solvent and establishes a

new method for BCP surface templating. Swelling kinetics are controlled by the relaxation rate

of the BCP chains, and the mechanism is marked by a sharp solvent front. Based on these

observations, the solvent is used as a carrier for controlling the spatially-resolved incorporation

of a fluorescent laser dye.

Background

Diblock copolymers, which consist of exactly two homopolymer sub-units, represent the simplest BCP architecture. This research focuses on poly(styrene-*block*-methyl methacrylate) (PS-*b*-PMMA), depicted in **Figure 1.2.A**, due to its favorable processability and interfacial interactions. For a diblock copolymer chain with component blocks PS and PMMA, the equilibrium morphology is fully described by just three chain parameters: the degree of polymerization, N; the Flory-Huggins interaction parameter, $\chi_{PS/PMMA}$, which describes block incompatibility and segregation; and the relative volume fraction of the blocks, $f_{PS} = 1 - f_{PMMA}$.[11] By synthetically tailoring these parameters, the BCP morphology may be tuned over a range of periodic nanostructures including spheres, cylinders, gyroids, and lamellae, as illustrated schematically in **Figure 1.2.B**. This thesis exclusively examines cylinder- and lamella-forming BCP systems because they form the characteristic striped patterns useful for lithographic templating.

In the absence of external control, BCP patterns adopt a polycrystalline domain structure that lacks long-range order, as seen in **Figure 1.3.A**. This disordered, high-defect-density state is known as a fingerprint pattern. To improve global ordering, substrate modification can be used to introduce a local guiding field that breaks the symmetry of the flat silicon substrate and creates a preferred direction for alignment. This approach includes two complementary DSA strategies: graphoepitaxy and chemoepitaxy. In graphoepitaxy, depicted in **Figure 1.3.B**, the substrate is lithographically etched to produce confining trenches, and the resulting topography is used to control the orientation of polymer domains within the trenches.[12] The trench sidewalls create boundary conditions for pattern alignment across the width of the trench. In chemoepitaxy, shown in **Figure 1.3.C**, the chemistry of an underlying polymer brush pattern modulates the

Figure 1.2.
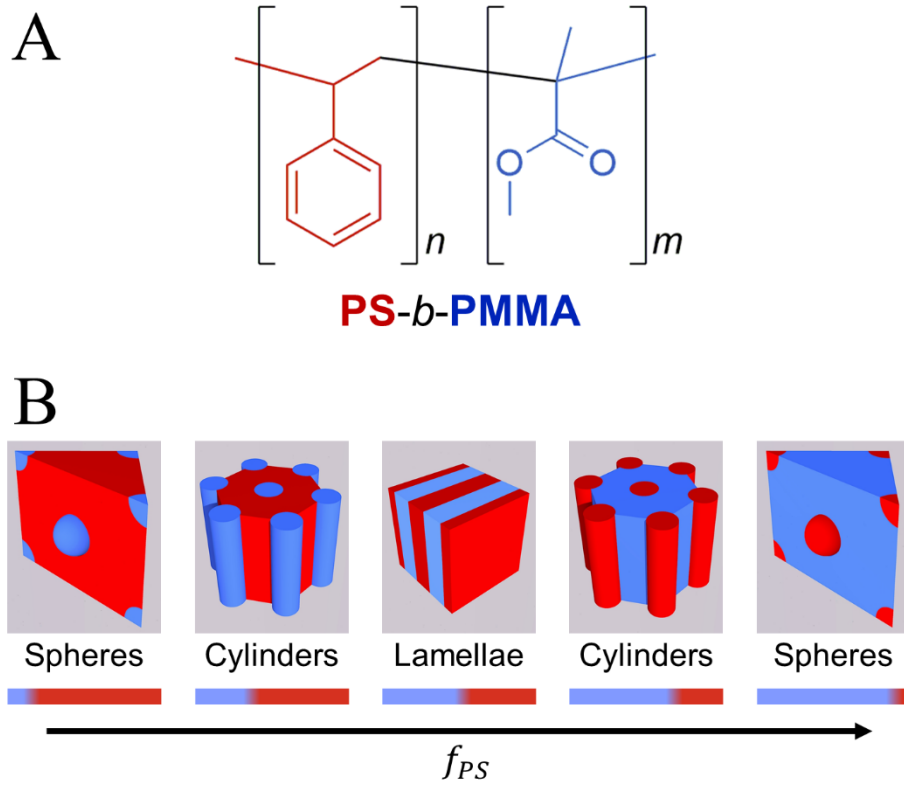
Structure and morphology of PS-*b*-PMMA. (A) Chemical structure of poly(styrene-*block*-methyl methacrylate) (PS-*b*-PMMA). (B) BCPs self-assemble to form a series of nanostructures, *i.e.* spheres, cylinders, and lamella, according to the relative volume fraction of the component blocks.

Figure 1.3.
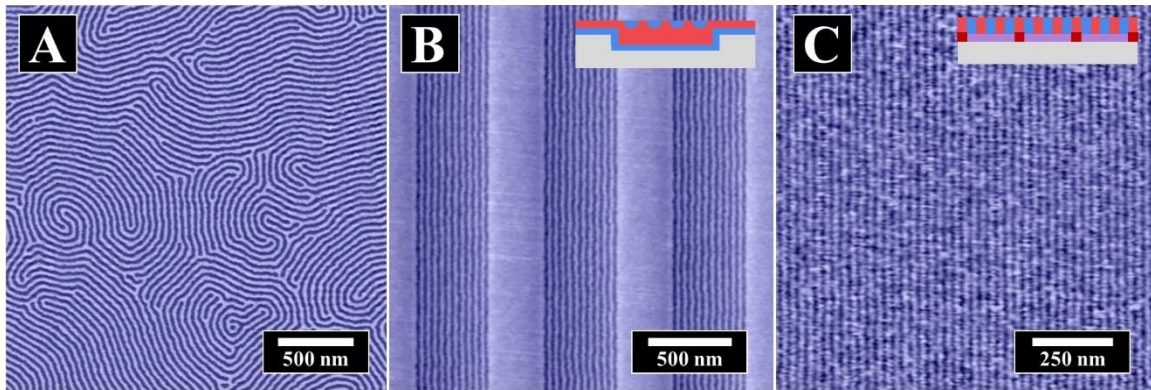
Comparison of PS-*b*-PMMA fingerprint and DSA patterning methods. (A) On a flat silicon substrate PS-*b*-PMMA self-assembles to form a fingerprint pattern that lacks long-range order. In the AFM phase image, dark stripes correspond to PMMA and light stripes to PS. (B) Confined PS-*b*-PMMA cylinders align within lithographic trenches. The inset shows a cross-sectional schematic of the substrate topography (Key: *Grey* = silicon substrate, *Blue* = PMMA, *Red* = PS). (C) On a chemically-patterned substrate, lamellar PS-*b*-PMMA orients with PS guide stripes for full-area alignment. The inset shows a cross-sectional schematic of the pattern's three-fold density multiplication (Key: *Grey* = silicon substrate, *Blue* = PMMA, *Red* = PS, *Dark red* = crosslinked PS guide stripe, *Purple* = neutral brush).

polymer/substrate interaction energy to promote a preferential BCP orientation.[9,13] The spacing

of the guide pattern is commensurate with the BCP lattice and allows for complete surface

coverage of the aligned polymer pattern. Each of these methods takes advantage of well-studied

top-down lithographic procedures to influence the bottom-up self-assembly of block copolymer

thin films. Ultimately, DSA processes have proven to be effective techniques for controlling the

structure and alignment of BCP patterns and have been used for the fabrication of nearly defect-

free patterns on the 300-mm wafer scale.[13]

By altering the potential energy landscape of polymer patterns, substrate-patterning

strategies influence both the thermodynamics and kinetics of BCP assembly. When deposited

from solution, BCP thin films initially form a kinetically-quenched, disordered state, and

additional processing is required to produce aligned patterns. Thermal annealing above the glass

transition temperature increases polymer mobility, which encourages defect healing and

coarsening of the polycrystalline domains. Alternatively, solvent treatment — either through

exposure to solvent vapor or by complete solvent immersion — may also be used to increase

chain plasticity and induce reordering. While these procedures are necessary for pattern

development, *in situ* analysis is challenging, because the required temperatures and solvent

environments remain inaccessible to most analytic techniques.

Scanning electron microscopy (SEM) is frequently used as a convenient tool for quickly

assessing the nanoscale pattern morphology, but its scope is generally limited to characterization

of the static BCP structure under vacuum. The technique is not well suited for kinetic studies as

exposure to the high-energy electron beam degrades the polymer sample and SEM chambers are

not amenable to harsh annealing conditions. Furthermore, to enhance the contrast between the

polymer blocks, pretreatment with heavy metal stains are often necessary, but this process fixes

the polymer structure in place. In recent years, tomographic SEM has been used to assess the full three-dimensional structure of BCP films.[14] The emergence of low-current imaging and ambient-environment SEM opens the possibility for kinetic experiments, but, as yet, these methods have not been applied to studying *in situ* BCP dynamics.

As an alternative method, grazing-incidence small-angle X-ray scattering (GISAXS) experiments have been used to probe the structural evolution of BCP thin films during solvent or thermal annealing. Closed solvent cells are used to isolate the film environment from the chamber and are constructed independently of the X-ray source or synchrotron. This experimental flexibility has enabled measurements of film ordering under a variety of processing conditions; this wide scope was recently demonstrated in measurements of the initial stages of microphase separation during spin-coating, a significant logistical challenge.[15] However, scattering methods provide only spatially-averaged, reciprocal-space information of the global polymer morphology. When tracking the specific healing mechanisms of individual defects, real-space imaging methods are required for locally mapping the polymer structure.

In contrast, AFM, which directly probes the polymer surface, intrinsically provides local information about the sample topography and composition. Scanning probe techniques naturally operate under ambient conditions and, using closed gas cells, may be adapted for environmentally-controlled conditions, including thermal annealing, solvent-vapor exposure, and complete solvent immersion. The Sibener group has been at the forefront of *in situ* imaging methods for the characterization of BCP dynamics and has used this method to track pattern evolution under otherwise inaccessible thermal-annealing conditions. Yufa examined the defect-healing response of a BCP thin film following surface damage by the AFM tip.[16] Building on these methods, Tong analyzed the motion and annihilation of dislocations in graphoepitaxially-

confined PS-*b*-PMMA cylinders to measure chain diffusivity.[17,18] Experiments by Ryu characterized the motion of grain boundaries to determine the mechanisms of grain coarsening and defect pinning.[19]

Although these experiments have provided the first direct insights into defect-healing mechanisms, their scope has been constrained by limited AFM time resolution. Conventional "stop-motion" AFM imaging is limited by the slow raster scan of the AFM tip, which determines a maximum data capture rate of roughly 2 min/image and prevents the acquisition of fine-grain kinetic data. However, over the course of this thesis research, the introduction of commercial high-speed AFM instrumentation has transformed the field. Engineering advances have enabled a 100-fold imaging speed increase for true video-rate AFM with image capture rates on the time scale of polymer chain dynamics.

These rate enhancements are largely based on miniaturization of the AFM sample cell and scanning probe. The maximum acquisition rate, t_{max}, of a tapping-mode AFM image is limited by the oscillation of the AFM probe and scales inversely with the cantilever's resonant frequency, f_R, as follows:

$$t_{max} \propto f_R^{-1} \qquad\qquad (1.1)$$

Improvements in AFM optics alongside developments in cantilever microfabrication have enabled the use of cantilevers with lengths as short as 35 μm with $f_R > 1$ MHz. At the same time, increased thermal stability of the AFM sample chamber has facilitated continuous, stable imaging of polymer samples for extended periods with minimal thermal drift. **Chapters 2** and **3**, which focus on dynamics during thermal annealing, take advantage of this revolution in high-speed AFM imaging to capture polymer motion in real time. These measurements provide

unique insights into the fluctuations and defect-healing processes necessary for the preparation of perfected BCP patterns.

The underlying goal of pattern alignment through DSA is to create templates for fabricating useful nanostructures. In comparison to conventional top-down lithographic methods, self-assembled BCP patterns offer enhancements in spatial resolution required for the development of next-generation electronic devices. For these applications, additional processing steps, which take advantage of native contrast in the blocks, are necessary for pattern transfer. In general, these post-processing strategies fall under two categories: (1) direct templating in which the BCP controls the deposition of functional materials; and (2) indirect templating using the BCP as a lithographic mask for transfer to the hard substrate. **Chapters 4** and **5** each explore a specific solvent-based, post-processing method for directly templating nanomaterials, with a particular emphasis on the resulting applications. In the experiments detailed in **Chapter 4**, acetic acid vapor is used to selectively swell PMMA cylinder domains to enhance surface corrugation and promote the subsequent alignment of Au nanorods.[8] In **Chapter 5**, the BCP samples are fully immersed in a selective solvent that acts as a carrier for the controlled distribution of functional materials. Indirect methods generally rely on the selective removal of one polymer block to expose and pattern the underlying substrate.[20] Selective plasma etching may be achieved either by using a natively etch-resistant inorganic block, *e.g.* poly(styrene-*block*-polydimethylsiloxane), or by later introducing inorganic material through sequential infiltration synthesis.[21] The advantages of each pattern-transfer scheme must be tuned and selected to each potential application.

Conclusions and Impact

Overall, the research in this dissertation answers fundamental questions related to BCP assembly. The following chapters include: a determination of the role of chemical templates in defect-healing kinetics; an examination of correlations between interfacial thermal fluctuations; the fabrication of SERS sensors based on hierarchically-aligned Au nanorods; and the development of a new method for controlling local functionalization of polymer surfaces. Along the way, each of these projects has sparked many new questions that hint at future potential research paths.

Since the investigation of defect healing described in **Chapter 2**, Hur *et al*. have developed simulations modeling these systems.[22] When examining the energetics of dislocation annihilation on chemically-patterned surfaces, they find that the precise location of the underlying chemical pattern modulates the potential energy landscape of defect annihilation, leading to specific trapped geometries, consistent with our measurements. Future modeling work is necessary to understand how the stitch morphology forms and to determine its role in controlling defect annihilation rates. These studies are also important to chart the limits of irreversible pattern evolution and to understand why some systems fail to overcome the kinetic barriers to alignment.

The examination of interfacial fluctuations in **Chapter 3** presents a new method for examining line roughness in BCP patterns, the current limiting factor for their industrial application as templates. This baseline study successfully demonstrates the feasibility of direct and time-resolved measurements of interfacial fluctuations at thermal-annealing temperatures but explores only the simplest case of aligned cylinders in a narrow channel. Continued work is necessary to understand the effects of the specific polymer chemistry and molecular weight to

better elucidate the connection between fluctuations and single-chain dynamics. Additionally, high-speed AFM should be used to fully map fluctuations in two spatial dimensions to chart correlations in space as well as time. Finally, it is important to analyze fluctuations in defective systems outside of equilibrium in order to understand their role in pattern alignment and defect annihilation.

Chapter 4 describes the preparation of new SERS sensing surfaces based on hierarchically-aligned Au nanorods. Since this work, these surfaces have been successfully applied for the detection of dimethyl methylphosphonate, a nerve agent simulant molecule. While this work has demonstrated the fabrication of local molecular sensors, the active area is limited to small patterned regions of the substrate. With full-area patterning methods, this sensing technique offers the potential for spatially-resolved sensing arrays.

Finally, **Chapter 5** follows the solvation kinetics of BCP islands immersed in a selective solvent. Recently, the development of direct-immersion annealing has inspired increased interest in the solvent-swelling behavior of BCP thin films for industrial processing. Solution-based processing offers a new avenue for controlling polymer morphology and is easily integrated into existing semiconductor fabrication lines. While our experiments only examine the interaction between PS-*b*-PMMA and cyclohexane, different solvents or mixtures may be chosen to tune the chemical potential and selectivity. Additionally, with improved hierarchical control over the BCP island structure and placement, it is possible to create regular arrays of nanoislands to serve as a controlled system for solvent swelling and molecular doping. The new method of kinetically-controlled doping described in **Chapter 5** tests the introduction only of fluorophore materials, but this technique may be extended for the fabrication of assays containing any soluble analyte or reactant.

Altogether, the topics included in this thesis highlight several aspects of the BCP patterning process: pattern dynamics during thermal annealing, nanorod templating, and solvent swelling. High-speed, environmentally-controlled AFM has revolutionized the ability to track pattern evolution in these selected topics and, for the foreseeable future, continues to promise exciting developments in the field at large.

Chapter 2.

Block Copolymer Thermal Annealing on a Chemical Pattern

This chapter contains an article that was reproduced in part with permission from ACS Nano.[10] Copyright 2017 American Chemical Society.

The kinetics of directed self-assembly of symmetric poly(styrene-*block*-methyl methacrylate) (PS-*b*-PMMA) diblock copolymer on chemically-patterned templates is measured during *in situ* thermal annealing. Although these chemical guide patterns lead to well-aligned, defect-free lamellar patterns at thermodynamic equilibrium, in practice, challenges remain in understanding and optimizing the kinetic evolution for technological applications. High-speed, environmentally controlled atomic force microscopy (AFM) imaging is used to track pattern evolution on the time scale of individual microdomain connections in real space and time allowing direct visualization of defect-healing mechanisms. When we apply this highly general technique to films on chemically-patterned substrates, we find that pattern alignment is mediated by a metastable non-bulk morphology unique to these samples — referred to as the "stitch" morphology. Through this local analysis, we observe diverse and anisotropic mechanisms for the conversion from this morphology to equilibrium lamellar stripes. Directed self-assembly (DSA) on chemical templates is observed to follow exponential kinetics with an effective energetic barrier of 3.5 eV, a significant enhancement when compared with ordering rates on unpatterned substrates. Ultimately, we find that the chemical guiding field facilitates *irreversible* morphological ordering and lamellar alignment for the rapid development of perfected patterns.

INTRODUCTION

The self-assembled, nanoscale patterns of block copolymers (BCP) have long been viewed as an attractive platform for fabricating semiconductor devices.[5,6,11,23] Nanoscopic control over polymer morphology is necessary to achieve the levels of registration and perfection required for such processes, and a variety of strategies have been developed for this purpose. Generally, these techniques break the in-plane symmetry of BCP films, either through the application of external long-range fields (such as shear flow[24] or electric fields[25,26]) or locally through substrate modification, in order to enforce a single preferred orientation.

DSA methods — which use lithographically-defined templates with chemical contrast (chemoepitaxy)[9,27] or topographical features (graphoepitaxy)[12] — dictate the orientation of a BCP overlayer and have been demonstrated to yield large-scale single-crystalline microphases with lower defect densities than long-range alignment strategies.[28,29] DSA patterns may achieve smaller features than conventional top-down lithographic templates through pattern multiplication.[9]

For DSA to be successfully implemented in high-volume semiconductor manufacturing, defect annihilation kinetics must be able to achieve defect levels of $0.01/cm^2$ within process-friendly timescales. Molecular simulations have determined that observed defect structures are not thermodynamically favorable but rather represent non-equilibrium structures that are kinetically trapped.[30,31] In BCP thin films, a single dislocation has a free energy excess of $\Delta F \sim 100\ k_B T$ over the aligned structure, where k_B is the Boltzmann constant and T is temperature. This large thermodynamic excess is derived from the collective strain of the many individual polymer chains participating in the defect.[32] The annihilation of even simple, single-domain defects involves the formation of a series of transition states that constitute an uphill thermodynamic

16

barrier. For more complex defects that involve multiple domains, the thermodynamic landscape becomes increasingly complicated and intermediate structures are more likely to remain trapped in a defective state. To understand the formation and annihilation of defects, in this chapter, we probe the evolution of BCP structures on DSA chemical patterns during thermal annealing through in situ high-speed AFM imaging.

Many studies have investigated the kinetics of annealing of BCP thin films. Grazing-incidence small-angle X-ray scattering (GISAXS) experiments have observed microphase separation and phase transitions during solvent vapor annealing.[33,34] Still, GISAXS scattering patterns reflect global morphological changes and cannot distinguish local defect structures. *Ex situ* imaging methods have examined pattern development following arrested annealing intervals, revealing a $t^{1/4}$ power law for the growth aligned grains with annealing rates sensitive to the BCP chemistry and architecture.[35-37] *In situ* AFM combines the advantages of each of these methods and has been used to trace the kinetics of BCP pattern evolution, including film healing,[16] defect annihilation rates,[17,18] and grain coarsening.[19] Despite their success in tracking BCP dynamics, previous AFM imaging experiments have been limited by slow scan rates and therefore lacked sufficient time resolution to map the dynamics of pattern evolution on the time scale of individual domain linkages and disconnections. However, recent advances in high-speed AFM imaging have revolutionized the field, and here we demonstrate the ability to track polymer evolution in real time and space to elucidate specific defect annealing mechanisms.

We have used environmentally-controlled in situ AFM to continuously trace the evolution of polymer structure during thermal annealing in real time, **Figure 2.1.A-F**. These AFM micrographs reveal the progression of the polymer morphology toward alignment, in which we observe three distinct and hierarchical processes: (1) microphase separation, (2)

17

Figure 2.1
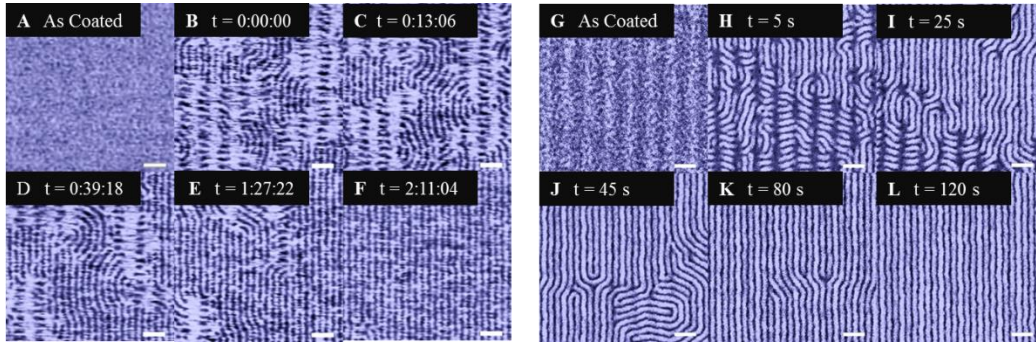
Polymer alignment on a chemical guide pattern. (A-F) AFM time series phase images of lamella-forming PS-b-PMMA films on a chemical guide pattern as cast (A) and captured throughout *in situ* thermal annealing at 210 °C (B-F). Dark domains correspond to PMMA and light domains correspond to PS. (G-L) SEM images showing a series of lamella-forming PS-*b*-PMMA samples as cast (G) and following discrete thermal annealing intervals at 250 °C (H-L). The contrast is inverted in SEM images; dark domains correspond to PS and light domains correspond to PMMA. Scale bars are 100 nm.

morphological stitched-to-perpendicular lamellar ordering, and (3) lamellar alignment. The first step, microphase separation of the PS and PMMA blocks, occurs rapidly, before we have begun imaging at 210 °C and is not captured here. (Thermal drift prevents stable imaging during the initial temperature ramp.)

Initially following microphase separation, the polymer has not yet fully adopted the perpendicular lamellar morphology, as illustrated in **Figure 2.2.A**. Instead, images show the coexistence of a second morphological phase, termed the "stitch" morphology, **Figure 2.2.B** — characterized by short PMMA stitches in a PS matrix to the chemical guide pattern — alongside the perpendicular lamellar morphology. The stitch morphology forms a regular pattern that includes columns of orthogonal stitches spaced by columns of lamella oriented parallel to the substrate. This morphology does not correspond to a classical bulk equilibrium BCP phase and instead reflects a metastable superstructure of perpendicular and parallel lamella unique to thin films on chemically-patterned substrates. Consequently. the stich morphology's energetics is governed by the relative periodicities of the guide pattern and epitaxial film.

As annealing continues, perpendicular lamellar grains coarsen and stitched grains shrink. Concurrently, defects, including dislocations and disclinations, in the lamellar grains annihilate, yielding a well-aligned film after roughly 135 min of annealing at 210 °C. The final equilibrium patterns have a pitch of 28 nm, consistent with three-fold pattern multiplication on the 84 nm templates.

The regions of perpendicular lamella and stitch phases may be easily distinguished in AFM images due to their distinct surface patterns. PS composes a larger fraction of the atmospheric interface for the stitch morphology, $f_{PS,stitch} = 72\%$, than for the perpendicular

Figure 2.2
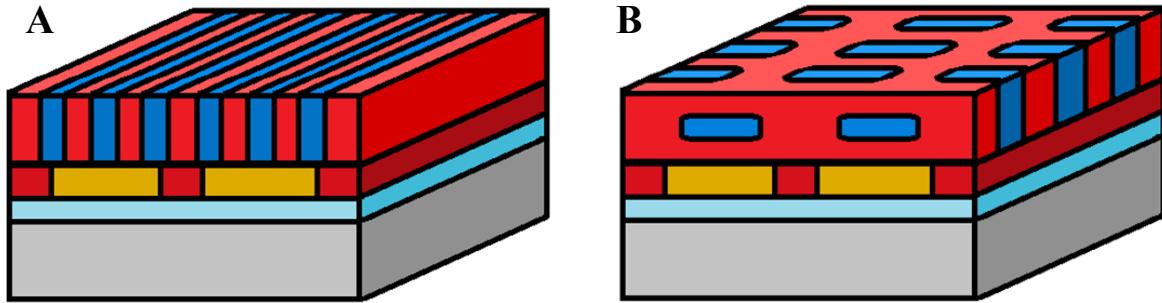
BCP morphologies on a chemical guide pattern. Schematic cross-sections of the thin-film morphology. (A) The lamellar morphology aligned epitaxially with the underlying PS guide stripes. (B) The metastable "stitch" morphology, a superstructure of lamella parallel and perpendicular to the substrate that is commensurate with the DSA pattern (Key: *Grey* = silicon substrate, *Red* = PS, *Blue* = PMMA, *Dark red* = crosslinked PS guide stripe, *Yellow* = neutral polymer brush, *Light blue* = native silicon oxide).

lamellar phase, $f_{PS,\perp lam} = 47\%$, which suggests that the stitch phase includes the formation of parallel lamella with PS at the top surface. We note that surfaces of perpendicular lamella in misaligned regions have comparable PS coverage to aligned lamellar structures despite their high defect densities. Although the Flory-Huggins interaction parameters of PS and PMMA with air are very similar at the annealing temperatures, the atmospheric interface has a slight PS preference, which may play a role in stabilizing the stitch morphology.[38]

We repeated these thermal annealing experiments at 250 °C to achieve industrially relevant conditions. However, pattern evolution progressed too quickly to be captured by *in situ* AFM imaging. Instead, we examined a series of samples with truncated annealing times and imaged the samples with scanning electron microscopy (SEM), **Figure 2.1.G-L**. Under these conditions, a similar morphological progression was observed at faster time scales. Initial microphase separation occurred rapidly, within 5 s at 250 C. We again observe the coexistence of stitched and perpendicular lamellar phases for annealing times under 25 s. Many in-plane lamellar defects persisted following the complete conversion of stitched grains, but continued thermal treatment yielded uniform perpendicular lamella and ultimately a well-aligned, low-defect structure within 2 min.

While SEM imaging confirms the overall progression of thermal annealing, these *ex situ* studies are necessarily discontinuous and each measurement must probe a separate sample. High-speed *in situ* AFM complements SEM analysis by enabling direct monitoring of polymer morphologies in a single region in real time. Furthermore, AFM imaging is completely nondestructive, whereas electron beam exposure during SEM imaging causes sample damage including backbone fragmentation and crosslinking.

Figure 2.3
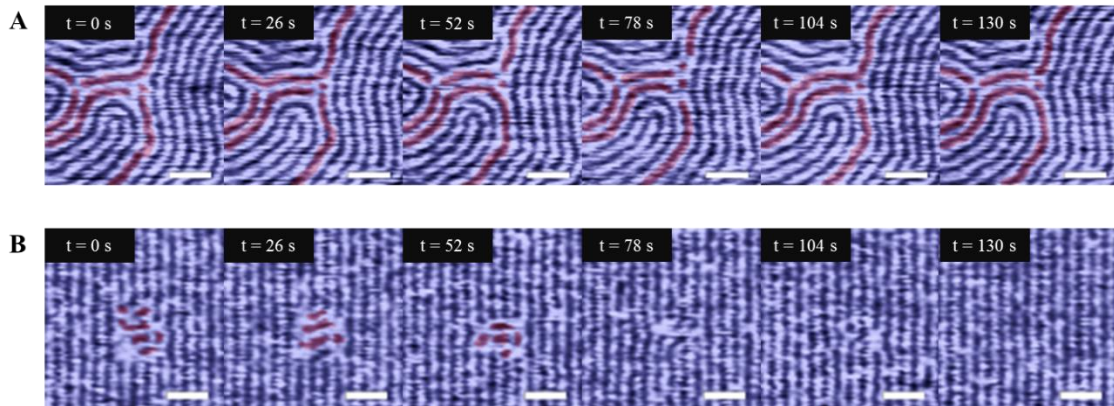
Annealing and irreversible alignment. (A) A time sequence at 26 s intervals of AFM images of lamella-forming PS-*b*-PMMA on a random brush substrate during *in situ* thermal annealing at 210 °C shows disconnections and reconnections of strained domain junctions. Red highlights are included for clarity. (B) A time sequence of symmetric PS-*b*-PMMA on a chemically-patterned substrate under identical annealing conditions shows the conversion of a short stitched domain, highlighted in red, to aligned perpendicular lamella. Scale bars are 100 nm.

As a point of comparison, we also tracked the dynamics of lamellar films on unpatterned substrates, shown in **Figure 2.3.A**. A random copolymer brush that is non-preferential toward PS and PMMA ensured the lamella would be oriented perpendicular to the interface.[39] In the absence of an external field, the pattern exhibits a polycrystalline grain structure with high defect density — a characteristic "fingerprint" pattern. As expected, no stitch phase was observed on the flat substrate, as the stitch morphology arises due to the influence of the chemically-patterned template. Thermal annealing of fingerprint patterns under the conditions and timescales used for patterned substrates showed minimal grain growth or overall ordering.

During the thermal annealing of unpatterned substrates, we witnessed frequent microdomain disconnections and reconnections in regions along the boundaries of orientational grains. The lamellae at grain junctions, highlighted in red for clarity, experience conflicting alignment stresses from the neighboring grains. In this isotropic substrate environment, there is no strong thermodynamic preference toward a unique lamellar orientation and the polymer may adopt any morphology from an array of nearly degenerate states. The polymer microdromains in these regions stochastically samples this selection of possible states. We note that domain evolution is reversible, as the pattern frequently backtracks to previously explored states, slowing the development of larger, well-aligned grains. Within the 2 min time period depicted, only minimal changes to the overall connectivity have occurred and the grain sizes have not changed. In these measurements, as with all of our experiments, AFM imaging may only probe lamellar connectivity at the surface. Previous tomographic analysis of these sites has shown similar variation in domain connectivity below the surface while suggesting a more complex three-dimensional structure.[14]

In contrast, polymer films on patterned templates rapidly converge onto a single thermodynamic minimum state. Figure **2.3.B** follows the complete conversion and alignment of a short column of stitched domains. These frames depict a polymer sample at the same temperature and over the same time period as the unpatterned sample shown in Figure **2.3.A**. Similar microdomain disconnection and reconnection events occur allowing the pattern to sample different connectivity states. In contrast to the unpatterned samples, however, the neighboring aligned lamella and the underlying chemical pattern provide stable boundary conditions for the stitched grains that direct alignment of the polymer and facilitate the elimination of defects. Only a single aligned lamellar orientation is thermodynamically favored. Strikingly, the strong thermodynamic gradient provides an irreversible path to alignment; on chemical patterns, we never observed aligned lamella reverting to misaligned or stitched domains. This result offers experimental confirmation for earlier simulation predictions that DSA establishes a significantly lower free energy for the aligned state such that the alignment process is irreversible.[30] The irreversibility of defect removal is crucial for DSA to be able to achieve the low defect level demanded by advanced lithography applications.

The kinetics of conversion from the stitch morphology is fundamental to understanding the organization of films on chemical patterns. This process is of particular interest because it appears to limit the overall alignment rate of the film. While the stitched-to-perpendicular lamella conversion process initially yields films with a high defect density, most of these lamellar defects are resolved before the stitch morphology has fully converted. In this manner, the energetics of the stitch phase mediates the overall alignment.

We therefore examined the kinetics of this morphological transition more closely. The stitched and lamellar domains initially form a bicontinuous two-dimensional network. Over time,

Figure 2.4
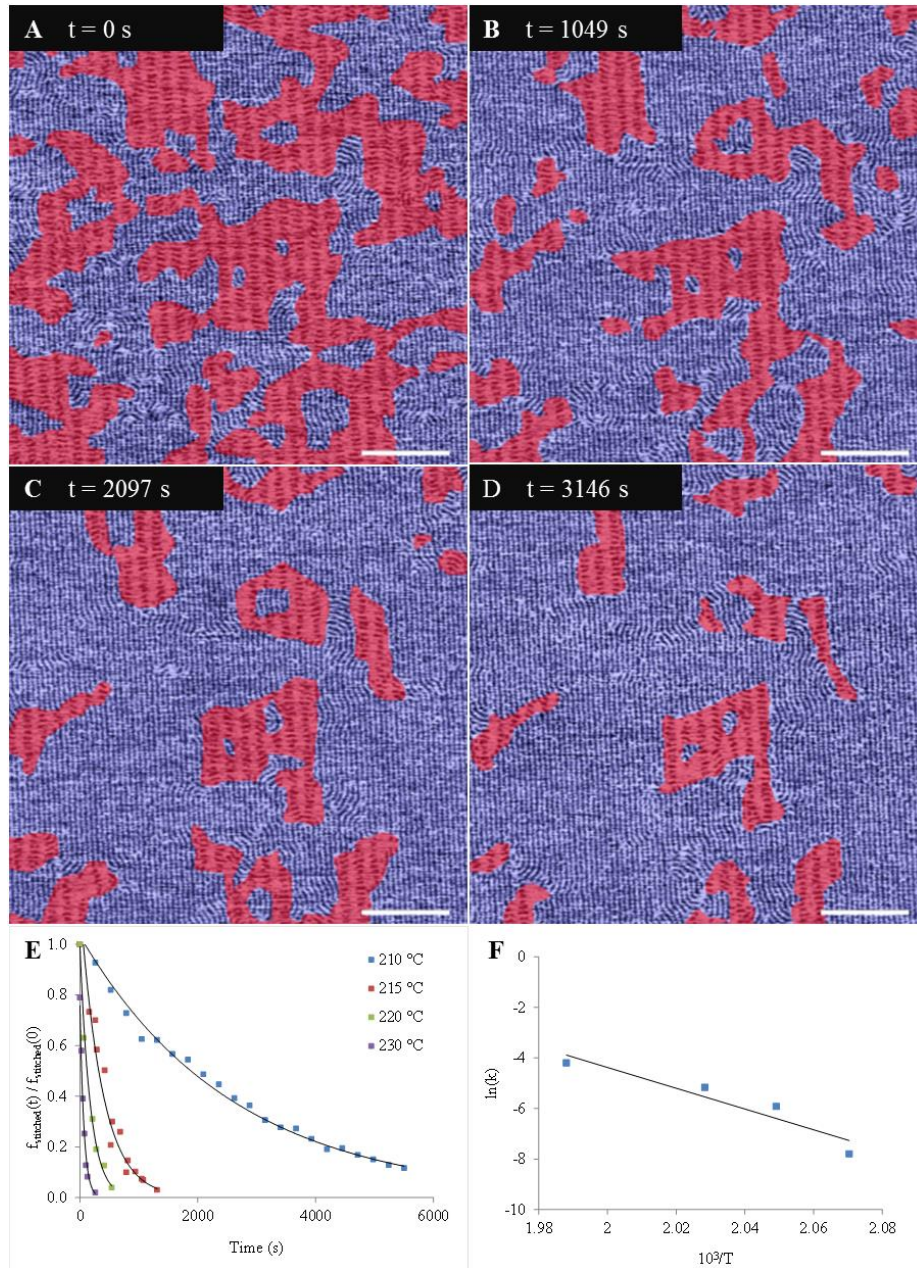
Time evolution of the stitch morphology. (A-D) AFM images of the PS-*b*-PMMA during *in situ* thermal annealing at 210 °C analyzed for kinetic data. The stitched domains have been highlighted in red. Scale bars are 500 nm. (E) The area fraction of the stitched domains plotted over time for several temperatures and fit by single exponentials curves. (F) An Arrhenius plot of the exponential rate constant plotted against temperature, yielding an effective energetic barrier of 3.5 eV.

the area of the stitched regions (marked in red in **Figure 2.4.A-D**) decreases, reducing its surface coverage and leaving disconnected grains. When annealing at 210 °C, surface coverage data could be closely fit to a single exponential decay with time constant τ = 2440 s.

$$\frac{f_{stitch}(t-t_0)}{f_{stitch}(t_0)} = e^{-(t-t_0)/\tau} \tag{2.1}$$

This exponential dependence represents a significant rate enhancement over the $t^{1/4}$ power laws governing the grain growth of unpatterned films.[35] We repeated these measurements over a series of temperatures, finding thermally activated Arrhenius kinetics with an effective energetic barrier of E_a = 3.5 eV or roughly 80 $k_B T$ at experimental temperatures. As observed in our AFM movies, defect annealing does not follow a singular topological mechanism and cannot be described by a unique potential energy surface. As such, this value reflects an average effective barrier for the chain reorientation of PS and PMMA domains into forming perpendicular lamellae, the molecular process common to each of these mechanisms.

As noted above, alignment requires the subsequent reorganization and annihilation of defects in the resulting lamellar microstructure. The high defect density of these films during the early stages of thermal annealing provides ample opportunities to study the annihilation of different defect structures. In most cases lamellar defects reorganized more quickly than the stitched-to-perpendicular lamellar conversion, but longer-lived structures occasionally formed depending on the local defect environment. Notably we observed differences in the resulting lamellar conformation dependent on the direction of grain growth during the stitched-to-perpendicular lamellar conversion.

When stitches were converted to lamella orthogonal to the direction of the guide stripe, as shown in **Figure 2.5.A**, grain growth proceeded by one stitched column at a time (corresponding to one guide pattern period). First, stitches adjacent to the grain boundary rotate to form aligned

Figure 2.5
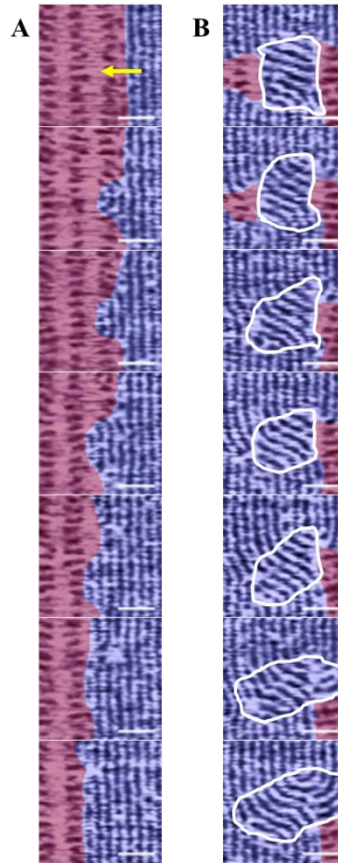
Stitched-to-aligned lamella conversion mechanisms. (A) Time series, ordered top-to-bottom with time intervals of 130 s, depicting grain growth during the stitched-to- perpendicular lamellar transition at 210 °C. Stitch domains are highlighted in red. The lamellar grain growth (yellow arrow) progresses orthogonal to the underlying guide pattern and occurs one stitched column at a time. (B) Time series, ordered top-to-bottom with time intervals of 260 s, at 210 °C in the presence of misoriented perpendicular lamellar grains (white bordered regions). When stitches initially connect between columns, misoriented grains form and coarsen that hinder the direct formation of fully aligned patterns.

lamellar segments. The short new lamellae then extend upwards and downwards to produce an entire aligned column. When the lamellae meet other aligned regions, the new stripes then directly connect to form continuous aligned domains without the formation of intermediate defect states. After the complete conversion of one stitched column, the end state is self-similar to the starting conditions, and the process may be repeated. In particular, we note that this grain growth mechanism provided a direct path to lamella with robust alignment, bypassing the late-stage lamellar alignment processes.

However, in other cases stitched columns may connect directly with each other rather than with neighboring lamellar domains as shown in **Figure 2.5.B**. This leads to grain growth parallel to the direction of the guide stripe. The stitched columns connect to form lamellar segments orthogonal to the underlying guide pattern. When aligned lamellae connect with misoriented segments they yield curved domains which ultimately form disclinations, an example of which is shown at the end of the time series in **Figure 2.5.B**. Disclinations were stabilized by the neighboring stitched morphology and were generally observed to persist as longer-lived structures at 210 °C following complete stitched-to-perpendicular lamella conversion. Although we witnessed many examples of the two cases pictured in **Figure 2.5**, in practice the conversion process is highly dependent on the local defect structure and often follows a combination of the mechanisms described here.

Misregistration of the lamellar stripes within domains, *i.e.* the case of aligned lamella breaking translational symmetry, also yields single dislocation defects, as highlighted in **Figure 2.6.A**. Lamellar misregistry extends across multiple domains connecting spatially separated defect sites. Dislocations are attracted to grain boundaries and defects of opposite orientation and will travel orthogonally across the lamellar pattern — a process known as dislocation glide. An

Figure 2.6
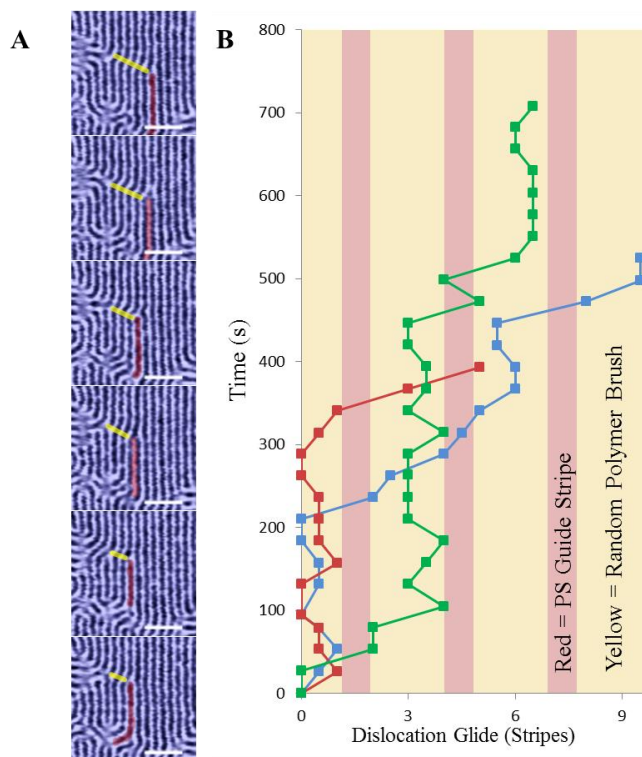
Punctuated dislocation mobility. (A) Time series of AFM images at 215 °C showing dislocation glide across six lamellar lines in intervals of 26 s. The dislocation is highlighted in red for clarity. Yellow traces indicate lines of lamellar misregistration. Scale bars are 100 nm. (B) A plot of dislocation trajectories over time at 215 °C for three dislocation glide events in units of lamellar stripes. The blue trace includes the dislocation pictured in (a). Background coloring indicates the locations of the PS guide stripes (red) and the random polymer brush (yellow) in the underlying DSA pattern. Dislocation motion is punctuated, and dislocations are observed to be predominantly trapped over the random polymer brush regions.

example of dislocation motion is shown in the time series of **Figure 2.6.A**. Ultimately, the sequential motion of the dislocation across the substrate corrects the misregistry in its wake and produces a well-aligned film, and when two opposite dislocations meet they will annihilate.

In contrast to previous studies of dislocation mobility on unpatterned substrates,[24] we observed that dislocation motion was not a continuous process. Instead transits were punctuated by long stationary periods of up to 20 min before rapidly gliding to a new site. Several dislocation trajectories are recorded in **Figure 2.6.B**. Transit distances were measured to follow multiples of three lamellar periods, distances commensurate with the underlying guide pattern of our three-fold pattern multiplication samples. When compared with the placement of the chemical guide pattern, stationary dislocations were predominantly found to reside above the centers of non-preferential brush regions of the guide pattern, indicated by the yellow banded regions in **Figure 2.6.B**.

For DSA with pattern multiplication, the lamellar stripes above the crosslinked PS regions of the guide pattern are directly aligned by the pattern; the interpolated lamellae are instead indirectly aligned by neighboring lamellar stripes. In this manner, punctuated dislocation mobility reflects the periodic potential energy surface produced by the underlying chemical guide pattern, whereas continuous mobility on graphoepitaxial substrates is governed exclusively by the long-range attraction of the opposing dislocation cores. Dislocation residence times varied dramatically, suggesting that the energetics of the trapping sites is highly dependent on the local defect structure. However, these observations emphasize the importance of guide patterning in governing the dynamics of epitaxial alignment.

In summary, we have directly observed the kinetic mechanism for DSA of block copolymers on chemical patterns. Our local AFM measurements provide local measurements of

defect ordering mechanisms that are complementary to previous globally averaged measurements by GISAXS. The chemical pattern hastens alignment to a single-crystal domain and, critically, this process was observed to occur irreversibly. On patterned substrates, ordering followed a single exponential rate law with an effective energetic barrier of 3.5 eV. Persistent defects were frequently observed to arise as the result of conversion from a metastable stitch morphology, which plays a crucial role in mediating the assembly process. In seeking to prevent defect nucleation, the design of chemical DSA templates must consider not only their role in shaping the final equilibrium state, but also their impact on the energetics of these metastable intermediate phases.

METHODS

Chemically-patterned substrates were prepared on a TEL CLEAN TRACK ACT™12 system at IMEC in Leuven, Belgium, following previously reported methods.[40] The template consisted of crosslinked polystyrene (X-PS, AZEMBLY NLD-128) guiding stripes that were preferential for the PS domains and non-preferential background regions filled with end-grafted PS-*r*-PMMA random copolymers (AZEMBLY NLD-127). The periodic X-PS guiding stripes had a pitch of 84 nm and each stripe was 8 nm in height and 20 nm in width. The background random copolymer was 6 nm thick, so there was minimal topographic contrast with the guiding stripes.

Unpatterned substrates were coated with a uniform layer of non-preferential PS-*r*-PMMA polymer brush (AZEMBLY NLD-127) with a thickness of 6 nm. A 35 nm-thick layer of lamella-forming PS-*b*-PMMA (AZEMBLY PME-312) was then coated on both types of substrates. This polymer was selected to form structures with three-fold pattern multiplication on our chosen templates. *In situ* experiments used samples as cast with no prior annealing. An Asylum Cypher ES AFM was used for *in situ* real-time imaging while heating the samples at temperatures between 210-230 °C with heating rates of 2 °C/s. Gold-coated Arrow UHF cantilevers were purchased from NanoWorld and had resonant frequencies of 1.2-1.6 MHz. *Ex situ* thermal annealing was performed by heating on a hot plate at 250 °C under nitrogen environment for a series of time intervals and rapidly quenching down to room temperature. Scanning electron microscopy was performed on a Carl Zeiss Merlin SEM.

Chapter 3.

Thermal Fluctuations of Confined Block Copolymer Cylinders

Using environmentally-controlled, high-speed atomic force microscopy (AFM), we examine dynamic fluctuations of topographically-confined poly(styrene-*block*-methyl methacrylate) (PS-*b*-PMMA) cylinders. Fluctuations are fundamental for driving domain alignment and give rise to the intrinsic roughness of block copolymer patterns, the current limiting factor for lithographic applications. Whereas previous investigations have examined polymer roughness in room temperature and kinetically quenched samples, we directly visualize the dynamics of PS/PMMA interfaces in real space and time at *in situ* temperatures above the glass transition temperature, T_g. Interfacial fluctuations increase in intensity with temperature and, at high temperatures, become spatially coherent across their confining potential. Additionally, we observe that topographic confinement suppresses fluctuations in the proximity of the guiding field. Through the use of slow-scan-disabled AFM, which dramatically improves the imaging time resolution, we achieve scan rates that match the time scale of single-chain polymer dynamics. From spectral analysis of the time-resolved fluctuations, we find a transition between this bulk, coherent behavior at long time scales and single-chain dynamics at short time scales, from which we identify chain diffusion constants. *In situ* imaging at annealing temperatures represents a significant step in capturing the statistical mechanics of chain mobility at block copolymer interfaces.

INTRODUCTION

The length scale and regularity of self-assembled block copolymer (BCP) patterns makes them attractive candidates for next-generation lithographic and templating applications.[5,11] BCP films natively self-assemble to form periodic nanostructures, including spherical, cylindrical, gyroid, and lamellar phases.[41,42] This self-assembly process is thermodynamically driven by microphase separation of the polymer domains as governed by χ, the Flory-Huggins interaction parameter between polymer segments. Strongly-segregated BCPs produce well-defined features that may be transferred onto hard substrates for subsequent lithographic processing. While the dimensions of BCP domains are favorable for device applications, in the absence of an external guiding field, the patterns lack long-range order and form a randomly oriented fingerprint-like pattern. Traditional top-down lithography can be used to engineer the polymer substrate, through processes known as directed self-assembly (DSA), to create local fields for controlling domain orientation and alignment. Chemical[9,43] or topographic[12,44,45] templates induce the organization of globally ordered BCP nanostructures, advantageous for both device fabrication and for creating stable environments to study BCP assembly. Graphoepitaxial control using topographically-patterned substrates, as shown in **Figure 3.1.A**, enforces the alignment of confined polymer cylinders using the trench sidewalls as well-defined boundary conditions.

DSA-templated systems have been extensively studied with a focus on producing long-range domain alignment[19,47,48] and removing point defects.[18,30,49] Concerted effort by the DSA community has resulted in the realization of single-crystal, essentially defect-free BCP thin films on the 300-mm wafer scale.[13,48] Nevertheless, even with perfect domain connectivity and control over defect density, structural disorder remains a limiting factor for the feasibility of BCPs as a technology for patterning semiconductor devices.[50-52] The intrinsic pattern roughness due to bulk

34

Figure 3.1
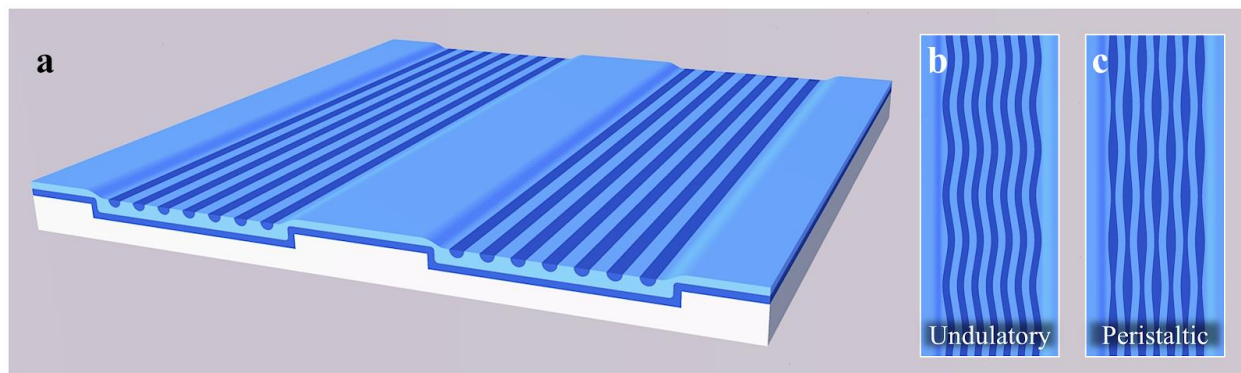
Oscillation modes of confined PS-*b*-PMMA cylinders. (A) Schematic of aligned PS-*b*-PMMA cylinders confined within lithographic trenches. Dark blue corresponds to PMMA and light blue to PS. Cylinder fluctuations are described in terms of coherent (B) undulatory and (C) peristaltic modes.

composition fluctuations in segregated polymer domains[53-55] is enhanced by thermally excited interfacial dynamics.[56,57] Measurements of the resulting line roughness parameters — categorized as edge roughness, placement roughness, and width roughness (abbreviated LER, LPR, and LWR) — exceed the maximum benchmarks for disorder set by the International Technology Roadmap for Semiconductors.[58] In an effort to achieve these targets, researchers have developed a variety of models and experimental methods to fully characterize line roughness, including its spatial correlation and spectral dependence. Stein *et al*. compared the use of soft X-ray diffraction and scanning electron microscopy as tools for non-destructively measuring domain roughness, which they modeled as interfacial capillary waves.[57] Further investigation by Bosse employed computer-simulated phase-field models to track the effects of temperature, segregation strength, and confinement on roughness.[59-61] In his theoretical treatment of confined BCP ordering, Bosse demonstrated that the line-edge roughness (LER) power spectra of lamellar-forming BCP can be modeled with a two-term expression that includes the contributions of interfacial thermal capillary wave fluctuations and bulk composition fluctuations.[61] Ruiz *et al*. adapted Bosse's expression for LER by modifying the description of interfacial dynamics to include a set of undulatory and peristaltic modes, as shown in **Figures 3.1.B** and **C**.[62] These modes correspond to line-placement roughness (LPR) and line-width roughness (LWR), respectively, following a phenomenological description used for bilayer membranes. Additionally, while traditional imaging techniques are limited to the polymer surface, several experiments have investigated interfacial fluctuations in three dimensions — through modeling of the reciprocal space signal with X-ray diffraction[63,64] and in real space with transmission electron microscope tomography[14] — to develop a complete, through-film description of roughness and to characterize the effects of substrate interactions.

36

The previously described experimental studies examined roughness in systems cooled below the glass transition T_g, *i.e.* at temperatures where dynamic fluctuations are quenched. While low-temperature analysis can quantify residual spatial roughness, these methods are limited to static systems and cannot separate the effect of fluctuation damping during the cooling process. Measurements above T_g are essential for directly visualizing the dynamics of BCP patterns, which, alongside domain fluctuations, include defect healing[16-18,65] and domain alignment.[10,19] Using *in situ* AFM heating techniques, several groups have independently investigated the behavior of interfacial fluctuations during thermal annealing. Tsarkova *et al.* observed periodic undulations of domain boundaries and found qualitative correlations between the fluctuations of adjacent domains.[66,67] When studying the formation and growth of BCP microdomains, Yufa *et al.* measured spatiotemporal autocorrelation of the interdomain boundary structure and observed an interfacial restoring force resulting from curvature minimization.[68]

Recent advancements in high-speed AFM have significantly improved instrumental stability and imaging rates, enhancing our ability to track domain fluctuations.[69] Together, these developments allow us to achieve sufficient fidelity to spatially and temporally characterize interfacial dynamics with a complete description of the BCP structure during the thermal annealing process. In this chapter, we apply *in situ* AFM imaging to measure fluctuations in topographically-confined cylinder-forming poly(styrene-*block*-methyl methacrylate) (PS-*b*-PMMA). For the first time, we are able to capture polymer dynamics on the time-scale of single-chain fluctuations. The aligned BCP cylinders act as a controlled environment for analyzing disorder under varying experimental conditions, including temperature and confinement strength. Ultimately, this method provides direct experimental insight of BCP fluctuations in real time and

real space, illuminating their contribution to interfacial roughness, defect healing,[16] and pattern aging.[70,71]

RESULTS AND DISCUSSION:

SSD Imaging

To optimize our time resolution, images are acquired in the slow-scan-disabled (SSD) AFM mode. An example SSD AFM image is shown in **Figure 3.2**, in which the slow-scan axis is disabled midway through the AFM scan, as indicated by the white horizontal line. The AFM phase image shows aligned PS-*b*-PMMA cylinders within a topographic trench flanked by two neighboring regions of unconfined fingerprint pattern; the PS and PMMA domains appear as light and dark blue, respectively. Above the dividing line, **Figure 3.2** shows a conventional AFM image, as collected over a two-dimensional surface raster. Then, after the slow-scan axis is disabled, the AFM probe begins to continuously trace over the same line of the sample along the *x*-axis, enabling rapid sampling of a single one-dimensional cross section of the surface. With this technique, the *y*-axis of the image becomes time, while, as usual, the *x*-axis indicates the lateral position of the probe. With typical high-speed AFM imaging under our experimental conditions, a full image with 512 lines takes 25 s. By disabling the slow-scan axis, the effective time resolution is enhanced to 0.05 s, while still fully capturing the dynamics of a single cross section.

An SSD image including aligned polymer cylinders in four lithographic trenches is shown in **Figure 3.3.A**. The PS and PMMA domains have strong contrast in the phase ϕ due to differences in energy dissipation at the AFM tip, allowing us to distinguish between the two blocks.[65] Peaks and valleys in ϕ, shown in **Figure 3.3.B**, correspond to the PS matrix and PMMA cylinders, respectively, in the image cross-section, marked as a line scan in **Figure 3.3.A**. We

38

Figure 3.2
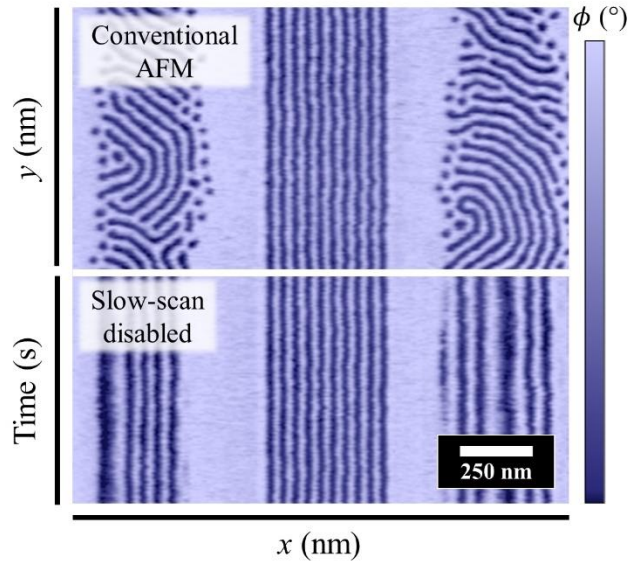
Slow-scan-disabled AFM imaging. AFM phase channel image of aligned PS-*b*-PMMA cylinders within a topographic trench, with surrounding regions of unconfined fingerprint pattern; the PS and PMMA domains are light and dark blue, respectively. The slow-scan axis is disabled midway through the scan, as indicated by the white horizontal line, and the *y*-axis becomes time while the *x*-axis remains the lateral position. Disabling the slow-scan axis increases the effective sampling time resolution to 0.05 s.

identify the domain interfaces as the points of greatest change in phase, determined from the extrema of the first-derivative signal $\Delta\phi/\Delta x$. Gaussian fits to these peaks are then used to precisely locate edge positions. Each guiding trench contains seven PMMA cylinders, indexed i = 1 to 7, and each has two corresponding domain interfaces, with positions $e_{i,n}$, where $n = L$ or R denote the left and right edges. We obtain the cylinder placement p_i from the average of the left and right edge positions and the width w_i from the edge separation:

$$p_i = \frac{1}{2}\left(e_{i,L} + e_{i,R}\right); \quad w_i = \left(e_{i,R} - e_{i,L}\right) \tag{3.1}$$

Roughness

In the strong-segregation limit, the interdomain boundary has a finite width where the composition continuously transitions between PS and PMMA.[54,72] When examined in systems quenched below T_g, the block composition varies along the boundary resulting in spatial roughness. The line roughness, which may be categorized as LER, LPR, and LWR, is the current limiting factor for achieving the precise registry standards for semiconductor device fabrication. Above T_g, the interface is dynamic and is continuously modulated by fluctuations; these fluctuations, in turn, contribute to the pattern roughness. While thermal annealing conditions are difficult to access experimentally, the temporal fluctuations are directly visible with high-speed AFM imaging.

Our *in situ* measurements of the interfacial position allow precise determination of each of the roughness parameters. Each SSD image includes 512 linescan traces, which together produce a time-resolved trajectory of the fluctuations for each the PS/PMMA interfaces $e_{i,n}(t)$. The position of the i-th interface fluctuates from its average, with residual:

$$\delta e_{i,n}(t) = e_{i,n}(t) - <e_{i,n}> \tag{3.2}$$

Figure 3.3
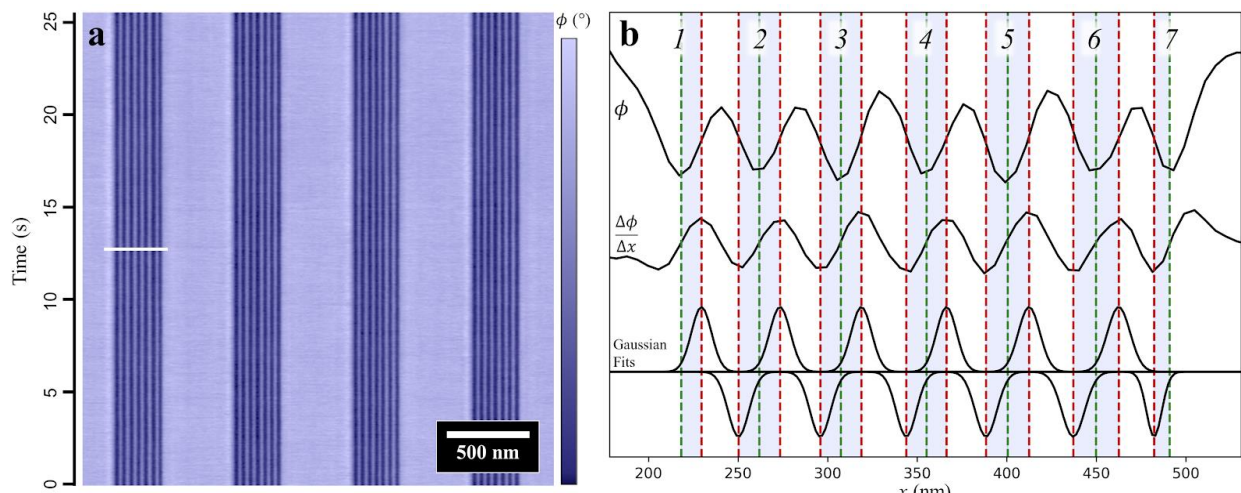
Edge measurements in SSD AFM images. (A) SSD AFM phase channel image of aligned PS-*b*-PMMA cylinders in a confining trench. Phase contrast distinguishes PS (light blue) and PMMA (dark blue). Because the slow-scan axis is disabled, the *y*-axis of the image measures time. A phase ϕ cross section of the seven cylinders, marked as a white horizontal line across the first trench, is plotted in (B). The $\Delta\phi/\Delta x$ derivative curve and associated Gaussian fits are used to determine the position of cylinder edges (dashed red lines), placements (dashed green lines), and widths (blue shaded areas). The left- and rightmost interfaces are not fit, as maxima are poorly defined at the trench sidewalls.

where $<\cdot>$ represents the time average. These terms are illustrated in a schematic in **Figure 3.4.A**. From the edge trajectories we obtain the corresponding placement $p_i(t)$ and width $w_i(t)$ time series for each cylinder, with residuals:

$$\delta p_i(t) = p_i(t) - <p_i>; \quad \delta w_i(t) = w_i(t) - <w_i> \tag{3.3}$$

The fluctuations for each term are observed to be normally distributed about their equilibrium values, as shown in **Figures 3.4.B-D**. Following convention, LER is defined as the third standard deviation of the edge position:

$$3\sigma_e = 3 <\delta e_{i,n}(t)^2>^{1/2} \tag{3.4}$$

Similar definitions are used for the LPR and LWR:

$$3\sigma_p = 3 <\delta p_i(t)^2>^{1/2}; \quad 3\sigma_p = 3 <\delta p_i(t)^2>^{1/2} \tag{3.5}$$

Roughness is conventionally determined from the spatial variation along pattern stripes, but here we measure LER, LPR, and LWR from the distributions of the time-resolved ensemble.

LPR and LWR are not independent variables, but rather are linked by their definitions in Equation (3.1), and they are related to LER as:

$$\sigma_p{}^2 = \frac{1}{2} \sigma_e{}^2 (1 + c); \quad \sigma_w{}^2 = 2 \sigma_e{}^2 (1 - c) \tag{3.6}$$

where c is the linear correlation coefficient between adjacent edges under the assumption that the edge roughness is consistent across each cylinder. The value of c varies between -1 (total negative correlation), 0 (no correlation), and 1 (total positive correlation). We note that in Equation (3.6) positive correlation enhances LPR, while negative correlation enhances LWR. In BCP patterns, polymer chain connectivity and incompressibility lead to coherence between the interfacial positions, and we anticipate positive values for c.[73]

Figure 3.4
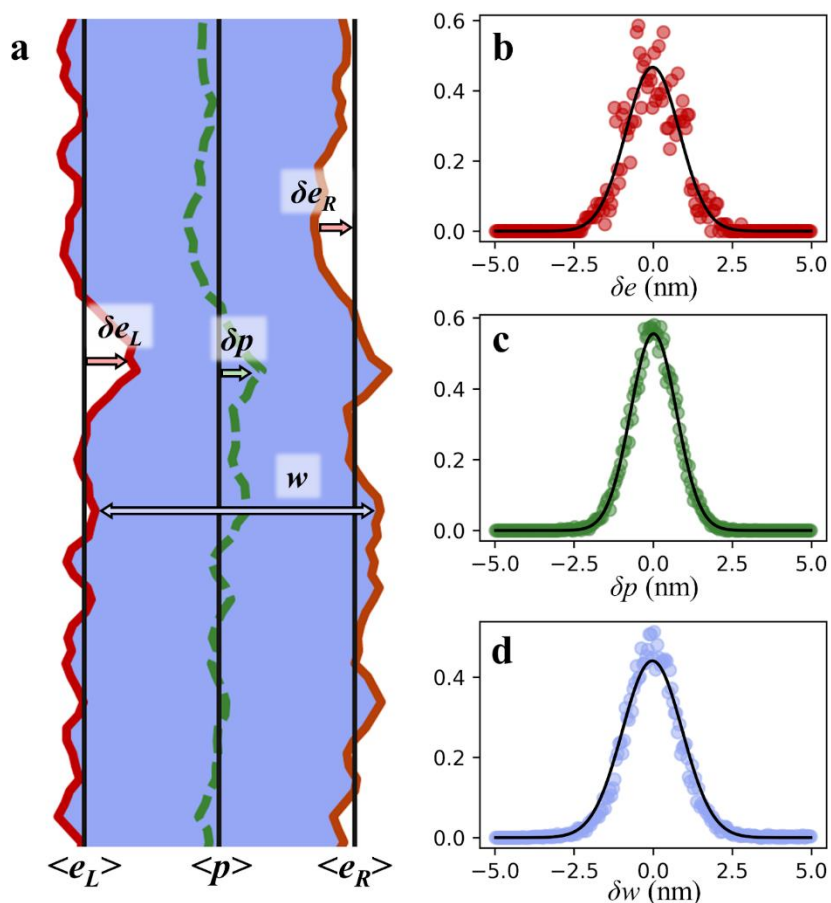
Line roughness parameters. (A) Schematic including definitions for cylinders edges, <e>, placements, <p>, and widths, <w> averaged over time and their residuals δe, δp, and δw. (B-D) Measurements at 150 °C of the respective residuals (red, green, and blue points) for each of these parameters, follow Gaussian distributions (black fit lines).

To understand the effect of the confining potential, we consider LER ($3\sigma_e$), LPR ($3\sigma_p$), and LWR ($3\sigma_w$) as a function of domain position. We find that each of the roughness parameters is enhanced with increasing distance from the trench sidewalls at 240 °C, as shown in **Figure 3.5.A**. The sidewalls act as external guiding fields and suppress interfacial fluctuations of the sidewall-adjacent cylinders ($i = 1, 7$).[60,74] At the center of the trenches, polymer domains are insulated from the hard sidewall by neighboring cylinders and experience a local environment that more closely resembles unconfined polymer, leading to increased roughness. Interestingly, we measure a consistent value of $c \sim 0.78$ at 240 °C, suggesting that the enhanced roughness does not result from changes in interfacial correlations. This finding contrasts with phase-field simulations of confined polymer in which Bosse identified damping of the interface-interface covariance in the proximity of the guiding field.[60] This discrepancy arises because we examined PMMA cylinders, as opposed to the two-dimensional and fully symmetric patterns studied in Bosse's simulations. Cylinders act as incompressible units which have uniformly high interfacial correlation and are therefore less susceptible to the influence of the guide pattern. We also note that, with similar analysis at lower temperatures, we do not observe trends in either roughness or the correlation c as a function of channel position. Below 240 °C, PS has a lower surface energy than PMMA, and the air interface acts as a hard surface which may dampen roughness uniformly across the trench.[75] A complete list of values for $3\sigma_e$, $3\sigma_p$, $3\sigma_w$, and c as a function of channel position are collected in **Table 3.1**.

Our use of *in situ* AFM allows us to directly measure LER, LPR, and LWR at a series of temperatures above T_g: 150, 200, 210, 220, 230, and 240 °C, as plotted in **Figure 3.5.B**. Cylinders adjacent to the trench sidewalls are excluded from this analysis to control for confinement effects. Roughness parameters, based on averages over multiple cylinders and from

Figure 3.5
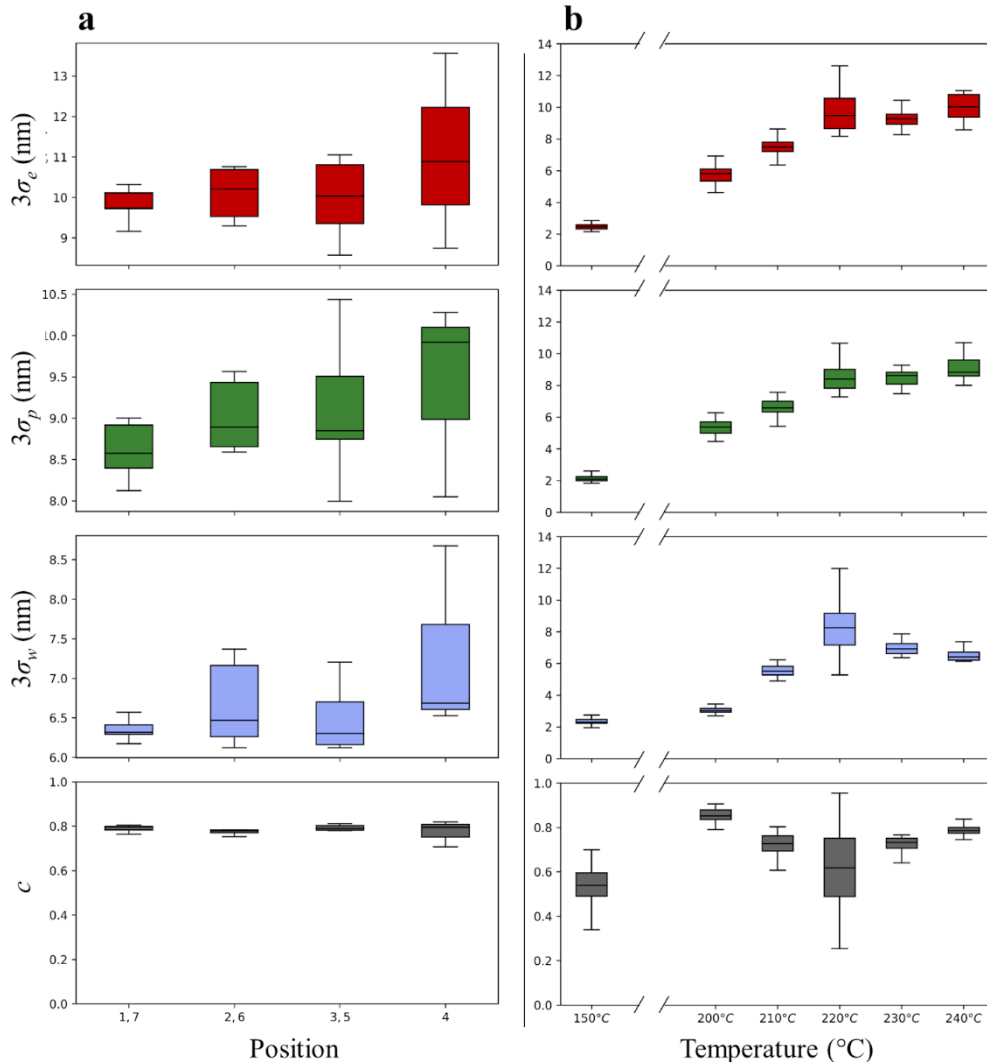
Line roughness trends. (A) Box plots showing the median and distribution of measured roughness parameters at 240 °C. Roughness varies between cylinders at sidewall positions ($i = 1$, 7) and those at central positions ($i = 4$). LER ($3\sigma_e$) and LPR ($3\sigma_p$), and LWR ($3\sigma_w$) are suppressed adjacent to sidewalls, where fluctuations are pinned by the confinement potential. The edge-edge covariance c is constant across the trench. (B) Box plots comparing roughness measurements across temperatures of 150, 200, 210, 220, 230, and 240 °C. Roughness initially increases with annealing temperature and saturates above 220 °C. The value of c increases above 150 °C but varies due to measurement uncertainty. To control for confinement effects, cylinders at sidewall positions ($i = 1$, 7) are excluded from the temperature series data.

multiple experiments at each temperature, initially increase with temperature and saturate above 220 °C. Roughness initially increases due to an enhancement of thermal fluctuations alongside an accompanying decrease in the domain segregation strength. Above 220 °C, we find limiting values of $3\sigma_e \sim 10$ nm, $3\sigma_p \sim 9$ nm, and $3\sigma_w \sim 7$ nm. In our system, the range of cylinder positions is constrained by the confining trench, which determines an upper limit for LER and LPR, while LWR is limited by chain length and domain incompressibility.

Over the temperatures surveyed, we measure positive values for c in the range $c \sim 0.5$ to 0.9. At 150 °C, where fluctuations are relatively small, dynamics at one interface have a minor influence on neighboring interfaces, and we measure $c = 0.54 \pm 0.10$. Above 150 °C, coherence helps accommodate the strain of increased fluctuations, leading to a general increase in the value of c. However, we see large variation in c between temperatures that can be partially attributed to uncertainty in the edge measurements. Imaging noise results in apparent decorrelation and causes the value of c to regress to the mean, as is particularly evident at 220 °C. Mean values for $3\sigma_e$, $3\sigma_p$, $3\sigma_w$, and c as a function of temperature are collected in **Table 3.2**.

When interpreting these values, we note that AFM imaging is limited to measuring the structure and roughness of the BCP pattern at the atmospheric interface, and we therefore expect our analysis to overestimate roughness. At the free surface, the polymer forms a melt-like layer with increased chain mobility, leading to heightened fluctuations.[76-78] Three-dimensional surveys of BCP interfaces have confirmed that surface roughness is enhanced with respect to the bulk.[14,63]

Table 3.1

Roughness versus channel position. LER, LPR, LWR, and edge-edge covariance of confined cylinders as a function of position within the channel.

Position (at 240 °C)	$3\sigma_e$ (nm)	$3\sigma_p$ (nm)	$3\sigma_w$ (nm)	c
1, 7	9.8 ± 0.4	8.6 ± 0.3	6.4 ± 0.1	0.79 ± 0.01
2, 6	10.5 ± 1.3	9.2 ± 0.7	6.9 ± 0.9	0.78 ± 0.03
3, 5	10.0 ± 0.9	9.1 ± 0.8	6.5 ± 0.4	0.79 ± 0.02
4	11.1 ± 2.0	9.4 ± 1.0	7.3 ± 1.0	0.77 ± 0.05

Table 3.2

Roughness versus annealing temperature. LER, LPR, LWR, and edge-edge covariance of confined cylinders as a function of temperature during thermal annealing.

Temperature (°C)	$3\sigma_e$ (nm)	$3\sigma_p$ (nm)	$3\sigma_w$ (nm)	c
150	2.5 ± 0.2	2.1 ± 0.2	2.4 ± 0.2	0.54 ± 0.10
200	5.8 ± 0.5	5.4 ± 0.4	3.1 ± 0.2	0.86 ± 0.03
210	7.7 ± 1.7	6.8 ± 1.2	5.7 ± 1.5	0.72 ± 0.05
220	10.2 ± 2.5	8.6 ± 1.3	8.4 ± 1.7	0.60 ± 0.22
230	9.3 ± 0.6	8.5 ± 0.5	7.0 ± 0.4	0.72 ± 0.04
240	10.3 ± 1.3	9.1 ± 0.8	6.7 ± 0.7	0.78 ± 0.03

Spatial Correlation

The long-range coherent behavior of the striped pattern may be described by a continuum model in which cylinder motion is coupled by a set of collective undulatory and peristaltic modes, depicted schematically in **Figures 3.1.B** and **C**. LPR is directly associated with cylinder undulations; LWR is similarly associated with peristalsis, but is also influenced by bulk composition fluctuations.[62]

Heretofore, we have only examined the correlations between adjacent interfaces across a PMMA cylinder. We generalize our previous analysis to include long-range correlations using Pearson correlation coefficients (PCC) to identify correlations for a pair of edges *i,n* and *j,m*:

$$\rho_e(i, n; \, j, m) = \frac{cov(e_{i,n}(t), \, e_{j,m}(t))}{\sigma_e(i,n) \, \sigma_e(j,m)} \tag{3.7}$$

where cov($\cdot$) is the covariance and e(i,n) is the standard deviation of the *n*-th edge of the *i*-th cylinder. This generalization allows us to measure the extent of lateral correlation across a trench. PCC values range from -1 (negative correlation) to 1 (positive correlation). **Figure 3.6** shows a set of correlation matrices comparing the positions of cylinder edges, placements, and widths over a temperature series of 150, 210, and 240 °C. In the PCC matrices, each matrix element compares the position of a reference cylinder to that of another cylinder in the trench. Our experiments comprise large datasets including multiple trenches imaged over time, and each matrix element is colored according to the average PCC value for a given pair of cylinders. At 150 °C, N_{points} = 129,024 for widths and placements (doubled for edges); at 210 °C, N_{points} = 186,368; and at 240 °C, N_{points} = 28,672. The matrices are symmetric, and diagonal elements have an autocorrelation of unity. Collectively, these plots reveal trends in fluctuation intensity and correlation as functions of temperature and domain separation.

Correlations of edge fluctuations are shown in **Figure 3.6.A**. Over this series, we observe that the strength and extent of spatial correlations are enhanced with increasing temperature. At 150 °C, adjacent domains, which are offset by one from the matrix diagonal, show positive correlations, while more separated domains show weaker correlations. Increasing the temperature to 210 °C, we find that the intensity of the positive correlations strengthens and that the range of coherence increases to include most of the trench, while still smoothly decreasing with separation. Finally, at 240 °C robust, positive correlations extend fully across the trench, indicating strong coupling between the confined cylinder edges. As confirmation that this analysis serves a true measure of coherence in domain fluctuations, we compared cylinders in separate trenches in the same SSD AFM line scans and observed no correlated behavior. While edge correlations are consistently positive, the intensity of correlations between adjacent cylinders is observed to modulate between alternating edges: edges that span PMMA domains ($n = L \rightarrow R$) show a stronger correlation than those across PS domains ($n = R \rightarrow L$). The effect is most apparent when examining the adjacent off-diagonal terms in **Figure 3.6.A** at 150 °C. With increasing temperature, the intensity difference between alternating matrix elements narrows as the system becomes globally coherent. The contrast arises because the longer-chain PS domains have greater configurational flexibility, and elastic deformation of the majority block more effectively screens interfacial correlations. The PMMA cylinders are comparatively inflexible, leading to stronger edge correlation. The predominant stable mode of our system is characterized by undulations of the minority-block PMMA cylinders in the PS matrix.[79]

Next, in **Figure 3.6.B**, we examine correlations between cylinder placements, which are directly related to undulatory oscillatory modes. The motion of placements is positively correlated, *i.e.*, as one cylinder oscillates, its neighbors move in the same direction. At 150 °C,

Figure 3.6
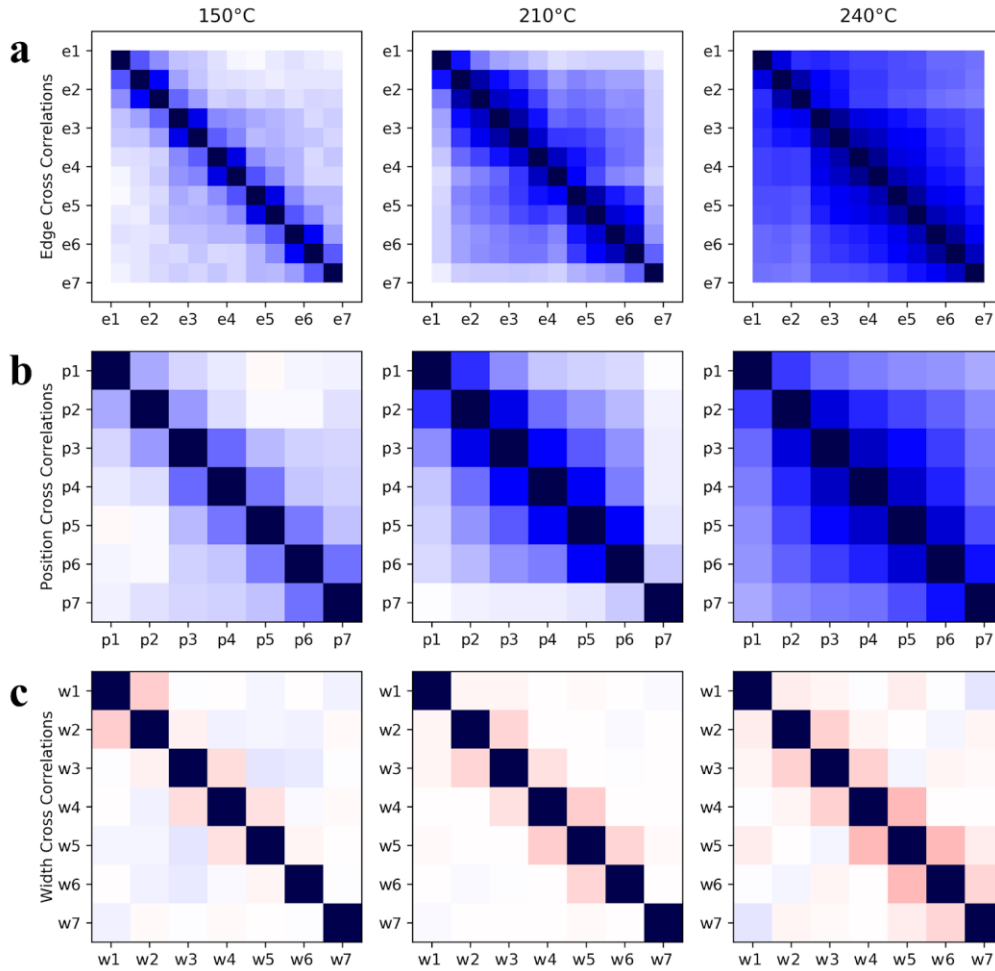
Spatial correlation matrices. (A) PCC matrices show cross correlations of edge positions across the trench at 150, 210, and 240 °C. Each matrix element is colored according to the PCC value for a pair of edge residuals $\delta e_{i,n}$ and $\delta e_{j,m}$. The matrices are symmetric, and diagonal elements have an autocorrelation of 1. At 150 °C, the edge displacements of adjacent cylinders show positive correlation, and the correlation strength decreases with separation. As the temperature is increased to 210 and 240 °C, the magnitude and range of correlations increase to extend across the trench. The left- and rightmost edges, which were not directly fit, are not included in the matrices. (B) PCC matrices of cylinder placements at 150, 210, and 240 °C. At 150 °C. The positive correlation is observed between the placements of adjacent cylinders, which weakens with large separations. With increasing temperature, the range and magnitude of placement correlation increases to extend across the trench, which we associate with coherent undulatory modes. (C) PCC matrices of cylinder widths at 150, 210, and 240 °C. Minimal correlation is observed at 150 °C, while at higher temperatures the widths of adjacent cylinders become negatively correlated. The range of the width anticorrelation, which is associated with peristaltic modes, does not extend beyond adjacent cylinders.

we observe weak positive correlation between nearest neighbors, which further weakens between more distant cylinders. Then, at 210 °C we find a significant increase in the strength of placement correlations that propagate throughout the cylinders in the trench. However, we observe that the coherence of cylinders along the trench edge positions, $i = 1, 7$, is damped. Finally, as with edge correlations, we find complete coherence of cylinder placements at 240 °C. These correlations arise from in-phase behavior and correspond to collective undulating motion. The similar trends between edge and placement are expected because placements are determined from the numerical average of directly adjacent edges, which are observed to be positively correlated in all temperatures surveyed.

Correlations between cylinder widths, shown in a set of PCC plots in **Figure 3.6.C**, are comparatively weak due to the strong coherence of adjacent edges. At 150 °C, we see minimal correlations between cylinder widths at any separation. With increasing temperature, at 210 °C we observe anticorrelation between adjacent cylinders with no long-range coupling. The correlation strength of adjacent cylinders is further increased at 240 °C, but the correlation range does not increase. Due to coupling of peristaltic modes, extension of one domain induces compression in its neighbors. Global coherence is mitigated by the contribution of local, independent composition fluctuations to width variation.[54] We observe that the magnitude of the anticorrelation at 210 and 240 °C is suppressed for cylinders $i = 1, 7$, due to interactions with the trench sidewalls.[48,60]

Due to the BCP microstructure, interfacial fluctuations are inherently structurally anisotropic. Our SSD measurements, which show long-range coherence, only examine behavior perpendicular to the cylinder alignment. Previous studies have found that small-angle fluctuations in BCP patterns form anisotropic grains oriented orthogonally to BCP pattern.[71,80]

Although inaccessible to our one-dimensional measurement technique, we expect a shorter length scale for correlations along the axis parallel to the stripes, which have a wavelength on the order L_0.

As an additional visualization of fluctuation correlation, sets of pairwise distributions of edge displacements are collected in hexagonally-binned, two-dimensional histograms, shown in **Figure 3.7**, for a series of domain separations (1st, 2nd, and 3rd order) and temperatures (150, 210, and 240 °C). Each histogram corresponds to a collection of cylinder pairs with uniform domain separation, as indicated by the colored diagonal lines in the associated PCC matrices. From the variance and shape of the distributions, we obtain information on both fluctuation intensity and coherence. The initially tight clustering at 150 °C is indicative of small fluctuations, but, with increasing temperature, the distribution broadens as fluctuations are enhanced. Meanwhile, covariance in the pairwise edge displacements, which appears as a linear trend in the histogram plots, directly corresponds to correlations of the associated PCC matrix. At all temperatures, the plots become less linear with increasing separation as edge displacements become decoupled. Generally, we observe that edge fluctuations increase with temperature and become less correlated with increasing domain separation.

Within the trenches, cylinder dynamics are locally coupled by BCP chain connectivity and compositional constraints. The transient structure reflects a balance between the enthalpic penalty of polymer mixing and the entropic freedom of the random coil.[41] Increasing temperature weakens domain segregation, resulting in enhanced composition fluctuations and interfacial broadening.[54] With increased thermal energy, the polymer chains also have greater configurational freedom, which is visible as increased interfacial roughness. The associated interfacial tension and bending strain from edge displacement are accommodated by neighboring

Figure 3.7
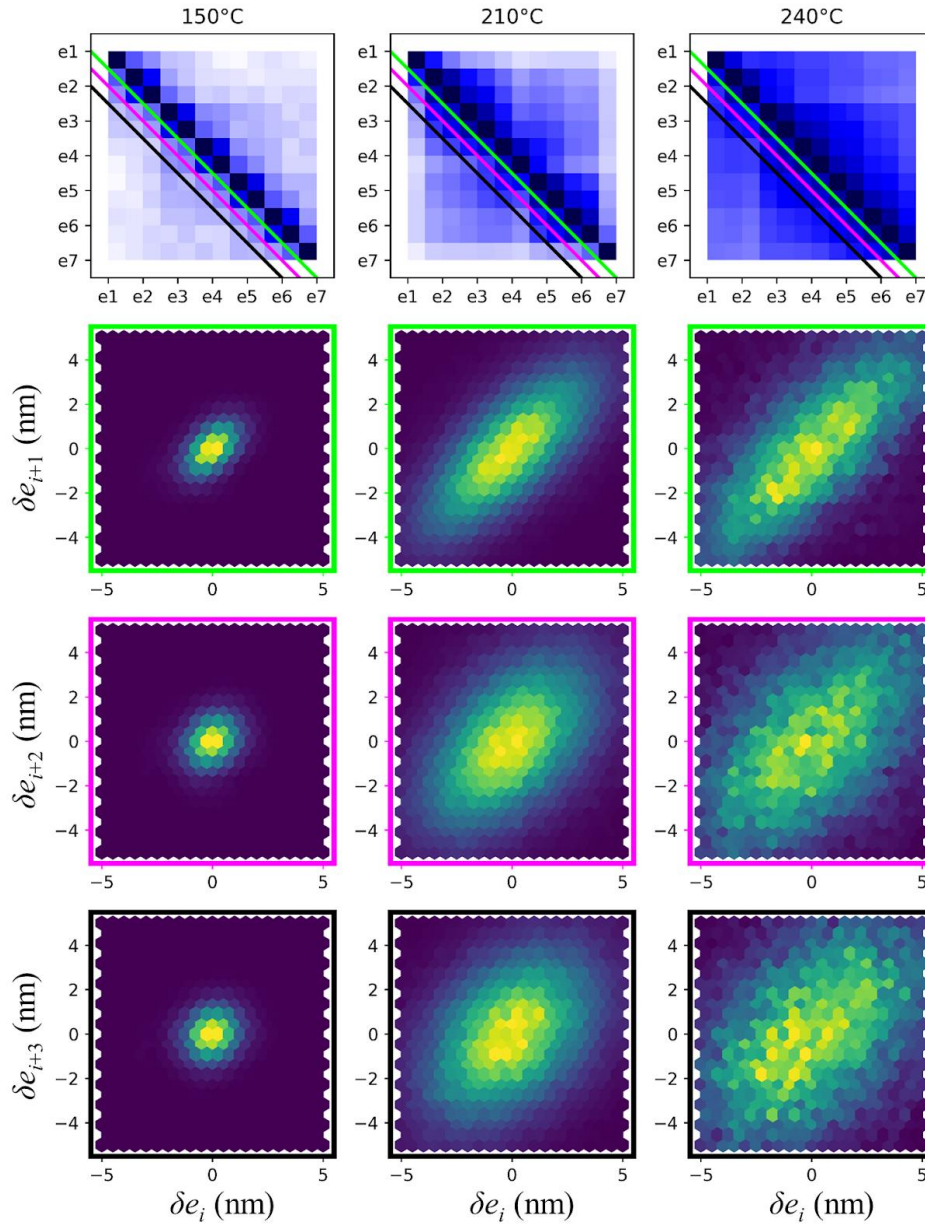
Edge fluctuation covariance. Two-dimensional histograms showing the pairwise distributions of edge displacements over a series of cylinder separations (1st, 2nd, and 3rd order) and temperatures (150, 210, and 240 °C). Each plot corresponds to a set of off-diagonal PCC matrix elements as indicated by the colored lines. The distribution widths show the magnitude of fluctuations, while the distribution shape indicates correlation between the edge displacements. The fluctuation magnitude increases with increasing temperature, and the covariance decreases with increasing separation.

domains, leading to correlated motion. At 150 °C, the observed edge perturbations are small, with a range of ~ 2 nm, and become sufficiently damped by one neighboring domain. Comparatively, at 240 °C, edge displacements have magnitudes of ~ 5 nm, roughly 20% of the cylinder width, resulting in large deviations from their equilibrium positions, and stabilization from correlated motion becomes significant. Our measured displacements correspond closely with interfacial widths of 4.9 ± 0.1 nm reported by Stein *et al.* in lamellar PS-*b*-PMMA after thermal annealing at 240 °C and quenching to room temperature; fluctuations during thermal annealing directly contribute to the final quenched roughness.[57]

Time Dependence

The *in situ* measurements made possible by high-speed AFM provide unique insight into the dynamics of interfacial fluctuations. Our imaging tracks the precise motion of cylinders over time, which could not previously be investigated due to the demanding imaging requirements — *i.e.* fast scan rates and high thermal stability — necessary for capturing these dynamics. Fluctuations are critical to the BCP assembly processes, as they lead to interfacial roughness and drive changes in connectivity for defect healing. By disabling the slow-scan axis, we increase the time resolution to match polymer diffusion time scales and, ultimately, to measure single-chain dynamics.

We analyze the time evolution of edge displacements by examining the discrete power spectral density (PSD) of cylinder trajectories in frequency space:

$$G_e(f) = \frac{2\Delta}{N_t{}^2} |E(f)|^2 \tag{3.8}$$

Here, N_t is the number of sampled points, Δ is the measurement time step, and $E(f)$ is the discrete Fourier coefficient of the edge position over a temporal frequency f. Similar definitions are used

for the placement and width in terms of the discrete Fourier coefficients $P(f)$ and $W(f)$, respectively:

$$G_w(f) = \frac{2\Delta}{N_t^2}|W(f)|^2; \qquad G_P(f) = \frac{2\Delta}{N_t^2}|P)|^2 \qquad (3.9)$$

PSD plots for LER, LWR, and LPR at 150, 210, and 240 °C are shown on log-log axes in **Figure 3.8**. The plots span a frequency range of 10^{-2} to 20 Hz, limited at low frequency by the survey time and at high frequency by the AFM scan rate. In previous reports, PSDs of spatial roughness have exhibited a natural length scale $r \sim L_0$, corresponding to a transition between single-chain dynamics and bulk behavior.[61,62] At high spatial frequencies, the roughness is limited by the range of motion of individual polymer chains, while at length scales greater than L_0 the combined contribution from multiple chains determines scaling of the bulk roughness. By analogy, we consider a characteristic diffusive time scale for the temporal roughness with:

$$\tau \sim L_0^2/2D \qquad (3.10)$$

where D is the BCP self-diffusion constant.[81] Interfacial chain fluctuations are dominated by the local Brownian motion of individual chains at short time scales and begin to couple with bulk modes on the diffusive time scale. Correspondingly, in the PSD spectra presented here, we find that roughness scales more rapidly at low frequencies, below a frequency threshold $f_t = 1/\tau$. In each frequency regime, the spectra follow power laws of the form $G(f) \propto f^k$ with different values for k, the frequency scaling factor.

Fit values of f_t and k are collected in **Table 3.3**. Over the temperature series, three general trends are observed: (1) the magnitude of roughness increases with temperature, (2) k decreases with temperature, and (3) f_t shifts to higher frequencies at higher temperatures. These trends all result from enhanced chain mobility and diffusion rates from the increased thermal energy of the

Figure 3.8
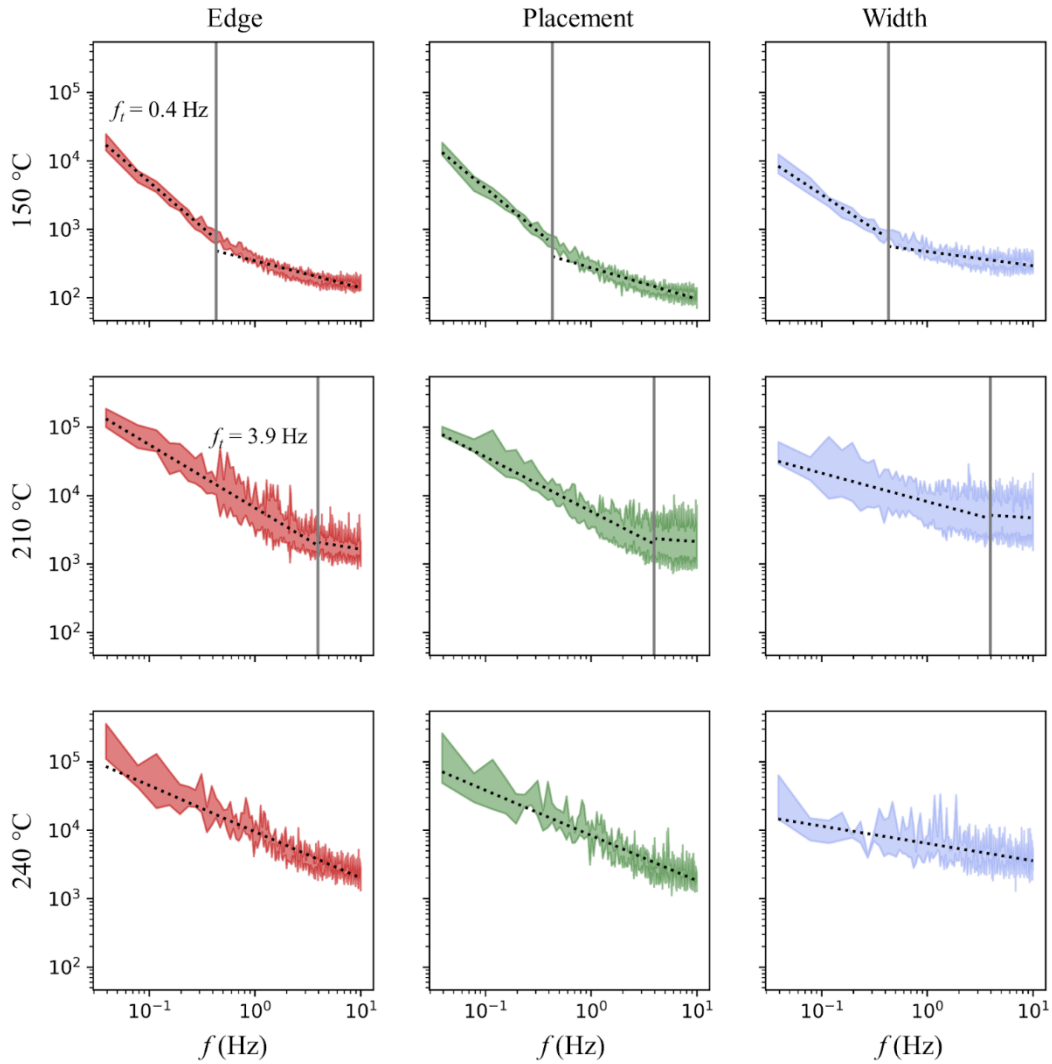
Time-dependent PSDs. Log-log plots of the temporal PSD for edge (red), placement (green), and width (blue) at 150, 210, and 240 °C. Colored bands correspond to the first standard deviation bounds of the discrete PSD. Dashed black lines correspond to power law fits. Gray vertical lines indicate the characteristic frequency which separates different dynamic regimes, with values of f_t (150 °C) = 0.4 Hz and f_t (210 °C) = 3.9 Hz.

system. At 150 and 210 °C, the PSD for each parameter is relatively flat at high frequencies, with k ~ -0.5, consistent with Brownian single-chain dynamics.[82] At frequencies below f_t, where bulk interactions contribute to roughness, we observe a stronger power law dependence. In this regime, the width roughness spectrum, G_w, is smaller in magnitude and shallower in slope than G_e and G_p, consistent with the weaker spatial coherence of width fluctuations. Comparing across temperatures, the frequency threshold increases by an order of magnitude from f_t (150 °C) = 0.4 Hz to f_t (210 °C) = 3.9 Hz. At 240 °C, the PSD for each parameter follows a single power law over the frequency range sampled, and a crossover to single-chain dynamics is not observed, indicating that chain fluctuations are too rapid to be captured by our AFM imaging. Although the roughness spectra appear to diverge at low frequencies, we expect that with longer measurement times the spectra would saturate. In the low-frequency limit, the range of edge and placement fluctuations are limited by the confining trench, while width fluctuations are limited by the polymer chain length.

From the measured frequency thresholds, we estimate diffusion coefficients as:

$$D \sim f_t L_0^2 / 2 \tag{3.11}$$

and find D(150 °C) ~ 4.1 × 10^{-12} cm^2/s and D(210 °C) ~ 4.0 × 10^{-11} cm^2/s. As a cut-off frequency is not observed at 240 °C, a value for D(240 °C) could not be determined. This calculation reflects the time scale for the onset of chain interactions along the polymer interface. More generally, chain diffusion of structured BCPs is anisotropic, and a complete description includes separate diffusion coefficients for diffusion along the interface D_{par} and across the interface D_{perp}.[83] Parallel diffusion is encumbered by chain entanglements, while perpendicular diffusion — which occurs more slowly — is hindered by chain hopping through incompatible domains.[84] Here, we examine fluctuations along the interface that do not require transport across

Table 3.3

Best-fit parameters of time-dependent PSDs. Best-fit parameters of the power-law dependence and characteristic frequency thresholds of roughness PSDs.

	Edge		Placement		Width		f_t (Hz)
	k (low f)	k (high f)	k (low f)	k (high f)	k (low f)	k (high f)	
150 °C	-1.3	-0.4	-1.3	-0.5	-1.0	-0.2	0.4
210 °C	-0.9	-0.3	-0.8	-0.1	-0.4	-0.1	3.9
240 °C	-0.7	-	-0.7	-	-0.3	-	-

polymer domains, and our estimate therefore provides a measure of D_{par}.

Our estimate compares well with previous measurements of cylinder-forming BCP mobility, which have identified D_{par} in the range 10^{-11} to 10^{-13} cm^2/s.[17,85-87] These experiments surveyed a wide variety of polymer species with different measurement techniques, resulting in a broad range of reported values. In particular, *in situ* AFM experiments by Tong and Sibener tracked the motion and annihilation of the defects in PS-*b*-PMMA cylinders with the same weight and composition as studied here and found $D_{par} = (2.6 \pm 0.5) \times 10^{-12}$ cm^2/s at 240 °C.[17]

This value reflects the self-diffusion constant in a defective system, in which interfacial connectivity is interrupted, hindering parallel transport.[86,88] Comparatively, our system considers the fluctuations of PS-*b*-PMMA cylinders in the absence of defects, and we attribute our faster kinetics to the well-ordered morphology.

CONCLUSION

Lithographic applications for BCP templates are currently limited by their native line roughness and, to be viable for microelectronic fabrication, significant advancements must be made to improve pattern regularity. While previous investigations have characterized interfacial roughness in quenched, room temperature systems, *in situ* high-speed SSD AFM imaging serves as a direct method for capturing the BCP dynamics above T_g. High-temperature imaging represents a significant step in understanding the intrinsic connections between the assembly of BCP patterns and dynamic fluctuations. Fluctuations should be understood not just as a barrier to device fabrication, but as a process fundamental to thermal annealing and defect healing of BCP thin films. Using SSD AFM imaging, we find that roughness scales with the annealing temperature and saturates above 220 °C, and, at high temperatures, fluctuations become broadly

coherent and extend spatially across confining trenches. This coherence reflects continuum

behavior in which cylinder oscillations may be described as a set of undulatory and peristaltic

modes. Analysis of the spectral dependence reveals a transition between this bulk behavior and

single-chain diffusion, demonstrating the use of AFM for capturing the dynamics of individual

polymer chains.

METHODS

Silicon wafer substrates (purchased from Virginia Semiconductor) were ultrasonically cleaned under toluene, acetone, and isopropanol and dried with N_2. Trench patterns were created by electron-beam lithography using an FEI NanoSEM 230 with PMMA as the electron-beam resist. After developing in methyl isobutyl ketone for 35 s, the patterned samples were rinsed with isopropanol and dried with N_2. Patterns were transferred to the silicon wafers with CF_4 and O_2 plasma dry etching, using a South Bay Technologies, Inc. RIE-2000. The resulting trenches were about 375 nm wide and 50 nm deep.

Cylinder-forming PS-*b*-PMMA (55k-22k, PDI 1.09) with $L_0 = 45$ nm was purchased from Polymer Source. A 0.9 wt% polymer solution was prepared in toluene and spin coated at 3000 rpm for 50 s onto the patterned substrates to produce a monolayer within the trench patterns. Film thicknesses, were measured with a Gaertner Waferskan ellipsometer, and found to be roughly 20 nm.

After pre-annealing in a tube furnace under argon at 250 °C for 8 h to produce aligned patterns, samples were imaged with an Asylum Cypher ES Environmental AFM. During imaging, samples were heated to *in situ* temperatures of 150-240 °C at ramp rates of 2 °C/s while under argon flow with cell pressures of 30-40 mbarg. The samples equilibrated for at least 5 min before imaging to ensure thermal stability of the instrument. High-speed, tapping-mode imaging was performed using gold-coated Arrow UHF cantilevers with resonant frequency of 1-1.5 MHz, achieving a scanning rate of 20 Hz and 5.9 nm pixel resolution. Images were collected with a 500 mV set point and in repulsive mode, while being careful to avoid tip-induced sample damage.

To accurately and reproducibly track and analyze domains, a custom image analysis software written in Python based on the SciPy framework was used.[89] At each temperature, the approximate location of the first PMMA domain in each trench was manually located on the time-averaged phase trace; the six successive PMMA domains were then located by finding the next six local minima. Each phase trace was then processed in parallel in order to find the true position of each domain at a given time. For each PMMA domain, the approximate cylinder placement was updated to the nearest local minimum. The neighboring left and right maxima then defined a local window that encompassed the interfaces between a given PMMA domain and its two adjacent PS domains. For each interface, the first derivative of the phase signal, smoothed with a three-point moving average, was fit with a model Gaussian to precisely locate the extrema positions, corresponding to the steepest slope of the phase and, thus, the PS/PMMA domain edges. An example of this procedure is illustrated in **Figure 3.3**. The phase signal was not well defined at the boundary of the trenches due to changing sample topography, and, therefore, the leftmost and rightmost edges were determined by doubling the distance between the first-derivative maximum and half-maxima.

Time correlations were extracted through estimation of the power spectral density (PSD) of the fluctuations of the three residuals associated with LER, LPR, and LWR. While analogous to previous work examining the PSD in real space, we directly measured the fluctuations in time resulting in a temporal PSD as a function of frequency, as opposed to a spatial PSD as a function of wavenumber.[29] We estimated the PSD as equal to the square of the absolute value of the discrete Fourier transform of the residuals. To properly estimate the PSD, while minimizing variance, we averaged multiple PSDs from each experiment measured across sample space.[90] Due to the large amount of data captured during real-time AFM measurement, the PSD was first

calculated for each individual domain, *i.e.* two edges and each domain's width and placement. These individual PSDs were averaged over a given image to create a per image PSD, and then were further averaged across images taken at a given temperature to create the final PSD for each temperature-residual pair, as shown in **Figure 3.8**. The colored bands represent the average PSD, plus or minus one standard deviation, as a quantification of the remaining spectral noise. At 150 and 210 °C, the spectra exhibited two dynamic regimes, which followed different power laws. These regimes were separated by a characteristic frequency that was found by iterating over the spectrum to determine the frequency that maximized the change of slope between the two regions.

Chapter 4.

Gold Nanorod Alignment on Block Copolymer Templates

We present an efficacious method for the end-to-end assembly of gold nanorods of various aspect ratios on corrugated, cylinder-forming diblock copolymer templates. The nanorods exhibit excellent selectivity for (>98%) and alignment with the polymer grooves due to capillary forces and the substrate's topography, even cases where the depth of corrugation is significantly smaller than the diameter of the nanorods. Preliminary polymer alignment *via* graphoepitaxy is employed to achieve long-range, linearly aligned gold nanorod arrays, with applications as surface-enhanced Raman scattering (SERS) sensors. Within these arrays, nanorods assemble with end-to-end alignment, maximizing the electric field enhancement of the nanorod junctions and optimizing the SERS enhancement. Furthermore, because the gold nanorods preferentially deposit inside of the polymer coated trenches, these substrates exhibit in-trench and out-of-trench signal contrast, as well as polarization dependent spectra with a 24-fold enhancement in signal intensity for trenches aligned parallel, versus perpendicular, to the incident laser. The simple construction of these systems and their unique SERS properties provide a new and interesting avenue for device fabrication.

INTRODUCTION

Thin films of nanoparticles have attracted considerable attention due to their possible applications to electronic devices,[91,92] magnetic storage,[93] and sensors.[94,95] Investigations have focused on noble metal nanoparticles, due to their well-documented surface-enhanced Raman spectroscopy (SERS) properties.[95-97] Gold nanoparticle (AuNP) SERS systems are produced using either top-down or bottom-up techniques, where the regions of electric field enhancement, known as hot spots, are fabricated by electron-beam lithography,[98,99] with ion-beam sputtering,[100] or through the deposition of colloidally synthesized AuNPs. Controlling the deposition of colloidal AuNPs is attractive because the locations of the hot spots are determined by the order and alignment of the AuNPs on the substrate. Successful deposition has been achieved by chemically functionalizing[101-103] or patterning[103-109] the substrates or through modification of the AuNP colloid.[110-112]

This chapter presents a straightforward, bottom-up technique for producing ordered end-to-end arrays of colloidal gold nanorods (AuNRs) with favorable SERS properties. Anisotropic AuNRs have garnered particular attention for SERS applications due to their favorable material features, including controllable synthetic procedures, tunable plasmon resonances, and strong electromagnetic field enhancements.[96-97,109,112-114] Coupling between plasmonic nanoparticles further strengthens the electric field hot spots of AuNR assemblies with respect to individual structures, increasing the SERS response, as documented for AuNR chains and for various large-scale, two- and three-dimensional AuNR aggregates.[109,110,115-2117]

The AuNR arrays presented in this chapter are produced by depositing colloidal AuNR onto silicon nitride substrates patterned with cylinder-forming poly(styrene-*block*-methyl methacrylate) (PS-*b*-PMMA) block copolymer (BCP) templates. BCP templates are attractive

platforms because they readily self-assemble into well-ordered microdomains of spheres, lamellae, or cylinders, and, through directed self-assembly (DSA), they can achieve long-range, defect-free structures.[12,27] BCP microdomains are also comparable in size to colloidally synthesized nanoparticles (5-50 nm), and therefore may be used to control nanoparticle deposition.[118] Nanoparticles preferentially localize on the BCP template due to chemical or topographic contrast between the blocks.[105,119-121] To improve topographic contrast, the relatively small native corrugation of BCP patterns may be enhanced through the selective removal of one polymer domain; for example, in PS-*b*-PMMA, UV-light exposure selectively degrades the PMMA block. In this chapter, we investigate the use of acetic acid vapor annealing as a convenient method for enhancing the corrugation of cylinder-forming PS-*b*-PMMA films without the need for substrate preprocessing.[121] Acetic acid vapor directly induces a topographically-enhanced surface reconstruction through selective swelling of the PMMA cylinders. Although the resulting BCP corrugation is significantly smaller than the particle diameter, excellent alignment is readily achieved for single and individual chains of end-to-end aligned AuNRs.

RESULTS AND DISCUSSION

Topographically-enhanced, cylinder-forming PS-*b*-PMMA BCP templates were fabricated by the selective swelling of PMMA domains in a saturated vapor of acetic acid.[121] Because the vapor-swollen PMMA blocks are covalently bound to the unswollen PS blocks, the microdomains cannot expand laterally, and instead, the PMMA chains swell and overflow onto the film surface, as shown in **Figure 4.1.A**. When the substrates are removed from the solvent chamber, the acetic acid quickly evaporates, causing the PMMA chains to collapse and leaving

Figure 4.1
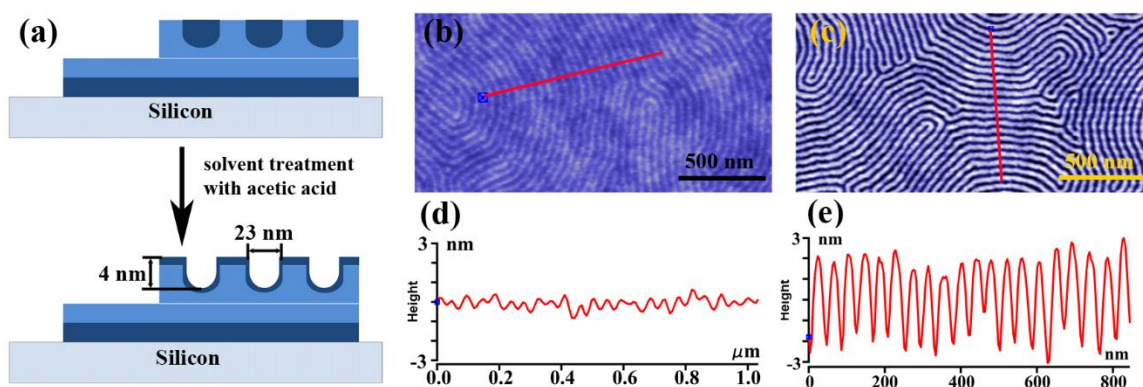
Corrugation enhancement from acetic acid vapor annealing. (A) Schematic representation of the corrugated cylinder-forming PS-*b*-PMMA BCP template fabrication (Key: *Grey* = silicon substrate, *Dark blue* = PMMA, *Light blue* = PS). AFM height images of the PS-*b*-PMMA fingerprint patterns (B) before and (C) after acetic acid vapor treatment. From the AFM height profiles, the film's corrugation increases from (D) ~1 nm before vapor exposure to (E) ~4 nm after the acetic acid treatment. The height profiles are taken along the arrows in (B) and (C).

behind a corrugated surface. A comparison of atomic force microscopy (AFM) images of the polymer surface before and after acetic acid exposure, shown in **Figures 4.1.B** and **C**, reveal a large enhancement of the film's surface contrast. As seen by directly comparing the AFM height profiles **Figures 4.1.D** and **E**, the film's height variation increases from roughly 1 to 4 nm following the acetic acid treatment.

To investigate the alignment of AuNRs on the BCP films, a series of nanorods with aspect ratios of 3.05, 3.20, 4.02, and 6.33 were synthetically prepared, and the properties of these samples are documented in **Table 4.1**. Throughout the chapter, we refer to these samples as $NR_{3.05}$, $NR_{3.20}$, $NR_{4.02}$, and $NR_{6.33}$, respectively. Ensemble UV/vis spectra of each of the AuNR solutions are shown in **Figure 4.2**, alongside transmission electron microscopy (TEM) images of the corresponding samples. The UV/vis spectra show a characteristic two-peak structure resulting from excitations of the surface plasmon resonances of the anisotropic nanorods; the principle peak corresponds with the longitudinal resonance, and the secondary peak with the transverse resonance. The longitudinal resonance is red-shifted with increasing nanorod aspect ratio over the AuNR series due an increase in the plasmon confinement length.

The $NR_{3.05}$ solution was then spin coated onto the BCP pattern surfaces to assess their feasibility as nanorod scaffolds. AFM imaging, shown in **Figure 4.3**, reveals robust alignment of nanorods with the underlying template surface over a range of surface coverages. Low surface density AuNR arrays, as shown in **Figure 4.3.A** were made by spin coating the stock colloid twice. The AuNRs were sparsely dispersed over the entire substrate, predominantly existing as isolated particles, with only 45 AuNRs/μm^2. They exhibited a nearly exclusive tendency to rest within the fingerprint grooves — greater than 98%, as determined by counting over 800 AuNRs

Table 4.1

Dimensions of synthesized AuNRs. Physical dimensions of the AuNR samples synthesized and examined in this chapter.

	Length (nm)	Diameter (nm)	Aspect Ratio
$AR_{3.05}$	61 ± 1	20 ± 1	3.05
$AR_{3.20}$	58.95 ± 3.63	18.41 ± 1.95	3.20
$AR_{4.02}$	59.76 ± 7.26	14.87 ± 2.00	4.02
$AR_{6.33}$	70.50 ± 7.59	11.14 ± 1.62	6.33

Figure 4.2
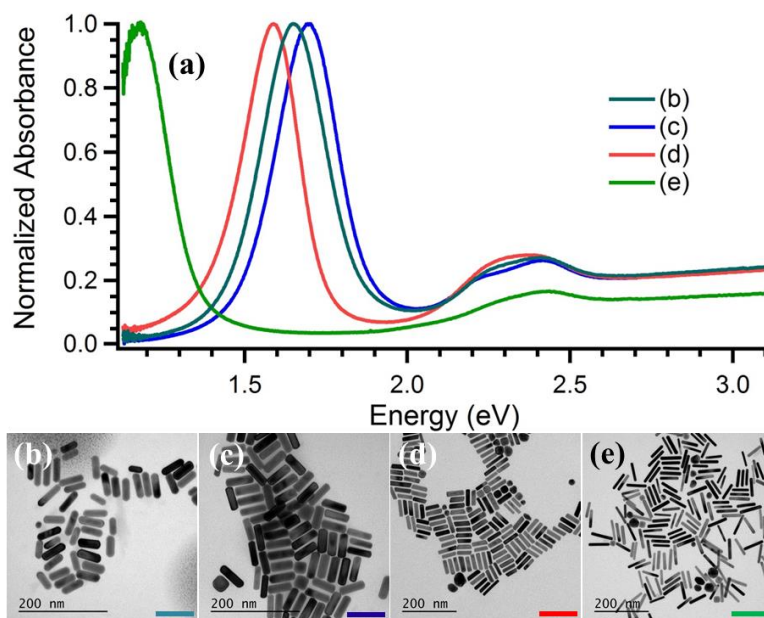
AuNR spectroscopy and imaging. (A) UV/vis spectra of the AuNRs used in the chapter. Absorbances are normalized to the peak maximum. TEM images of (B) $NR_{3.05}$, (C) $NR_{3.20}$, (D) $NR_{4.02}$, and (E) $NR_{6.33}$ as described in **Table 4.1**.

Figure 4.3
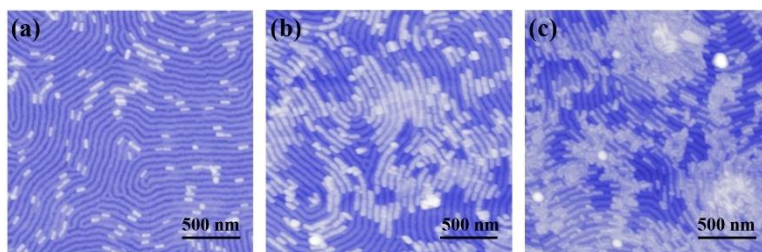
AuNR templating with varying surface coverage. AFM images of $NR_{3.05}$ deposited on the topographically-enhanced, cylinder-forming PS-*b*-PMMA BCP thin films after solvent treatment with acetic acid. The AuNR densities are (A) 45 AuNRs/μm^2, (B) 160 AuNRs/μm^2, and (C) >300 AuNRs/μm^2. The AuNRs in (B) appear larger because an AFM tip with a larger radius was used to record the image.

— where they were aligned along the contours. When the colloid was spin coated six times onto the films, the surface density increased to 160 AuNRs/μm^2, shown in **Figure 4.3.B**, and the AuNRs nearly covered the substrate as a monolayer. The AuNRs were still aligned end-to-end along the contours of the fingerprints, resting within the grooves with over 97% selectivity. After spin coating ten times, the AuNRs formed three-dimensional clusters with greater than 300 AuNRs/μm^2, as shown in **Figure 4.3.C**, and lost the structure of the underlying substrate.

Next, to assess the effect of changing the AuNR aspect ratio, $NR_{3.20}$, $NR_{4.02}$, and $NR_{6.33}$ were spin coated onto the BCP fingerprint templates. In all cases, the AuNRs deposited end-to-end in the fingerprint grooves with over 97% selectivity, as shown in **Figure 4.4**. Remarkably, $NR_{6.33}$ did not exhibit any side-to-side packing, even though the rod diameter (11 nm) was less than half of the width of the grooves (23 nm). Furthermore, none of the AuNR samples exhibited obvious tilting within the polymer grooves, and all were aligned with the pattern's contours.

These AuNR deposition results exhibit stark contrast from previous reports.[12,15,16,33] First, the AuNRs only assemble end-to-end within the template grooves. Second, the AuNRs did not deviate from the contours of the grooves. Third, the AuNRs successfully assembled despite the fact that the BCP template height profiles were much smaller than the deposited AuNR diameters — as low as 20% of the AuNR diameter.

These observations are consistent with a simple model involving the capillary forces exerted on partially immersed colloidal particles[122-125] and the topography of the BCP template[126] (**Figure 4.5**). Because of the large aspect ratio of the AuNRs, only the capillary force arising from the contact line along their length is considered.[38] The resulting force, $F = \gamma^2 L \cos(\alpha)$, is maximized when the particles are half-immersed, where $\gamma = 72.8$ dyne/cm is the surface tension of water, L is the length of the rod, and α is the contact angle of the water at the AuNR's surface.

Figure 4.4
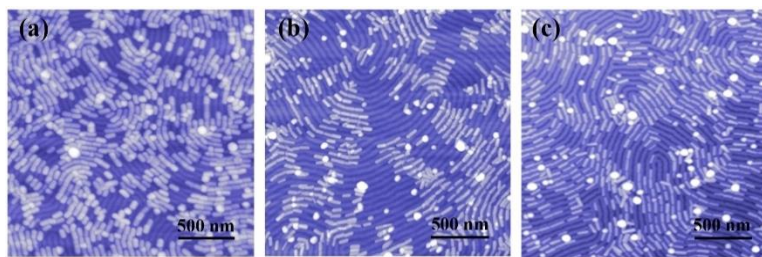
AuNR templating over a series of aspect ratios. AFM images of AuNRs with different ARs on the topographically-enhanced, horizontal cylinder-forming PS-*b*-PMMA BCP thin films. (A) $NR_{3.20}$, (B) $NR_{4.02}$, (C) $NR_{6.33}$. For each sample, the AuNRs align in grooves with over 97% selectivity. The images are 2 μm × 2 μm.

The energy that each AuNR gains by moving from a crest to a trough is calculated by integrating over the substrate's corrugation h, yielding a change in energy:

$$\Delta E = \gamma^2 L\, h \cos(\alpha) \tag{4.1}$$

Calculating for AuNRs with 61 nm length and $\alpha = 30°$, the crest to trough energy difference $\Delta E = 3.08$ x 10^{-17} J, four orders of magnitude greater than their room temperature thermal energy of 4.11 x 10^{-21} J. [127] The strength of the capillary force explains both the AuNRs' extreme preference for and alignment in the grooves. Because the fingerprint patterns are generated from cylindrical PMMA domains, their surface is curved, as shown schematically in **Figure 4.1.A**. Therefore, any misalignment in the grooves would result in a vertical displacement. From the equation of the tangent circle describing the curvature of grooves with radius ~ 20 nm, thermal energy could only induce a misalignment of roughly 0.5°.

Thus, the capillary force explains AuNR ordering, but it is not sufficient to explain the lack of lateral packing. For the $NR_{3.05}$, $NR_{3.20}$, and $NR_{4.02}$ samples with larger diameters nearly as large as the groove width of 23 nm, the absence of side-to-side packing can be easily attributed to geometric confinement. However, the $NR_{6.33}$ have a diameter smaller than half of the channel width, and previous reports of nanorod deposition on BCP films have observed lateral NR packing under these conditions.[105,120] In this case, we attribute the lack of side-to-side packing to electrostatic repulsion between the AuNRs. The colloidally synthesized AuNRs are coated in a hexadecyltrimethylammonium bromide (CTAB) and 5-bromosalicylic acid (5-BSA) bilayer, and each rod may be approximated as having a positive charge q, roughly equal to the number of CTA^+ molecules in the outer layer, as determined by calculating the AuNR surface area and assuming an optimal CTA^+ packing density of 2.44 CTA^+/nm^2. [128,129] The Debye length of the

Figure 4.5

(a)

$\vec{F}$

$\otimes$ L

α

h

(b)
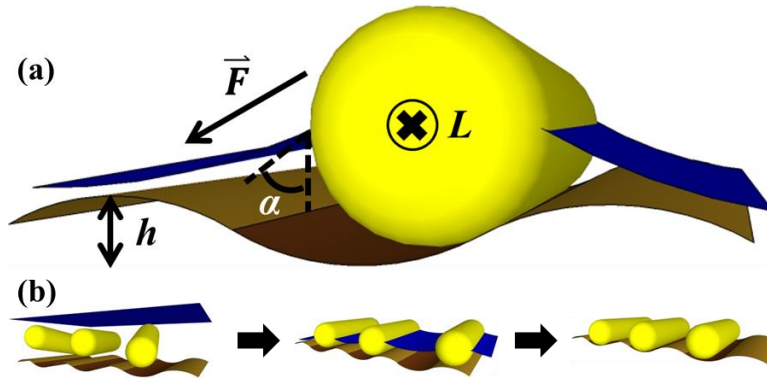
Capillary forces during deposition and drying. Schematic representation of the AuNRs drying on the substrates. (A) Partially immersed AuNR being drawn into a polymer trench. The $\vec{F}$ indicates the direction of the capillary force. All variables are the same as defined in the text. (B) Schematic representation of the AuNR deposition process, from the fully immersed AuNRs, to the partially immersed particles, to the aligned product.

colloid is given by:

$$\kappa^{-1} = \sqrt{\frac{\varepsilon_r \varepsilon_0 k_B T}{2 N_A e^2 I}} \qquad (4.2)$$

where ε_r is the relative permittivity of water at room temperature, ε_o is the permittivity of vacuum, k_B is the Boltzmann constant, T is the absolute temperature, N_A is Avogadro's number, e is the fundamental unit of charge, and I is the colloid's ionic strength in mol/m^3. With a CTAB concentration of 1 mM and using a value of $\varepsilon_r = 78.54$, the Debye length is calculated as $\kappa^{-1} = 9.62$ nm. The electrostatic repulsion for two $NR_{6.33}$ separated by their Debye length is:

$$F_R = \frac{1}{4\pi\varepsilon_0 \varepsilon_r} \frac{|q|^2}{(\kappa^{-1})^2} \qquad (4.3)$$

which yields a very large repulsive force of 1.36 x 10^{-6} N, consistent with the long-term stability of the colloidal suspension. Moreover, as long as the particles are fully submerged in solution, they will be separated by a distance of at least their Debye length, irrespective of the substrate geometry. As the solvent evaporates, the AuNRs will remain fully immersed, with their interparticle interactions governed by electrostatics. This effect will keep them well spaced as they approach the substrate surface. When enough of the solvent has evaporated such that AuNRs are partially immersed, capillary forces are strong enough to induce the final assembly on the substrate (**Figure 4.5.B**). End-to-end assembly is favored because of that orientation reduces the electrostatic repulsion, as compared to lateral assembly. If the deposition is formed at a higher concentration of the AuNRs, side-to-side and random aggregates appear because the ionic strength increases as water evaporates, drastically shrinking the Debye length.

SERS measurements were performed on the samples shown in **Figure 4.3** to characterize the Raman enhancement properties of the AuNR films. Benzenethiol (BT) diluted in ethanol was drop cast onto the substrates and dried in air, and the Raman spectra were recorded using the 785

Figure 4.6
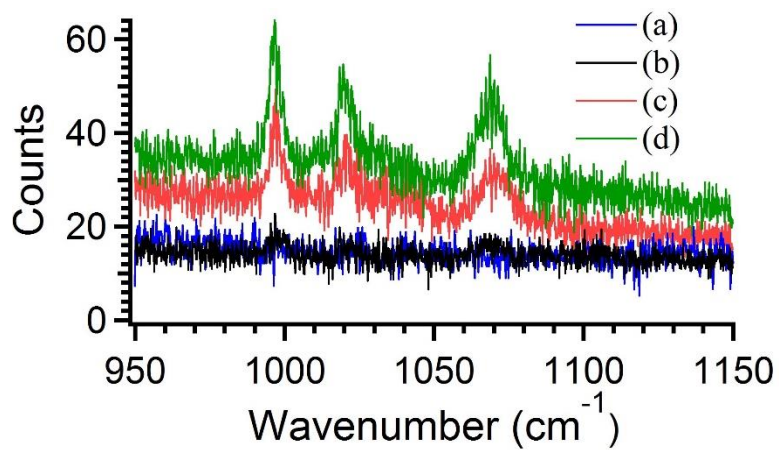
SERS of benzenethiol. Raman spectra of (A) BCP fingerprint substrate without AuNRs, (B) 45 AuNRs/μm^2 substrate, (C) 160 AuNRs/μm^2 substrate, (D) >300 AuNRs/μm^2 substrate. The peaks at 998, 1022, and 1072 cm^{-1} are the characteristic BT peaks in this region.

nm laser of a Horiba LabRam Evolution confocal Raman microscope. Spectra recorded from BCP thin films without AuNRs showed no signal, while spectra with intensities that increased with AuNR surface density were recorded from those substrates (**Figure 4.6**). The selective and reproducible AuNR deposition directed by the BCP microdomains indicated that linear, end-to-end AuNR arrays of micron dimensions with unique SERS properties could be achieved if the microdomains' alignments could be controlled, *e.g.* with graphoepitaxy.[12] Thus, substrates were patterned with sets of 500 nm wide and 50 nm deep trenches before the BCP thin film was deposited and treated. Because the aligned PS-*b*-PMMA cylinder domains are confined to the trenches, the AuNR colloids could be drop cast onto the substrates so that the drying contact line would draw the NPs into the predefined trenches.[106,108,130]

After the droplet recedes, a thin layer of solvent still covers each trench, because they are deeper than the AuNRs' diameters. This result is analogous to the situation depicted in the middle panel of **Figure 4.5.B**, meaning that as the solvent evaporates, the previously described capillary forces and the BCP microdomains will direct the AuNR assembly. The AuNRs shown in **Figure 4.2.B** were found in the trenches with over 97% selectivity, with surface densities dictated by the number of depositions repeated. For trenches with surface densities of 40 AuNRs/μm^2 (**Figure 4.7.A**) and 160 AuNRs/μm^2 (**Figure 4.7.B**), the AuNRs aligned along the straight BCP contours, while trenches with over 250 AuNRs/μm^2 (**Figure 4.7.C**) exhibited large, three-dimensional clusters that lost the structure of the underlying film, similar to those seen in **Figure 4.3.C**. The nearly monolayer coverage of linearly aligned AuNRs in the trenches of **Figure 4.7.B** present a combination of surface density and alignment that should have the most interesting and useful SERS properties. Explicitly, we wished to investigate how the AuNR

Figure 4.7
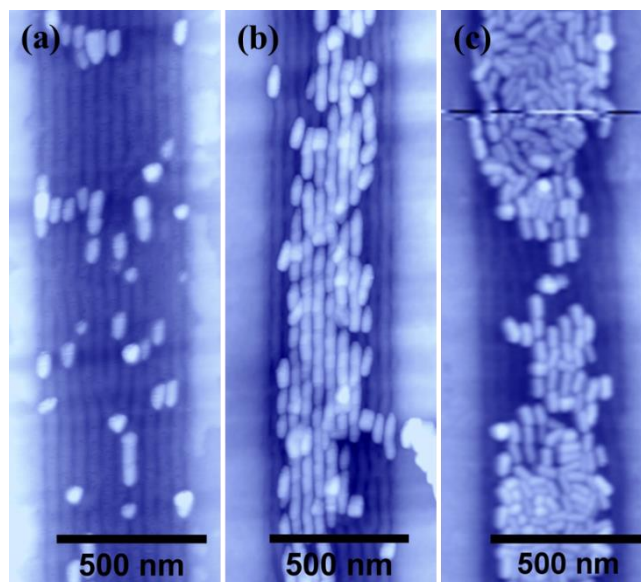
Hierarchically-aligned AuNRs. AFM images of different AuNR colloid concentrations drop cast onto laterally ordered thin films of horizontal, cylinder forming PS-*b*-PMMA BCP made using graphoepitaxy. The AuNR densities are (A) 40 AuNRs/μm^2, (B) 160 AuNR/μm^2, and (C) >250 AuNRs/μm^2. The AuNRs are 20 nm by 61 nm, and the images are 0.75 μm × 1.5 μm.

localization affected the Raman signal across the substrate and whether the nanowire AuNR arrays exhibited polarization dependent SERS.[131]

Because the graphoepitaxy trenches are optically identifiable, local regions on the substrates can be closely matched with corresponding AFM images (**Figures 4.8** and **4.9**). Thus, samples were functionalized with a monolayer of BT, mounted on a rotation stage, and the signal intensities of the characteristic BT peaks at 998, 1022, 1072, and 1572 cm^{-1} were tracked by scanning the laser over specific trenches oriented parallel (**Figures 4.8.A** and **4.9.A**) and perpendicular (**Figures 4.8.C** and **4.9.B**) to the incident laser polarization in 200 nm steps.[132] When the trenches were aligned parallel to the laser polarization, the BT peak intensities modulated with the periodicity of the trenches, showing a 3.5-fold signal enhancement when the laser scanned inside, as opposed to outside, the trench. For this sample, the spacing is 1200 nm, since the trenches were 500 nm wide and were separated by 700 nm crests.

This periodicity and signal localization are especially impressive since the theoretical minimum of the laser spot diameter was roughly 1064 nm, 50% larger than the spacing between the trenches. When the trench was aligned perpendicular to the laser polarization, the Raman signal intensities were severely reduced and showed no correlation with the substrate's surface. The in-trench signal intensities of the parallel orientation exhibited a 24-fold enhancement over the same regions in the perpendicular orientation, demonstrating that these large, ordered, macroscopic arrays of anisotropic NPs maintain the polarization dependence of single structures (**Figure 4.9**). These SERS results show that macroscopic systems of closely spaced, colloidally synthesized NPs will still have strong, directionally dependent electromagnetic enhancement properties when their alignment is carefully controlled.

Figure 4.8
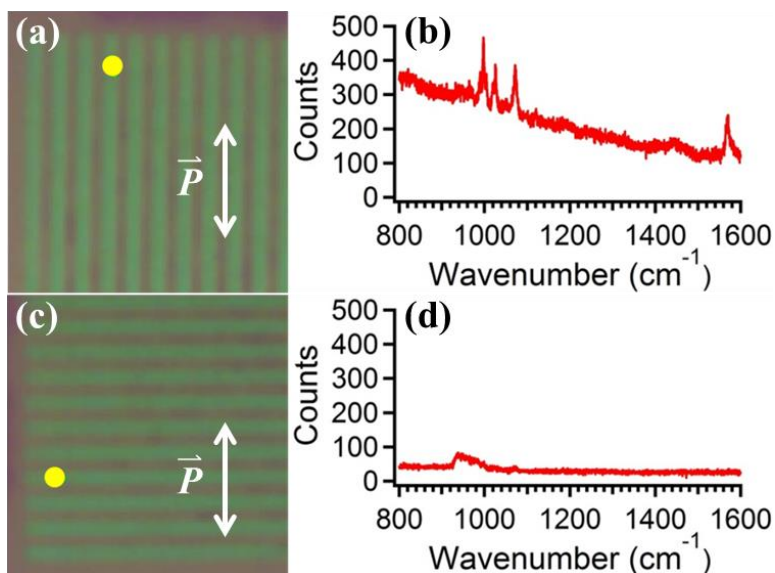
Polarization dependent SERS response. (A, C) Optical images of graphoepitaxy trenches oriented parallel (a) and perpendicular (C) to the incident laser. The yellow dot indicates the region of the trench that was scanned over. (B, D) Raw Raman spectra recorded from the middle of each trench oriented parallel (B) and perpendicular (D) to the laser. The spectral features in (B) correspond to the characteristic BT peaks in this region, while the spectral feature at 950 cm^{-1} in (D) corresponds to the silicon feature in this region. These spectra correspond to the respective 600 nm step positions in Figures 4.9.A and B. The arrows and $\vec{P}$ indicate the laser orientation relative to the substrate.

Figure 4.9
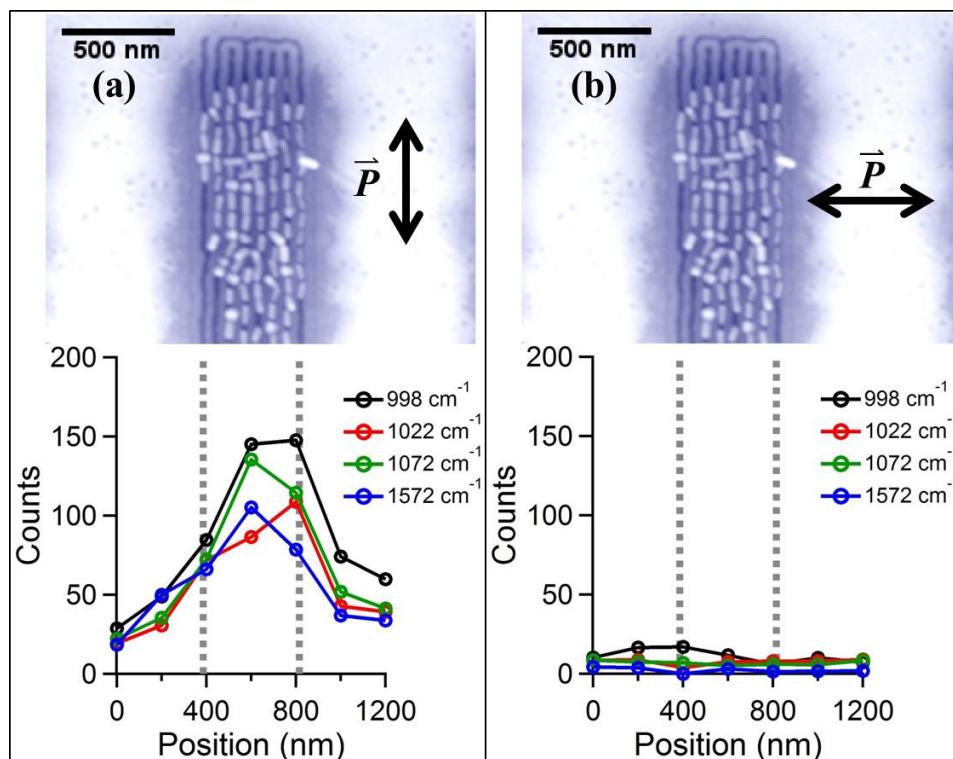
Spatial mapping of the SERS signal. (A) Results of the Raman spectral mapping over the graphoepitaxy trench aligned parallel to the laser (Figure 4.8.A). Top: AFM image of the trench region. Bottom: Plot of the signal intensities of the four characteristic BT peaks, which are maximized within the trench and minimized in regions outside the trench. (B) Results of the Raman spectral mapping over the graphoepitaxy trench aligned perpendicular to the laser (Figure 4.8.B). Top: AFM image of the trench region. Bottom: Plot of the signal intensities of the four characteristic BT peaks, which are severely reduced and featureless. The arrows and $\vec{P}$ indicate the laser orientation relative to the substrate, and the gray lines indicate the width of the trench.

CONCLUSION

In summary, we investigated the alignment of AuNRs on topographically-enhanced, horizontal cylinder-forming PS-*b*-PMMA BCP templates, whose corrugation was much smaller than the widths of the AuNRs. We demonstrated precise control over the ordering and orientation of AuNRs of multiple aspect ratios for surface densities at and below 160 AuNR/μm^2 and presented a simple model that demonstrated that the topography of the substrate, while shallow, drives the AuNR alignment. Graphoepitaxy was then employed to align the BCP microdomains, allowing long-range, linear arrays of AuNRs to form. We characterized the SERS properties of these structures and found that they exhibit extreme signal localization and polarization dependent spectra, with a maximum 24-fold signal enhancement. This effective, topography driven AuNR assembly and alignment that shows strong, directional electromagnetic enhancements offers great potential for the fabrication of reproducible, macroscopic, colloidal AuNR based plasmonic waveguides, optoelectronics, and sensing chips.

METHODS

Hexadecyltrimethylammonium bromide (CTAB, ≥99%), gold (III) chloride trihydrate (HAuCl$_4$, ≥99.9% metals basis), and 5-bromosalicylic acid (5-BSA, ≥98.0%) were purchased from TCI Chemicals and used without further purification. Silver nitrate (AgNO$_3$, 99.9999%), L-ascorbic acid (Vitamin C, ≥99.0%), sodium borohydride (NaBH$_4$, ≥98.5%), and benzenethiol (BT, ≥98%) were purchased from Sigma-Aldrich and used without further purification. Hydrochloric acid (HCl, 1 N) was purchased from Fisher Scientific and used without further purification. Silicon nitride (Si$_3$N$_4$) substrates were purchased from Virginia Semiconductor, Inc., cut to 1 cm^2, and cleaned with toluene, acetone, and methanol using an ultrasonic cleaner, and finally dried with nitrogen. The PS-b-PMMA (55k-22k, PDI = 1.09) was purchased from Polymer Source, Inc. and used without further purification.

UV/vis spectra were recorded using an Agilent HP 8453. TEM images were taken using a FEI Spirit operating at 120 kV. AFM images were taken using an Asylum Research's MFP-3D AFM performed in AC (tapping) mode with Olympus AC240TS cantilevers with a spring constant of 2 N/m. Electron-beam lithography was performed using a Hitachi 2700 SEM at 300 μC/cm^2. SERS spectra were recorded using a Horiba LabRam Evolution confocal Raman microscope, a 785 nm diode laser, 100× objective with NA 0.90, 1200 gr/mm, and an Andor Synapse CCD detector.

The cleaned Si$_3$N$_4$ substrates were spin coated with PS-b-PMMA block copolymer in 0.9% toluene solution at 4000-5500 rpm for 60 s and then annealed at 523 K under an inert argon atmosphere for 1 h. The phase separated BCP thin films were then exposed to saturated acetic acid vapor for 15 min to induce the selective swelling of the PMMA cylinder domains. For the

substrates created by graphoepitaxy, 500 nm wide, 20 μm long, and 50 nm deep trenches were patterned into the substrate by electron-beam lithography before being coated with BCP.

The AuNRs used in this chapter were synthesized using a scaled down and slightly modified version of the protocol developed by Ye *et al.*[128] In all cases, the AuNR seeds were synthesized by dissolving 364 mg of CTAB in 10 mL of nanopore water at 30 °C and under vigorous stirring, then adding 250 μL of a 10 mM $HAuCl_4$ solution and 600 μL of a fresh, 10 mM $NaBH_4$ solution. The solution promptly turned yellow-brown and was vigorously stirred for two minutes before being set aside.

All AuNR colloids were made by dissolving 182 mg of CTAB and 21.9 mg of 5-BSA in 10 mL of nanopore water at 70 °C under vigorous stirring, and were then cooled to 30 °C. For the AuNRs of AR 3.05-3.20, 96 μL of a 10 mM $AgNO_3$ solution, 500 μL of a 10 mM $HAuCl_4$, 51.2 μL of a fresh, 100 mM ascorbic acid solution, and 16 μL of the AuNR seed solution were added to the solution. For the AuNRs of AR 4.02, 384 μL of a 10 mM $AgNO_3$ solution, 500 μL of a 10 mM $HAuCl_4$, 500 μL of 1M HCl, 51.2 μL of a fresh, 100 mM ascorbic acid solution, and 16 μL of the AuNR seed solution were added to the solution. For the AuNRs of AR 6.33, 384 μL of a 10 mM $AgNO_3$ solution, 500 μL of a 10 mM $HAuCl_4$, 500 μL of 1M HCl, 25.6 μL of a fresh, 100 mM ascorbic acid solution, and 16 μL of the AuNR seed solution were added to the solution. The colloids were vigorously stirred for 30 s, then left to age overnight (15-18 h). All solutions were then hard centrifuged at 8500 *g* and 30 °C for 15 minutes, and had their supernatants decanted and pellets resuspended in 10 mL of nanopore water before being centrifuged again under the same conditions. After the second centrifugation, the supernatant was decanted, and the pellet resuspended with 250 μL of nanopore water. Aliquots of these mixtures were removed for UV/vis and TEM analysis (**Figure 4.2**).

The AuNR colloid was deposited on the BCP fingerprint films by spin coating at 3000

rpm for 60 s multiple times to achieve the surface densities described in **Figure 4.3**, dried in air,

then imaged by AFM. For the AuNRs of different AR, described in **Figure 4.4**, each colloid was

spin coated six times at 3000 rpm for 60 s, dried in air, then imaged by AFM. For the substrates

created by graphoepitaxy, the AuNR colloid was drop cast onto the surface, the excess liquid

wicked away, and the substrates dried in air before AFM imaging. This process was repeated

several times to achieve the desired particle densities. Regions on interest for Raman

spectroscopy were identified at this point.

For the SERS characterization of the BCP fingerprint film without AuNRs, 20 µL of a 2

$\times 10^{-4}$ M BT solution in ethanol were drop cast onto the substrates, dried, and the Raman spectra

recorded with laser power of 14.1 µW for 30 s. The SERS characterization of the

lithographically-patterned substrate of **Figures 4.8** and **4.9** was performed by drop casting 21 µL

of a 2 x 10^{-5} M BT solution in ethanol onto the 0.81 µm^2 substrates, to ensure the BT monolayer

packing of 0.544 nmol/cm^2.[132] The samples were mounted on a rotation stage and manually

oriented parallel (0°) or perpendicular (90°) to the laser's polarization, as determined by using

the reflected microscopy optics of the Horiba LabRam Evolution (**Figures 4.8.A** and **C**), and the

Raman spectra were recorded with a laser power of 75.5 µW for 20 s. The laser was scanned

over the sample's surface using the Duoscan capability of the microscope, meaning the beam

was moved with mirrors, instead of the sample being moved by the mechanical stage. This

procedure helped limit possible issues involving backlash and drift that could have been

exacerbated through the use of an after-market rotation stage. All SERS data were recorded

using the Horiba LabSpec 6 software, and the peak fits were performed in Igor Pro with

background corrected Voigt functions. The 785 nm laser was used for all experiments because

the 633 nm laser yielded too high of a fluorescent background, caused by the AuNRs.

Chapter 5.

Solvent Swelling of Block Copolymer Nanoislands

Atomic force microscopy (AFM) imaging was used to study the *in situ* swelling of poly(styrene-*block*-methyl methacrylate) (PS-*b*-PMMA) terraces under cyclohexane, a selective solvent for PS. These diblock copolymer terraces form insulated, single-layer PS domains, which confine the solvent swelling to two dimensions. The observed swelling is highly anisotropic with expansion occurring normal to the surface plane. Swollen terraces become softer and are sensitive to interaction with the AFM scanning probe. In this system, solvent swelling was observed to propagate *via* a sharp solvent front from terrace edges, separating swollen and unswollen polymer regions, indicative that dynamics are mediated by the chain relaxation rate, *i.e*. a Case II diffusion mechanism. Based on these observations, a technique for the local, spatially-controlled doping of functional molecules onto block copolymer templates is demonstrated using fluorescent boron-dipyrromethene laser dye as a molecular probe.

INTRODUCTION

Interactions between polymer and solvent are ubiquitous in materials processing, and applications increasingly demand precise control over polymer structure and function under environmental conditions. In nanolithography, solvent penetration during development determines the resolution achieved by polymeric resists for templating microelectronic patterns.[133] In drug delivery systems, solvation kinetics regulate the controlled release of active materials from a polymer substrate as well as the subsequent degradation of the matrix.[134] In membrane filtration, solvent interactions during fabrication and operation influence the selectivity, stability, and fouling rate of polymer nanopores.[135] In each of these applications, proper polymer functionality relies on careful understanding of solvation behavior at the nanoscale in and outside of equilibrium.

A statistical model describing the thermodynamics of network swelling was first developed by Flory and Rehner.[136,137] From their description, when a crosslinked polymer network is introduced to a solvent environment, entropy of mixing drives solvent into the polymer matrix, causing the material to expand. During this process, polymer chain configurations extend and reorganize to accommodate interactions with solvent molecules under the new chemical environment. Solvent continues to flow into the matrix until it reaches equilibrium where the osmotic pressure is balanced by tensile strain from chain extension. This theory has found remarkable success at predicting the behavior of unconfined, isotropic networks with low crosslink density. However, additional complexity is introduced when considering the swelling of structured and multi-component polymer networks due to structural anisotropy,[138] solvent selectivity,[139] and interfacial confinement.[140]

Block copolymers (BCP) have proven to be a natural system for studying structured polymer networks as a result of their native ability to self-assemble into periodic nanopatterns.[11,141] The structural regularity and definition of BCP patterns also offers potential utility for lithographic templating applications.[5,142] Thermodynamic incompatibility of the BCP blocks, as described by the Flory-Huggins interaction parameter χ, drives them to microphase separate into ordered domains. However, in ambient conditions below the glass transition temperature, as-cast BCP films typically become kinetically trapped in nonequilibrium structures. The introduction of solvent to the film enhances chain mobility and, under carefully controlled annealing conditions, may be used to direct the organization and alignment of BCP nanopatterns.[143] This procedure is most commonly performed using solvent vapor, but recent reports have also examined solution-processed assembly involving the complete immersion of BCP thin films.[144,145] In the solvated films, solvent molecules partition into the BCP matrix according to their relative affinity for each domain. The incorporation of selective solvents — *i.e.* solvents that are selectively miscible for one block — enhances block segregation, while the addition of non-selective solvents mitigates their incompatibility.[146] Selectively swollen BCP films may also be employed as templates, for *e.g.* mesostructured silica, by using the BCP architecture to control the distribution of a sol-gel precursor solution.[147]

In systems outside of equilibrium, the kinetics of polymer swelling are governed by competing rates for diffusion of the solvent and chain relaxation of the network. When these rates are comparable, swelling kinetics enter a non-Fickian regime classified as Case II diffusion as first described by Alfrey *et al.*[148] Case II kinetics are routinely observed experimentally and are characterized by three major features: (1) a sharp solvent front separating the swollen outer corona from the glassy core, (2) uniform solvent concentration behind the front, and (3) a linear

front velocity. In Case II swelling, solvent transport is mediated by relaxation of the glassy core at the solvent front, leading to a characteristic discontinuity in the concentration profile.[149,150] Mechanical deformation of the matrix at the front produces a tensile stress that balances osmotic pressure, hindering further solvation. However, as solvent penetrates the unswollen core, plasticization of the chains behind the advancing front causes each successive swelling element to rapidly swell to its equilibrium solvent concentration. The precise kinetics of this process are characteristic of specific solvent-polymer interactions and are also dependent on processing conditions,[150] film thickness,[151,152] and the degree of crosslinking,[153-155] among other factors.

In the present study, we have investigated the swelling equilibria and kinetics of poly(styrene-*block*-methyl methacrylate) (PS-*b*-PMMA) islands in cyclohexane as a model system of polymer swelling on the nanoscale. We prepare BCP films with a terraced lamellar architecture in which single-layer PS domains are insulated from the solvent environment by a PMMA overlayer. On this length scale, atomic force microscopy (AFM) allows *in situ* measurements of the swelling volume and force response without sample damage.[156] Utilizing the unique architecture of our system, we observe Case II swelling behavior and track the real-time progression of the solvent front for a series of polymer molecular weights. With this technique, it is now possible to directly investigate swelling kinetics at the limit of single-layer polymer films.

RESULTS AND DISCUSSION

BCP Terrace Morphology

Symmetric BCP thin films self-assemble to form lamellar nanostructures.[9] When oriented parallel to the surface, substrate-confined films adopt integral thicknesses τ following:

$$\tau = \frac{1}{2}nL_0; \qquad n = 1, 2, 3, \dots \tag{5.1}$$

where L_0 is the characteristic lamellar period, and where the number of layers n is even or odd for symmetric and asymmetric wetting conditions, respectively.[157-159] This constraint is enforced because deviations from quantized thicknesses result in an entropic penalty from chain stretching.[160] In the case of PS-*b*-PMMA, the lower surface energy PMMA block uniformly wets the Si substrate, but either block may coat the atmospheric interface due to similar values for the $\chi_{PS\text{-}air}$ and $\chi_{PMMA\text{-}air}$ Flory-Huggins interaction parameters.[158,159] Consequently, parallel lamella with both symmetric and asymmetric wetting can be observed in PS-*b*-PMMA thin films, and the blocks may coexist on the air surface at equilibrium.

When PS-*b*-PMMA films with incommensurate thickness are prepared, relief structures — such as islands, holes, or terraces — form to ensure locally commensurate thicknesses.[161] For our study, we examine thicknesses of $\tau \sim 0.75\ L_0$ in which PMMA islands ($\tau = L_0$) decorate a majority PS surface ($\tau = \frac{1}{2}\ L_0$). We prepared a series of such films with different molecular weight polymers, designated as P_{51} (M$_W$ = 51,000*)*, $P_{68.5}$ (M$_W$ = 68,500), and P_{89} (M$_W$ =89,000), and a summary of their characteristics is included in **Table 5.1**. Terrace thicknesses, as measured from the AFM height images, follow the familiar scaling law of $L_0 \propto N^{2/3}$ in which the extended chains reflect a balance between domain segregation and configurational entropy.[160] In **Figure 5.1.A** a representative height image of a $P_{68.5}$ shows the island topography, and, in **Figure 5.1.B**, the corresponding phase channel image shows the chemical composition of the surface. The AFM phase offset is determined by energy dissipation of the tip-surface interaction, and contrast arises due to differences in PS and PMMA viscoelasticity.[162,163] To highlight the structure of the step edges, a three-dimensional perspective of the topography is shown in **Figure 5.1.C** with an overlaid phase color map.

Table 5.1

Lamellar PS-*b*-PMMA properties. Physical properties — including weight-average molecular weight M_w, PS fraction f_{PS}, and polydispersity index PDI — of the polymers examined in this chapter.

	Mw (g/mol)	Mw PS (g/mol)	Mw PMMA (g/mol)	f_{PS}	PDI (M_W/M_N)
P_{51}	51,000	25,000	26,000	49%	1.06
$P_{68.5}$	68,500	35,000	33,500	51%	1.09
P_{89}	89,000	44,000	45,000	49%	1.12

Figure 5.1
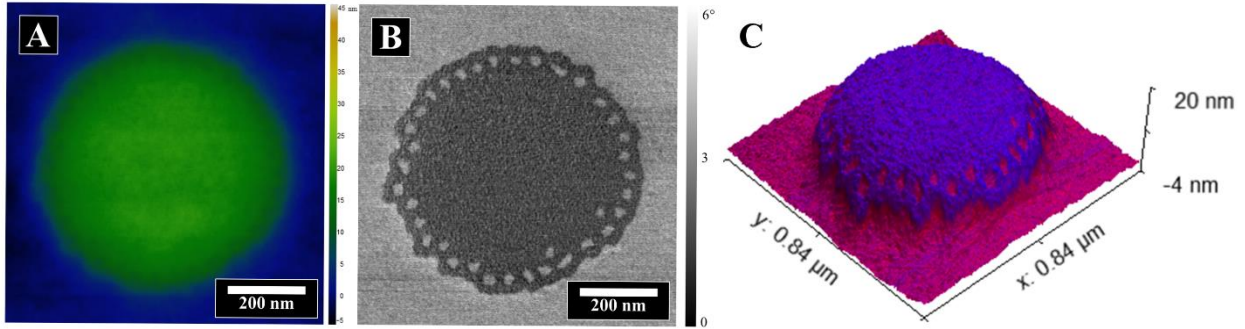
PS-*b*-PMMA island structure. AFM height (A) and phase (B) channel images showing the structure of a $P_{68.5}$ island in air. The phase image tracks the composition of the surface, with dark corresponding to PMMA and light to PS. (C) A three-dimensional view of the surface topography colored with an overlaid phase scale to highlight the structure of the island step edges, with blue corresponding to PMMA and red to PS.

Along the island step edges, we observe a complex domain morphology with bands of perpendicular domains, matching previous observations by Carvalho and Thomas[164] and by Liu *et al.*[165] The edge structure forms to accommodate the thickness discontinuity between islands and the background film. Islands represent topological defects in the film's lamellar structure and their edges correspond to prismatic loop dislocations.[165,166] In multilayer films, strain resulting from the curvature of the subsurface dislocation core is distributed between several polymer layers. However, in the case of single-layer films, as studied here, this strain cannot be sufficiently shared, and the edge tension is instead relieved by reorientation of the lamellar domains to form perpendicular lamellae.[165,167] The exposed PS domains along the step edge are connected bicontinuously to the internal lamellae with twist grain boundaries described by Scherk's surface,[164] which provides a channel for solvent to flow into the island interior during immersion experiments.

Selective Swelling

In our swelling experiments, we examine the infiltration of cyclohexane, a selective solvent for PS that does not dissolve PMMA. The PMMA islands include an internal PS layer, and, when dispersed in solvent, cyclohexane flows into the PS until it reaches equilibrium, causing the film to expand. Anchoring by the insoluble PMMA overlayer ensures a consistent island structure throughout the swelling process without the need for interchain crosslinking. AFM images in **Figures 5.2.A-C** track the changes in the equilibrium island thickness before solvent immersion, upon the introduction of cyclohexane, and following its subsequent removal. The polymer islands expand when immersed in cyclohexane, as measured by an increase in thickness. When cyclohexane is removed, and the samples are dried, the swelling is found to be

96

Figure 5.2
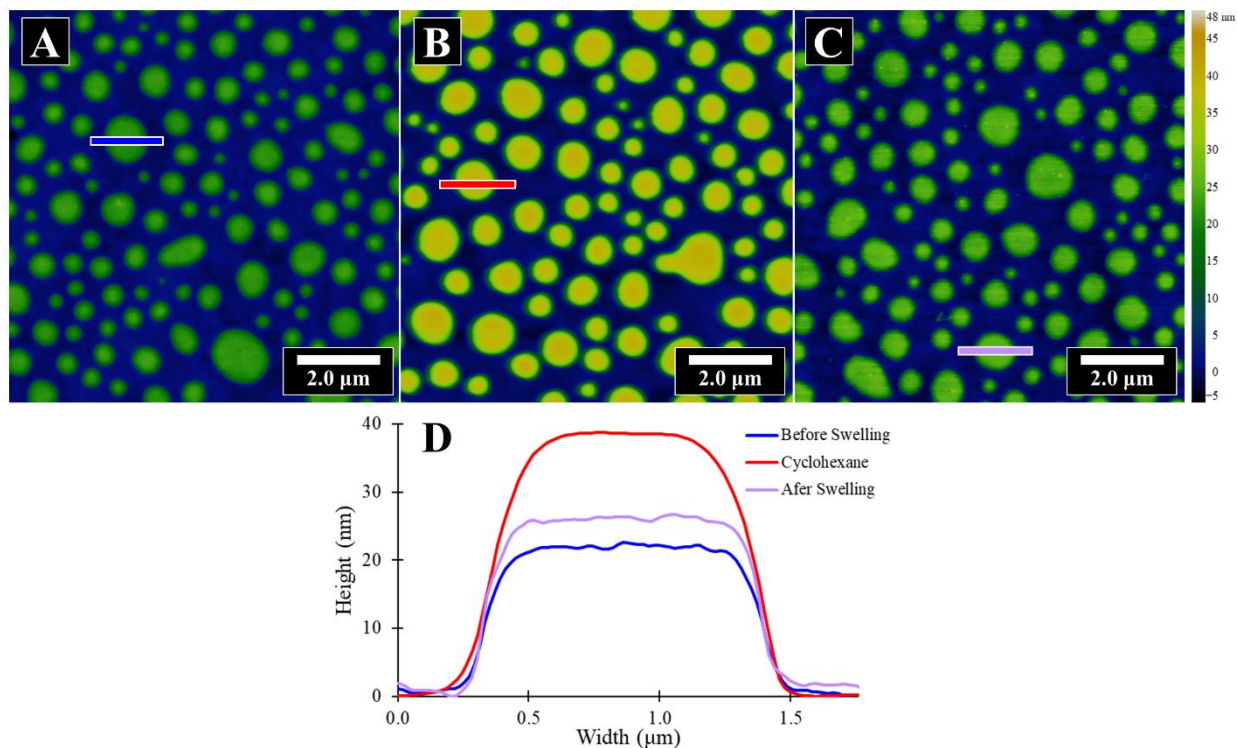
Reversible swelling of PS-*b*-PMMA islands. AFM height images of $P_{68.5}$ islands before swelling (A), during cyclohexane immersion (B), and after solvent evaporation (C). Line profiles of the islands (D) show the change in island thickness due to solvent swelling. The swelling process is reversible following solvent removal, but the islands do not fully return to their original thickness.

reversible. However, the polymer islands do not completely return to their initial thickness. The deswollen thickness remains constant when measured 24 h following solvent removal, indicating that the change is a consequence of limited chain plasticity during deswelling, rather than the result of residual solvent. PS chains initially contract during solvent evaporation, but once all the solvent is removed, the polymer morphology is kinetically quenched, preventing the islands from continuing to deswell.[143]

AFM height profiles, as plotted in **Figure 5.2.D**, provide a direct measure of solvent incorporation. Under the assumption that cyclohexane is localized to the PS domains, the swelling ratio Q may be calculated as:

$$Q = (\tau_{swol} - \tau_{PMMA})/(\tau - \tau_{PMMA}) \tag{5.2}$$

where τ is the thickness of the unswollen film, τ_{swol} is the thickness of the swollen film, and $\tau_{PMMA} = \frac{1}{2} \tau$ is the thickness of the PMMA capping layer. The solvent content is then:

$$\phi_{cyl} = (1 - \phi_{PS}) = 1 - Q^{-1} \tag{5.3}$$

where ϕ_{cyl} and ϕ_{PS} are the respective volume fractions of cyclohexane and PS. Measured swollen and unswollen thicknesses for each polymer are reported in **Table 5.2** alongside resulting values of Q and ϕ_{cyl}.

From Flory-Rehner theory, the difference between the chemical potential of cyclohexane in the PS matrix μ_{cyl}^{PS} and of the pure solvent μ_{cyl}^{0} is determined as:

$$\mu_{cyl}^{PS} - \mu_{cyl}^{0} = RT \left[\ln(\phi_{cyl}) + (1 - \phi_{cyl}) + \chi_{cyl-PS}(1 - \phi_{cyl})^2 \right] \tag{5.4}$$

where R is the molar gas constant, T is temperature, and $\chi_{cyl\text{-}PS}$ is the Flory-Huggins interaction parameter between cyclohexane and PS.[14] At equilibrium, μ_{cyl}^{PS} and μ_{cyl}^{0} are balanced, and we set Equation (5.4) to zero. Note that this expression is equivalent to the first term of the Flory-

Table 5.2

Island swelling during cyclohexane immersion. PS-*b*-PMMA island swelling parameters during cyclohexane immersion. From the swelling ratio Q we obtain the solvent fraction ϕ_{cyl} and the interaction parameter between cyclohexane and polystyrene $\chi_{cyl\text{-}PS}$.

	τ (nm)	τ_{swol} (nm)	Q	ϕ_{cyl}	$\chi_{cyl\text{-}PS}$
P_{51}	14.3 ± 0.7	23.0 ± 1.1	2.2 ± 0.2	0.55 ± 0.04	0.73 ± 0.03
$P_{68.5}$	20.1 ± 0.9	34.7 ± 2.4	2.5 ± 0.3	0.60 ± 0.05	0.69 ± 0.04
P_{89}	28.0 ± 1.0	45.1 ± 3.5	2.2 ± 0.3	0.55 ± 0.06	0.73 ± 0.05

Rehner equation for polymer swelling but neglects the effects of network tension, because our system is uncrosslinked.[136] From our measured swelling ratios, we obtain values of $\chi_{cyl\text{-}PS} = 0.73 \pm 0.03$ for P_{51}, and $\chi_{cyl\text{-}PS} = 0.69 \pm 0.04$ for $P_{68.5}$, and $\chi_{cyl\text{-}PS} = 0.73 \pm 0.05$ for P_{89} at 25 °C. In general, for a given polymer-solvent system, χ is sensitive to a number of factors including temperature, volume fraction, polymer molecular weight, and chain architecture. Our values compare well with previous reported measurements of $\chi_{cyl\text{-}PS} = 0.64$ with $M_W = 25{,}000$ g/mol PS homopolymer and $\phi_{cyl} = 0.6$ at 34 °C.[168] In our system, the PS block is constrained by its connection to the BCP interface, limiting solvent interactions and leading to a general increase in $\chi_{cyl\text{-}PS}$ with respect to the homopolymer.

Solvent swelling is accompanied by softening of the polymer islands. When a swollen film at equilibrium is compressed, solvent is expelled, and its elasticity therefore scales according to the osmotic pressure of the solvent in the network.[169] The material change under cyclohexane is qualitatively evident in the increased contrast of AFM phase imaging, which is sensitive to the sample viscoelasticity, as shown in **Figures 5.3.A** and **B**. When the probe interacts with the softer, solvent-swollen islands, energy dissipation leads to a larger phase offset.[32] This change in mechanical response can be more closely examined through AFM indentation experiments comparing the elasticity of swollen and unswollen islands of $P_{68.5}$.[170] We collected force curves under immersion examining the sample at a set of the same positions before and after swelling: two points on islands and two on the background polymer film, with 20 measurements for each sample position. Observations were consistent across the measurements, and representative force curves are shown in **Figures 5.3.C** and **D** for the background and island regions, respectively. The islands show a softer, less steep response

Figure 5.3
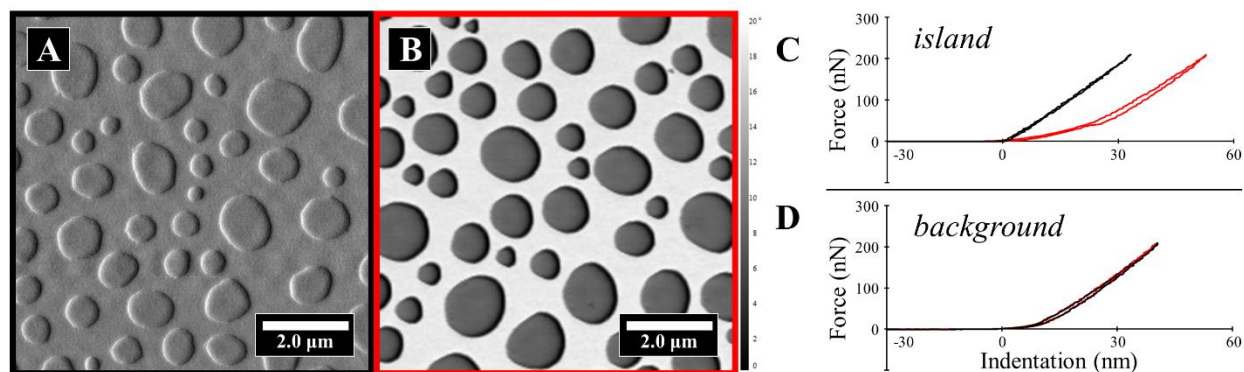
Force response of swollen islands. AFM phase images of $P_{68.5}$ islands in air (A) and under cyclohexane (B). The phase contrast is enhanced under cyclohexane because the soft, solvent-swollen islands increase energy dissipation of the tip-surface interaction. Extension and retraction force curves of polymer islands (C) and of the background film (D) as measured by AFM indentation experiments under cyclohexane. In each plot, the black curve corresponds to measurements before swelling and the red curve to measurements after swelling. The change in force response shows softening of the swollen. Over the same period, the force response of the background remained consistent.

following solvent penetration, reflecting the change from a glassy matrix to a rubbery gel. Over the same time interval, the background is unchanged and maintains a consistent response.

During AFM imaging, solvent-swollen terraces were observed to be sensitive to interactions from the AFM scanning probe. The soluble PS layer in the polymer islands is not covalently linked to the background film but does not fully dissolve because it is insulated from the solvent by an insoluble PMMA overlayer. The PMMA is tenuously anchored only along island step-edges, and we are able to disrupt this connection with the scanning action of the AFM probe. **Figure 5.4.A** shows a large-area view of the polymer sample imaged with a "gentle" amplitude set point of 800 mV, 80% of the cantilever free amplitude in solution, to avoid sample damage. A small inset region shown in **Figure 5.4.C** was then imaged with a "strong" amplitude setpoint of 300 mV, sufficient to push the tip into the polymer islands. Under these conditions, islands are removed from the surface by the AFM scanning action yielding a flat, single-layer film. We note that islands are unperturbed when this procedure is performed in air. Following removal, the exposed area below the islands lies flush with the height of the background film and is imprinted with patterns matching the locations of former island sites. Island edges reflect dislocations in the lamellar structure, and the underlying defects become visible after removing the top polymer layer.[166] A second large-area image, **Figure 5.4.B**, was then obtained with the "gentle" 800 mV setpoint after removing the islands, revealing that surface features outside of the scan area were undisturbed. Fragments of the removed islands are visible, seen in **Figure 5.4.B**, as white features, in the region surrounding the scan area, but do not fully account for the removed polymer. The remaining balance of detached polymer is likely dispersed as micelles in the solvent environment.

Figure 5.4
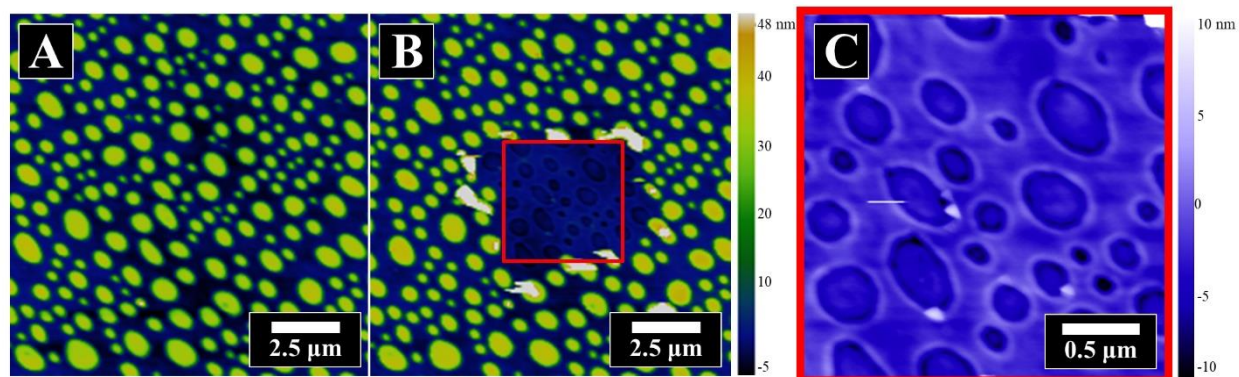
AFM abrasion of swollen islands. AFM height images of a region of swollen $P_{68.5}$ islands under cyclohexane before (A) and after (B) abrading the surface with the AFM probe. The inset region in (C) was scanned with a low-amplitude setpoint to depress the cantilever into the surface and controllably remove a layer of polymer islands. After removing the islands, the surface is imprinted with patterns corresponding to the island step edges.

Swelling Kinetics

AFM imaging immediately following cyclohexane immersion enables time-resolved investigation of swelling behavior outside of equilibrium. The time evolution of $P_{68.5}$ swelling is shown in **Figure 5.5** over a series of AFM images. For each island, swelling is observed to initiate along step edges and then spread inward over time until the island is uniformly solvated. Cyclohexane penetrates the single-layer PS domain along the bicontinuous step edge where it is exposed to the solvent, but the PS is otherwise protected by the PMMA overlayer. In these images, a sharp solvent front separates the uniformly swollen corona from the unswollen core, consistent with a Case II diffusion mechanism.[148] Case II behavior on the nanoscale has previously been observed in ultrathin polymer films through optical ellipsometry.[152] However, direct AFM imaging of the solvent front was not accessible in these systems, because the front propagates into the film, perpendicular to the imaging plane. Height cross-sections of the AFM images, as shown in **Figure 5.5**, show a discontinuous solvent concentration profile, from which we can track the motion of the front. From these width measurements, we find that the front propagates linearly, validating the mechanism as Case II diffusion, and with rate $s = 0.29 \pm 0.02$ nm/s. The timing of these measurement was scaled based on the *y*-axis position of the solvent front in each image to account for the AFM raster time. Through comparison over multiple samples, diffusion kinetics are found to be independent of terrace size or shape. The same mechanism and rate are also observed on slightly thicker films where the islands connect to form large terraces ($T = L_0$) with inlaid holes ($T = \frac{1}{2} L_0$).

As discussed above, upon swelling the islands expand significantly along the surface normal with swelling ratios $Q > 2$. In contrast, we measure no expansion parallel to the substrate; when tracking the swelling of individual islands, the area footprint of each island remains

Figure 5.5
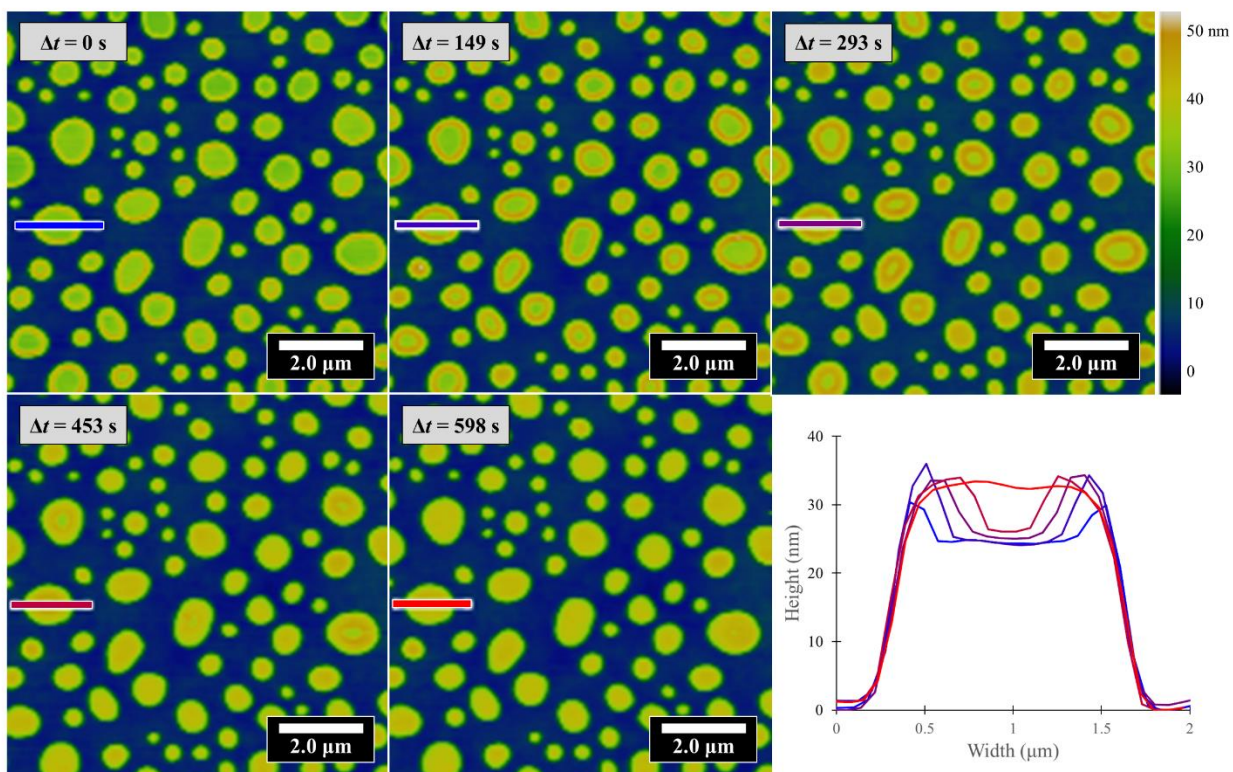
Solvent swelling dynamics. A time series of AFM height images of $P_{68.5}$ islands under cyclohexane. A sharp swelling front initiates along the island step edges and then uniformly propagates until the islands swell to their equilibrium thickness. Corresponding height cross sections track the progression of the solvent front.

constant throughout the swelling process. This large swelling anisotropy results from the structural anisotropy of the BCP film. PS chains extend freely normal to the BCP interfaces but are laterally confined by covalent tethering to the PS/PMMA boundary, which restricts extension parallel to the lamellar structure.[171] Similar anisotropy has been observed by Meier, who examined lamellar networks composed of crosslinked triblock elastomers.[172] In thick, globally aligned systems, the orientation of the microstructure directly translates to bulk swelling anisotropy on the macroscale.

Previous measurements of the swelling rate of bulk PS samples in cyclohexane have shown strong dependence on the degree of crosslinking, which determines the average chain length between network junctions.[153,154] In highly crosslinked networks, chain rearrangements are hindered which limits conformational changes and causes the swelling rate to decrease.[155] In our single-layer system, the PS is not crosslinked, but is instead covalently tethered to the PMMA. As a proxy for crosslink density, we compared swelling kinetics as a function of molecular weight, which correspondingly determines the unrestricted chain length. Our system is not a perfect analog, however, as the PS chains in the BCP islands have only one bound chain end and one free end.

Figures 5.6.A and **B** show time series for solvent penetration of P_{51} and P_{89} islands, respectively. Plots of the front motion for each molecular weight are collected in **Figure 5.6.C**. Over this range of samples, we observe that the front propagation rate is independent of molecular weight. In general, singly-bound chains do not contribute elastic resistance against solvent swelling, and we expect that changing the length of unrestricted chains will not significantly influence the swelling rate.[136]

Figure 5.6
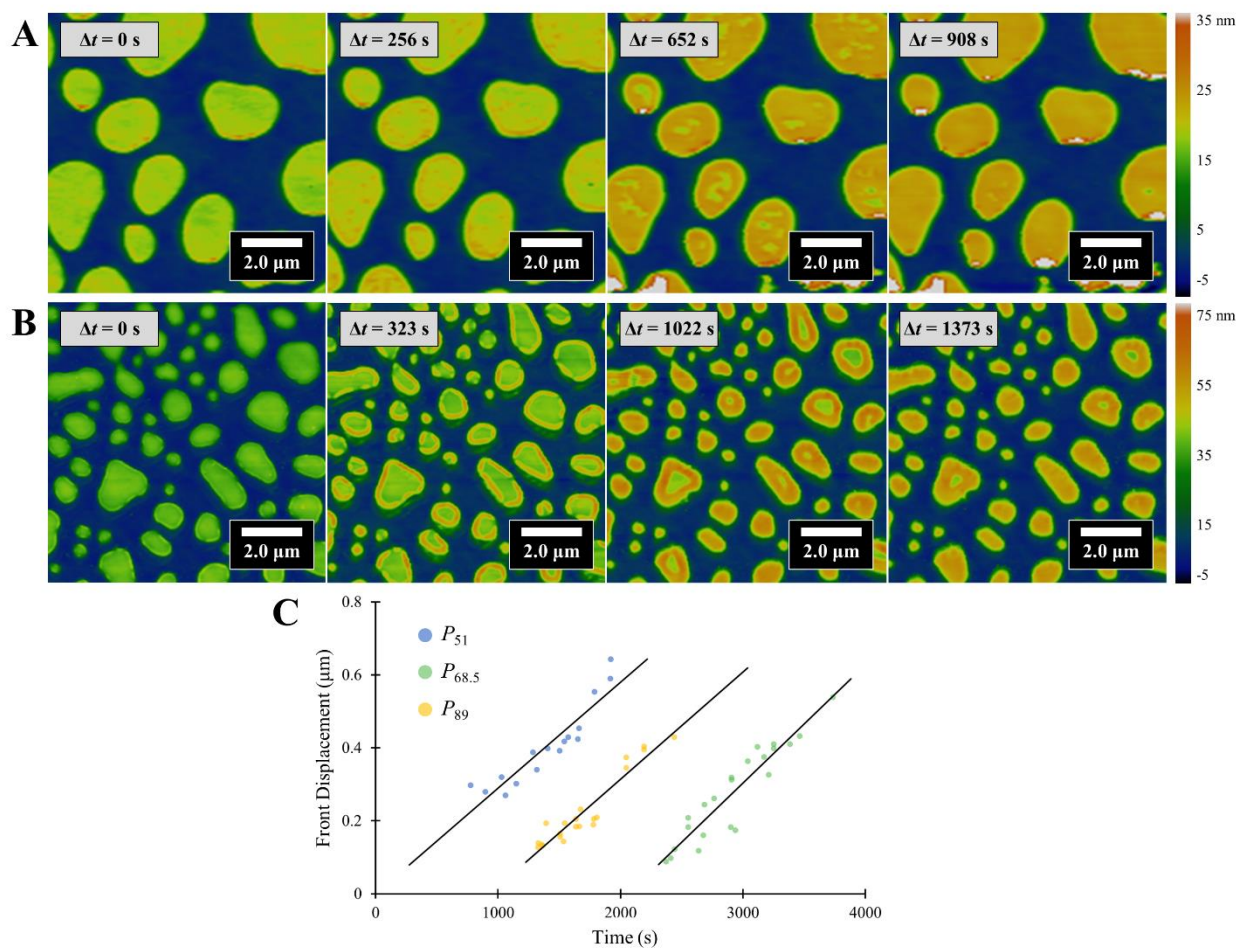
Swelling kinetics over a molecular weight series. Time series of AFM height images showing the swelling of P_{51} (A) and P_{89} (B) islands under cyclohexane. (C) The motion of the solvent front is plotted over time for each sample. The starting time for each data series has been offset for clarity. Solvent fronts are observed to propagate linearly, consistent with Case II diffusion. The rate of front propagation is found to be independent of molecular weight, with $s(P_{51}) = 0.29 \pm 0.03$ nm/s, $s(P_{68.5}) = 0.29 \pm 0.02$ nm/s, and $s(P_{89}) = 0.33 \pm 0.03$ nm/s.

Although the diffusion rate remains constant, comparison of the AFM time series shows a different solvent penetration mechanism for P_{51}. In this sample, the front initiates at many internal points on the island surface in addition to the perimeter. We still identify specific initiation sites, however, indicating that the solvent does not diffuse homogeneously through the film. In this case, the PMMA capping layer is thinner and defects in the film create nanochannels for direct cyclohexane penetration to the PS. Solvent fronts, both internal and from the edge, propagate linearly at the same rate until they ultimately coalesce to form a uniformly swollen island.

Fluorescence Imaging

Solution immersion is frequently employed to incorporate functional materials into polymer matrices. In polymer swelling experiments, stains are used as indirect assays of the solvent distribution. When working with structured BCP patterns, chemically selective swelling enables the deposition of functional materials with controlled spatial heterogeneity. As an example, Hayward *et al.* selectively incorporated sol-gel precursors into the poly(2-vinylpyridine) (P2VP) domains of a PS-*b*-P2VP film for the fabrication of nanoporous silica.[147] Here we demonstrate that kinetic control over molecular staining provides an additional pathway for spatial patterning and localization on BCP terraces.

To test this idea, we immersed BCP thin films in saturated solutions of 1,3,5,7,8-pentamethylpyrromethene-difluoroborate (BODIPY) laser dye for a series of immersion times. While the samples are immersed, the solvent diffuses into the terraces, but, once removed, the islands deswell, arresting further solvent penetration. The doped samples were then imaged by rastering a focused 473 nm laser over a 10×10 μm area to locally excite the incorporated

Figure 5.7
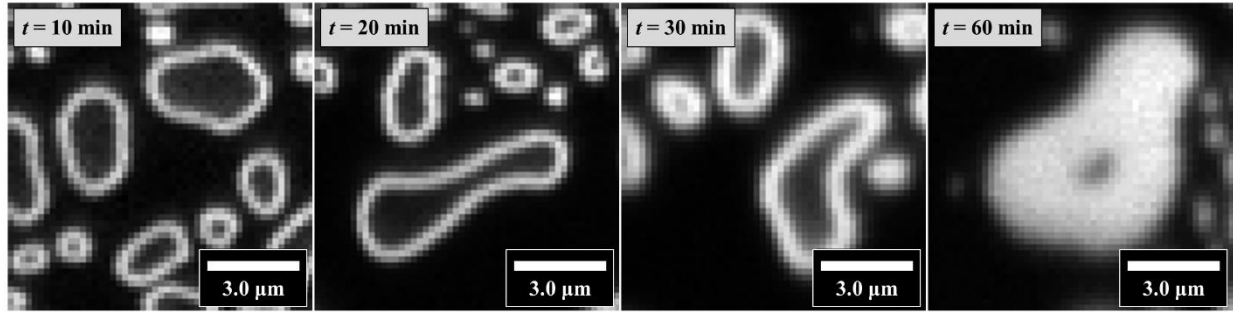
Fluorescent doping of PS-*b*-PMMA islands. Fluorescence maps of $P_{68.5}$ islands following immersion in saturated BODIPY in cyclohexane solutions for a series of doping times. The samples were excited using a 473 nm laser and rastered over a 10×10 µm area with a point resolution of 200 nm. The maps were plotted by measuring the integrated fluorescence intensity over 495-510 nm. Fluorescent BODIPY molecules are locally dispersed in the films according to the time-dependent penetration of the cyclohexane carrier solution.

fluorophore. A broad fluorescence signal was collected for each point, and intensities were integrated over 495-510 nm to produce an image. **Figure 5.7** shows fluorescence maps for island samples for a series of immersion times.

From these images, we find that the fluorophore is confined to the perimeter of block copolymer islands. The fluorescence signal in the film is consistent with the pattern of cyclohexane uptake observed by *in situ* AFM; the BODIPY distribution is characteristic of Case II kinetics with a sharp front and uniform concentration behind the front. Increasing the immersion time increased the extent of BODIPY infiltration without changing the fluorescence intensity. The sharply defined solvent front of cyclohexane diffusion directly translates to precise kinetic control over molecular doping.

CONCLUSION

In this chapter, AFM imaging was used to investigate the *in situ* swelling behavior of terraced PS-*b*-PMMA films in cyclohexane. The terraced structure includes insulated lamellar domains that allow examination of the swelling of a single PS layer, while preventing dissolution of the film. The lateral orientation of the PS domains in our system enables direct AFM imaging and indentation measurements throughout the two-dimensional swelling process. We find that solvent penetrates along the island step edges, but that the PS domains are protected at the surface by a PMMA capping layer. Outside of equilibrium, the swelling follows a Case II diffusion mechanism, characterized by the linear propagation of a sharp solvent front, and, for our uncrosslinked system, the front velocity is independent of molecular weight. However, with low molecular weight P_{51} films, solvent permeates the thin PMMA overlayer and we identify multiple internal initiation sites for solvent diffusion. In equilibrated samples, we observe

uniform swelling with highly anisotropic expansion due to interfacial confinement of the PS chains. The solvent-swollen islands also soften and become susceptible to interaction and damage from the AFM cantilever.

Understanding of the interplay between polymer and solvent is increasingly critical to nanoscale engineering challenges, and, based on our observations of swelling kinetics, we examine the use BCP islands as templates for functional additives. With fluorescence mapping, we demonstrate that kinetic control alongside chemical selectivity provides a pathway for controlling the distribution of BODIPY fluorophore in the polymer film. PS-b-PMMA islands serve as a model system for the continued investigation of nanoscale swelling behavior.

METHODS

PS-b-PMMA copolymer was obtained from Polymer Source, Inc. Three lamella-forming polymer samples with differing molecular weights were used, designated P_{51}, $P_{68.5}$, and P_{89}. A summary of their characteristics is detailed above in Table 5.1. The silicon wafer substrates were ultrasonically cleaned with toluene, acetone, and isopropanol and dried with nitrogen gas before polymer deposition. Polymer films were spin-coated from solutions of 0.8-1.0 wt% PS-*b*-PMMA in toluene at 3000-4000 rpm for 60 s and then thermally annealed at 250 °C for 2 h under argon to achieve terrace formation. To verify the fabrication of single-layer films, polymer thicknesses were measured using a Gaertner Waferskan ellipsometer.

The samples were imaged in an open liquid cell with an Asylum Research MFP-3D AFM and immersed in cyclohexane immediately prior to imaging. Imaging was performed in fluid AC (tapping) mode, using Olympus AC240TS cantilevers with average spring constants of 2 N/m and with tetrahedral tips of radius 7 nm. Specific scanning parameters varied between cantilevers and samples based on operating conditions. In general, when imaging in liquid, the set-point amplitude was set to 80% of the free-oscillation amplitude to avoid disturbance or damage at the polymer/fluid interface.

For nanoindentation experiments, the samples were initially imaged following cyclohexane immersion but before solvent penetration into the island interior to identify regions of interest. Four points were selected; two on islands and two on the background polymer. At each point, a set of 20 force curves was obtained by depressing the AFM tip into the surface until it reached a 1.0 V deflection set-point. Following a roughly 30 min sample equilibration period, the sampled was imaged again to ensure complete swelling of the islands and to locate the previously analyzed sample positions. Force measurements were then repeated at these points to

determine the change in mechanical response due to solvent swelling. All force curves were obtained using a single cantilever with a spring constant of 2.95 N/m and with an inverse optical lever sensitivity of 70.8 nm/V.

Fluorescence samples were prepared by immersing the polymer films *ex situ* in shallow solutions of 1,3,5,7,8-pentamethylpyrromethene-difluoroborate complex (BODIPY) laser dye dissolved in cyclohexane. The dye was purchased from Exciton under the trade name pyrromethene 546. Saturated solutions were prepared by fully dissolving 10 mg of BODIPY in 2 mL cyclohexane and decanting to remove excess solute. For each sample. the immersion time was adjusted to control the kinetically limited incorporation of BODIPY. Fluorescence maps were then acquired using a confocal Horiba LabRAM HR Evolution Raman spectrometer. A 473 nm laser was focused on the samples and rastered over a 10×10 µm area to excite a fluorescent signal, which was collected with a diffraction-limited 200 nm resolution. Images were created using the integrated fluorescence intensity over 495-510 nm for each pixel.

References.

1. Robotti, R. TPEs in Automotive Applications. In *Thermoplastic Elastomers II: Processing for Performance*. Rapra Technology Limited, **1989**.

2. Brown, H. R. Effect of a Diblock Copolymer on the Adhesion between Incompatible Polymers. *Macromolecules* **1989**, *22*, 2859−2860.

3. Hustad, P. D.; Marchand, G. R.; Garcia-Meitin, E. I.; Roberts, P. L.; Weinhold, J. D. Photonic Polyethylene from Self-Assembled Mesophases of Polydisperse Olefin Block Copolymers. *Macromolecules* **2009**, *42*, 3788−3794.

4. Soppimath, K. S.; Aminabhavi, T. M.; Kulkarni, A. R.; Rudzinski, W. E. Biodegradable Polymeric Nanoparticles as Drug Delivery Devices. *J. Control. Release* **2001**, *70*, 1−20.

5. Bates, C. M.; Maher, M. J.; Janes, D. W.; Ellison, C. J.; Willson, C. G. Block Copolymer Lithography. *Macromolecules* **2013**, *47*, 2−12.

6. Kim, H.; Park, S.; Hinsberg, W. D. Block Copolymer Based Nanostructures: Materials, Processes, and Applications to Electronics. *Chem. Rev.* **2010**, *110*, 146−177.

7. Bockstaller, M. R.; Mickiewicz, R. A.; Thomas, E. L. Block Copolymer Nanocomposites: Perspectives for Tailored Functional Materials. *Adv. Mater.* **2005**, *17*, 1331−1349.

8. Tong, Q.; Malachosky, E. W.; Raybin, J.; Guyot-Sionnest, P.; Sibener, S. J. End-to-End Alignment of Gold Nanorods on Topographically Enhanced Cylinder-Forming Diblock Copolymer Templates and Their Surface Enhancing Raman Properties. *J. Phys. Chem. C* **2014**, *118*, 19259−19265.

9. Liu, C. C.; Ramírez-Hernández, A.; Han, E.; Craig, G. S. W.; Tada, Y.; Yoshida, H.; Kang, H.; Ji, S.; Gopalan, P.; de Pablo, J. J.; Nealey, P. F. Chemical Patterns for Directed Self-Assembly of Lamellae-Forming Block Copolymers with Density Multiplication Features. *Macromolecules* **2013**, *46*, 1415−1424.

10. Raybin, J.; Ren, J.; Chen, X.; Gronheid, R.; Nealey, P. F.; Sibener, S. J. Real-Time Atomic Force Microscopy Imaging of Block Copolymer Directed Self Assembly. *Nano Lett.* **2017**, 7717−7723.

11. Darling, S. B. Directing the Self-Assembly of Block Copolymers. *Progress in Polymer Science* **2007**, *32*, 1152−1204.

12. Sundrani, D.; Darling, S. B.; Sibener, S. J. Guiding Polymers to Perfection: Macroscopic Alignment of Nanoscale Domain. *Nano Lett.* **2004**, *4*, 273−276.

13. Liu, C. C.; Thode, C. J.; Delgadillo, P. A. R.; Craig, G. S.; Nealey, P. F.; Gronheid, R. Towards an All-Track 300 mm Process for Directed Self-Assembly. *J. Vac. Sci. Technol B* **2011**, *29*, 06F203.

14. Segal-Peretz, T.; Winterstein, J.; Doxastakis, M.; Ramírez-Hernández, A.; Biswas, M.; Ren, J.; Suh, H. S.; Darling, S. B.; Liddle, J. A.; Elam, J. W.; de Pablo, J. J.; Zaluzec, N. J.; Nealey, P. F. Characterizing the Three-Dimensional Structure of Block Copolymers via Sequential Infiltration Synthesis and Scanning Transmission Electron Tomography. *ACS Nano* **2015**, *9*, 5333−5347.

15. van Franeker, J. J.; Hermida-Merino, D.; Gommes, C.; Arapov, K.; Michels, J. J; Janssen, R. A. J.; Portale, G. Sub-Micrometer Structure Formation during Spin Coating Revealed by Time-Resolved In Situ Laser and X-Ray Scattering. *Adv. Funct. Mat.* **2017**, *27*, 1702516.

16. Yufa, N. A.; Li, J.; Sibener, S. J. Diblock Copolymer Healing. *Polymer* **2009**, *50*, 2630−2634.

17. Tong, Q; Sibener, S. J. Visualization of Individual Defect Mobility and Annihilation within Cylinder-Forming Diblock Copolymer Thin Films on Nanopatterned Substrates. *Macromolecules* **2013**, *46*, 8538−8544.

18. Tong, Q.; Zheng, Q.; Sibener, S. J. Alignment and Structural Evolution of Cylinder-Forming Diblock Copolymer Thin Films in Patterned Tapered-Width Nanochannels. *Macromolecules* **2014**, *47*, 4236−4242.

19. Ryu, H. J.; Tong, Q.; Sibener, S. J. Time-Resolved Analysis of Domain Growth and Alignment of Cylinder-Forming Block Copolymers Confined within Nanopatterned Substrates. *J. Phys. Chem. Lett.* **2013**, *4*, 2890–2895.

20. Darling, S. B.; Yufa, N. A.; Cisse, A. L.; Bader, S. D.; Sibener, S. J. Self-Assembly of FePt Nanoparticles on Photochemically Modified Diblock Copolymer Templates. *Adv. Mater.* **2005**, *17*, 2446−2450.

21. Peng, Q.; Tseng, Y.-C.; Darling, S. B.; Elam, J. W. A Route to Nanoscopic Materials via Sequential Infiltration Synthesis on Block Copolymer Templates. *ACS Nano* **2011**, *5*, 4600−4606.

22. Hur, S. M.; Thapar, V.; Ramírez-Hernández, A; Nealey, P. F.; de Pablo, J. J. Defect Annihilation Pathways in Directed Assembly of Lamellar Block Copolymer Thin Films. *ACS Nano* **2018**, *12*, 9974−9981.

23. Park, C.; Yoon, J.; Thomas, E. L. Enabling Nanotechnology with Self Assembled Block Copolymer Patterns. *Polymer* **2003**, *44*, 6725−6760.

24. Angelescu, D. E.; Waller, J. H.; Adamson, D. H.; Deshpande, P.; Chou, S. Y.; Register, R. A.; Chaikin, P. M. Macroscopic Orientation of Block Copolymer Cylinders in Single-Layer Films by Shearing. *Adv. Mater.* **2004**, *16*, 1736−1740.

25. Amundson, K.; Helfand, E.; Quan, X.; Hudson, S. D.; Smith, S. D. Alignment of Lamellar Block Copolymer Microstructure in an Electric Field. 2. Mechanisms of Alignment. *Macromolecules* **1994**, *27*, 6559−6570.

26. Tong, Q.; Sibener, S. J. Electric Field Induced Control and Switching of Block Copolymer Domain Orientations in Nanoconfined Channel Architectures. *J. Phys. Chem. C* **2014**, *118*, 13752–13756.

27. Ouk Kim, S.; Solak, H. H.; Stoykovich, M. P.; Ferrier, N. J.; de Pablo, J. J.; Nealey, P. F. Epitaxial Self-Assembly of Block Copolymers on Lithographically Defined Nanopatterned Substrates *Nature* **2003**, *424*, 411–414.

28. Ji, S.; Wan, L.; Liu, C.-C.; Nealey, P. F. Directed Self-Assembly of Block Copolymers on Chemical Patterns: A Platform for Nanofabrication. *Prog. Polym. Sci.* **2016**, *54*, 76–127.

29. Bita, I.; Yang, J. K. W.; Jung, Y. S.; Ross, C. A.; Thomas, E. L.; Berggren, K. K. Graphoepitaxy of Self-Assembled Block Copolymers on Two-Dimensional Periodic Patterned Templates. *Science* **2008**, *321*, 939–943.

30. Hur, S.-M.; Thapar, V.; Ramírez-Hernández, A.; Khaira, G.; Segal-Peretz, T.; Rincon-Delgadillo, P. A.; Li, W.; Müller, M.; Nealey, P. F.; de Pablo, J. J. Molecular Pathways for Defect Annihilation in Directed Self-Assembly. *Proc. Natl. Acad. Sci.* **2015**, *112*, 14144–14149.

31. Li, W.; Nealey, P. F.; de Pablo, J. J.; Müller, M. Defect Removal in the Course of Directed Self-Assembly is Facilitated in the Vicinity of the Order-Disorder Transition. *Phys. Rev. Lett.* **2014**, *113*, 168301.

32. Li, W.; Müller, M. Defects in the Self-Assembly of Block Copolymers and Their Relevance for Directed Self-Assembly *Annu. Rev. Chem. Biomol. Eng.* **2015**, *6*, 187–216.

33. Paik, M. Y.; Bosworth, J. K.; Smilges, D.-M.; Schwartz, E. L.; Andre, X.; Ober, C. K. Reversible Morphology Control in Block Copolymer Films via Solvent Vapor Processing: An In Situ GISAXS Study. *Macromolecules* **2010**, *43*, 4253–4260.

34. Gu, X.; Gunkel, I.; Hexemer, A.; Gu, W.; Russell, T. P. An In Situ Grazing Incidence X-Ray Scattering Study of Block Copolymer Thin Films During Solvent Vapor Annealing. *Adv. Mater.* **2014**, *26*, 273–281.

35. Harrison, C.; Adamson, D. H.; Cheng, Z.; Sebastian, J. M.; Sethuraman, S.; Huse, D. A.; Register, R. A.; Chaikin, P. M. Mechanisms of Ordering in Striped Patterns. *Science* **2000**, *290*, 1558−1560.

36. Welander, A. M.; Kang, H.; Stuen, K. O.; Solak, H. H.; Müller, M.; de Pablo, J. J.; Nealey, P. F. Rapid Directed Assembly of Block Copolymer Films at Elevated Temperatures. *Macromolecules* **2008**, *41*, 2759–2761.

37. Ruiz, R.; Bosworth, J. K.; Black, C. T. Effect of Structural Anisotropy on the Coarsening Kinetics of Diblock Copolymer Striped Patterns. *Phys. Rev. B* **2008**, *77*, 54204.

38. Russell, T. P.; Hjelm, R. P.; Seeger, P. A. Temperature Dependence of the Interaction Parameter of Polystyrene and Poly(Methyl Methacrylate). *Macromolecules* **1990**, *23*, 890–893.

39. Mansky, P.; Liu, Y.; Huang, E.; Russell, T. P.; Hawker, C. Controlling Polymer-Surface Interactions with Random Copolymer Brushes. *Science* **1997**, *275*, 1458−1460.

40. Rincon Delgadillo, P. A.; Gronheid, R.; Thode, C. J.; Wu, H.; Cao, Y.; Somervell, M.; Nafus, K.; Nealey, P. F. All Track Directed Self-Assembly of Block Copolymers: Process Flow and Origin of Defects, Proc. SPIE 8328, *Alternative Lithographic Technologies IV*, 83230D (Mar 21, 2012)

41. Fredrickson, G. H.; Bates, F. S. Dynamics of Block Copolymers: Theory and Experiment. *Annu. Rev. Mater. Sci.* **1996**, *26*, 501−550.

42. Bates, C. M.; Bates, F. S. 50th Anniversary Perspective: Block Polymers—Pure Potential. *Macromolecules* **2016**, *50*, 3−22.

43. Ruiz, R.; Kang, H.; Detcheverry, F. A.; Dobisz, E.; Kercher, D. S.; Albrecht, T. R.; de Pablo, J. J.; Nealey P. F. Density Multiplication and Improved Lithography by Directed Block Copolymer Assembly. *Science* **2008**, *321*, 936−939

44. Sundrani, D.; Darling, S. B.; Sibener, S. J. Hierarchical Assembly and Compliance of Aligned Nanoscale Polymer Cylinders in Confinement. *Langmuir* **2004**, *20*, 5091−5099.

45. Cheng, J. Y.; Ross, C. A.; Thomas, E. L.; Smith, H. I.; Vancso, G. J. Templated Self-Assembly of Block Copolymers: Effect of Substrate Topography. *Adv. Mater.* **2003**, *15*, 1599−1602.

46. Ryu, H. J.; Tong, Q.; Sibener, S. J. Time-Resolved Analysis of Domain Growth and Alignment of Cylinder-Forming Block Copolymers Confined within Nanopatterned Substrates. *J. Phys. Chem. Lett.* **2013**, *4*, 2890−2895.

47. Li, W.; Müller, M. Directed Self-Assembly of Block Copolymers by Chemical or Topographical Guiding Patterns: Optimizing Molecular Architecture, Thin-Film Properties, and Kinetics. *Prog. Polym. Sci.* **2015**, *54−55*, 47−75.

48. Garner, G. P.; Delgadillo, P. R.; Gronheid, R.; Nealey, P. F.; de Pablo, J. J. Design of Surface Patterns with Optimized Thermodynamic Driving Forces for the Directed Self-Assembly of Block Copolymers in Lithographic Applications. *Mol. Syst. Des. Eng.* **2017**, *2*, 567−580.

49. Li, W.; Müller, M. Thermodynamics and Kinetics of Defect Motion and Annihilation in the Self-Assembly of Lamellar Diblock Copolymers. *Macromolecules* **2016**, *49*, 6126−6138.

50. Stoykovich, M. P.; Daoulas, K. C.; Müller, M.; Kang, H.; de Pablo, J. J.; Nealey, P. F. Remediation of Line Edge Roughness in Chemical Nanopatterns by the Directed Assembly of Overlying Block Copolymer Films. *Macromolecules* **2010**, *43*, 2334−2342.

51. Patrone, P. N.; Gallatin, G. M. Modeling Line Edge Roughness in Templated, Lamellar Block Copolymer Systems. *Macromolecules* **2012**, *45*, 9507−9516.

52. Suh, H. S.; Chen, X.; Rincon-Delgadillo, P. A.; Jiang, Z.; Strzalka, J.; Wang, J.; Chen, W.; Gronheid, R.; de Pablo, J. J.; Ferrier, N.; Doxastakis, M.; Nealey, P. F. Characterization of the Shape and Line-Edge Roughness of Polymer Gratings with

Grazing Incidence Small-Angle X-Ray Scattering and Atomic Force Microscopy. *J. Appl. Cryst.* **2016**, *49*, 823−834.

53. Witten, T. A.; Leibler, L.; Pincus, P. A. Stress Relaxation in the Lamellar Copolymer Mesophase. *Macromolecules* **1990**, *23*, 824−829.

54. Semenov, A. N. Theory of Block-Copolymer Interfaces in the Strong Segregation Limit. *Macromolecules* **1993**, *26*, 6617−6621.

55. Semenov, A. N. Scattering of Statistical Structure of Polymer/Polymer Interfaces. *Macromolecules* **1994**, *27*, 2732−2735.

56. Srinivas, G.; Swope, W. C.; Pitera, J. W. Interfacial Fluctuations of Block Copolymers: A Coarse-Grain Molecular Dynamics Simulation Study. *J. Phys. Chem. B* **2007**, *111*, 13734−13742.

57. Stein, G. E.; Liddle, J. A.; Aquila, A. L.; Gullikson, E. M. Measuring the Structure of Epitaxially Assembled Block Copolymer Domains with Soft X-ray Diffraction. *Macromolecules* **2010**, *43*, 433−441

58. *International Technology Roadmap for Semiconductors, 2017 Edition*, https://www.dropbox.com/sh/3jfh5fq634b5yqu/AADYT8V2Nj5bX6C5q764kUg4a?dl=0&preview=0_2015+ITRS+2.0+Executive+Report.pdf

59. Bosse, A. W. Phase-Field Simulation of Long-Wavelength Line Edge Roughness in Diblock Copolymer Resists. *Macromol. Theory Simul.* **2010**, *19*, 399−406.

60. Bosse, A. W. Effects of Segregation Strength and an External Field on the Thermal Line Edge and Line Width Roughness Spectra of a Diblock Copolymer Resist. *J. Vac. Sci. Technol. B* **2011**, *29*, 031803.

61. Bosse, A. Modeling the Power Spectrum of Thermal Line Edge Roughness in a Lamellar Diblock Copolymer Mesophase. *J. Vac. Sci. Technol. B* **2011**, *29*, 06F202.

62. Ruiz, R.; Wan, L.; Lopez, R.; Albrecht, T. R. Line Roughness in Lamellae-Forming Block Copolymer Films. *Macromolecules* **2017**, *50*, 1037−1046.

63. Sunday, D. F.; Hammond, M. R.; Wang, C.; Wut, W.; Delongchamp, D. M.; Tjio, M.; Cheng, J. Y.; Pitera, J. W.; Kline, R. J. Determination of the Internal Morphology of Nanostructures Patterned by Direct Self Assembly. *ACS Nano* **2014**, *8*, 8426−8437.

64. Sunday, D. F.; Ren, J.; Liman, C. D.; Williamson, L. D.; Gronheid, R.; Nealey, P. F.; Kline, R. J. Characterizing Patterned Block Copolymer Thin Films with Soft X-Rays. *ACS Appl. Mater. Interfaces* **2017**, *9*, 31325−31334.

65. Hahm, J.; Lopes, W. A.; Jaeger, H. M.; Sibener, S. J. Defect Evolution in Ultrathin Films of Polystyrene-Block-Polymethylmethacrylate Diblock Copolymers Observed by Atomic Force Microscopy. *J. Chem. Phys.* **1998**, *109*, 10111−10114.

66. Tsarkova, L.; Knoll, A.; Magerle, R. Rapid Transitions between Defect Configurations in a Block Copolymer Melt. *Nano Lett.* **2006**, *6*, 1574−1577

67. Tsarkova, L.; Horvat, A.; Krausch, G.; Zvelindovsky, A. V.; Agur Sevink, G. J.; Magerle, R. Defect Evolution in Block Copolymer Thin Films via Temporal Phase Transitions. *Langmuir*, **2006**, *22*, 8089−8095.

68. Yufa, N. A.; Li, J.; Sibener, S. J. In-Situ High-Temperature Studies of Diblock Copolymer Structural Evolution. *Macromolecules* **2009**, *42*, 2667−2671.

69. Hansma, P. K.; Schitter, G.; Fantner, G. E.; Prater, C. High-Speed Atomic Force Microscopy. *Science* **2006**, *314*, 601−602.

70. Riesch, C.; Radons, G.; Magerle, R. Aging of Orientation Fluctuations in Stripe Phases. *Phys. Rev. E* **2014**, *90*, 052101.

71. Riesch, C.; Radons, G.; Magerle, R. Scaling Properties of Ageing Orientation Fluctuations in Stripe Phases. *Interface Focus* **2017**, *7*, 20160146.

72. Shull, K. R.; Mayes, A. M.; Russell, T. P. Segment Distributions in Lamellar Diblock Copolymers. *Macromolecules* **1993**, *26*, 3929−3936.

73. Bosse, A. W.; Lin, E. K.; Jones, R. L.; Karim, A. Interfacial Fluctuations in an Ideal Block Copolymer Resist. *Soft Matter* **2009**, *5*, 4266−4271.

74. Geisinger, T.; Müller, M.; Binder, K. Symmetric Diblock Copolymers in Thin Films. II. Comparison of Profiles between Self-Consistent Field Calculations and Monte Carlo Simulations. *J. Chem. Phys.* **1999**, *111*, 5251−5258.

75. Mansky, P.; Russell, T. P.; Hawker, C. J.; Mays, J.; Cook, D. C.; Satija, S. K. Interfacial Segregation in Disordered Block Copolymers: Effect of Tunable Surface Potentials. *Phys. Rev. Lett.* **1997**, *79*, 237−240.

76. Keddie, J. L. Size-Dependent Depression of the Glass Transition Temperature in Polymer Films. *Europhys. Lett.* **1994**, *27*, 59−64.

77. Fakhraai, Z.; Forrest, J. A. Probing Slow Dynamics in Supported Thin Polymer Films. *Phys. Rev. Lett.* **2005**, *95*, 025701.

78. Zhang, Y.; Potter, R.; Zhang, W.; Fakhraai, Z. Using Tobacco Mosaic Virus to Probe Enhanced Surface Diffusion of Molecular Glasses. *Soft Matter* **2016**, *44*, 9115−9120.

79. Yeung, C.; Shi, A.-C.; Noolandi, J; Desai, R. C. Anisotropic Fluctuations in Ordered Copolymer Phases. *Macromol. Theory Simul.* **1996**, *5*, 291−298.

80. Hammond, M. R.; Kramer, E. J. Edge Effects on Thermal Disorder in Laterally Confined Diblock Copolymer Cylinder Monolayers. *Macromolecules* **2006**, *39*, 1538−1544.

81. Yokoyama, H. Diffusion of Block Copolymers. *Mater. Sci. Eng. R* **2006**, *53*, 199−248.

82. Barnes, J. A.; Allan, D. W. A Statistical Model of Flicker Noise. *Proc. IEEE* **1966**, *54*, 176−178

83. Dalvi, M. C.; Lodge, T. P. Parallel and Perpendicular Chain Diffusion in a Lamellar Block Copolymer. *Macromolecules* **1993**, *26*, 859−861

84. Lodge, T. P.; Dalvi, M. C. Mechanisms of Chain Diffusion in Lamellar Block Copolymers. *Phys. Rev. Lett.* **1995**, *75*, 657−660.

85. Rittig, F.; Fleischer, G.; Kärger, J.; Papadakis, C. M.; Almdal, K.; Štěpánek, P. Anisotropic Self-Diffusion in a Hexagonally Ordered Asymmetric PEP-PDMS Diblock Copolymer Studied by Pulsed Field Gradient NMR. *Macromolecules* **1999**, *32*, 5872−5877.

86. Cavicchi, K. A.; Lodge, T. P. Anisotropic Self-Diffusion in Block Copolymer Cylinders. *Macromolecules* **2004**, *37*, 6004−6012.

87. Ruiz, R.; Bosworth, J. K.; Black, C. T. Effect of Structural Anisotropy on the Coarsening Kinetics of Diblock Copolymer Striped Patterns. *Phys. Rev. B* **2008**, *77*, 054204.

88. Hamersky, M. W.; Hillmyer, M. A.; Tirrell, M.; Bates, F. S.; Lodge, T. P. Block Copolymer Self-Diffusion in the Gyroid and Cylinder Morphologies. *Macromolecules* **1998**, *31*, 5363−5370.

89. Jones, E.; Oliphant, E.; Peterson, P. *et. al.* SciPy: Open Source Scientific Tools for Python. **2001**, http://www.scipy.org/

90. Welch, P. D. The Use of Fast Fourier Transform for the Estimation of Power Spectra: A Method Based on Time Averaging Over Short, Modified Periodograms. *IEEE Trans. Audio & Electroacoust.* **1967**, *15*, 70−73.

91. Matsui, I. Nanoparticles for Electronic Device Applications: A Brief Review *J. Chem. Eng. Jpn.* **2005**, *38*, 535–546.

92. Stebe, K. J.; Lewandowski, E.; Ghosh, M. Oriented Assembly of Metamaterials *Science* **2009**, *325*, 159–160.

93. Gass, J.; Poddar, P.; Almand, J.; Srinath, S.; Srikanth, H. Superparamagnetic Polymer Nanocomposites with Uniform Fe3O4 Nanoparticle Dispersions *Adv. Funct. Mater.* **2006**, *16*, 71–75.

94. Nie, Z.; Petukhova, A.; Kumacheva, E. Properties and Emerging Applications of Self-Assembled Structures Made from Inorganic Nanoparticles *Nat. Nanotechnol.* **2010**, *5*, 15–25.

95. Stiles, P. L.; Dieringer, J. A.; Shah, N. C.; Van Duyne, R. P. Surface-Enhanced Raman Spectroscopy *Annu. Rev. Anal. Chem.* **2008**, *1*, 601–626.

96. Li, N.; Zhao, P.; Astruc, D. Anisotropic Gold Nanoparticles: Synthesis, Properties, Applications, and Toxicity *Angew. Chem. Int. Ed.* **2014**, *53*, 1756–1789.

97. Vigderman, L.; Khanal, B. P.; Zubarev, E. R. Functional Gold Nanorods: Synthesis, Self-Assembly, and Sensing Applications *Adv. Mater.* **2012**, *24*, 4811–4841.

98. Grande, M.; Bianco, G. V; Vincenti, M. A.; Stomeo, T.; de Ceglia, D.; De Vittorio, M.; Petruzzelli, V.; Scalora, M.; Bruno, G.; D'Orazio, A. Experimental Surface-Enhanced

Raman Scattering Response of Two-Dimensional Finite Arrays of Gold Nanopatches *Appl. Phys. Lett.* **2012**, *101*, 111606.

99. Chirumamilla, M.; Toma, A.; Gopalakrishnan, A.; Das, G.; Zaccaria, R. P.; Krahne, R.; Rondanina, E.; Leoncini, M.; Liberale, C.; De Angelis, F.; Fabrizio, E. D. 3D Nanostar Dimers with a Sub-10-Nm Gap for Single-/Few-Molecule Surface-Enhanced Raman Scattering *Adv. Mater.* **2014**, *26*, 2353–2358.

100. D'Andrea, C.; Fazio, B.; Gucciardi, P. G.; Giordano, M. C.; Martella, C.; Chiappe, D.; Toma, A.; de Mongeot, F.; Tantussi, F.; Vasanthakumar, P.; Fuso, F.; Allegrini, M. SERS Enhancement and Field Confinement in Nanosensors Based on Self-Organized Gold Nanowires Produced by Ion-Beam Sputtering *J. Phys. Chem. C* **2014**, *16*, 8571-8580.

101. Nepal, D.; Onses, M. S.; Park, K.; Jespersen, M.; Thode, C. J.; Nealey, P. F.; Vaia, R. A. Control over Position, Orientation, and Spacing of Arrays of Gold Nanorods Using Chemically Nanopatterned Surfaces and Tailored Particle–Particle–Surface Interactions *ACS Nano* **2012**, *6*, 5693–5701.

102. Adams, S. M.; Campione, S.; Caldwell, J. D.; Bezares, F. J.; Culbertson, J. C.; Capolino, F.; Ragan, R. Non-Lithographic SERS Substrates: Tailoring Surface Chemistry for Au Nanoparticle Cluster Assembly *Small* **2012**, *8*, 2239–2249.

103. Kuemin, C.; Nowack, L.; Bozano, L.; Spencer, N. D.; Wolf, H. Oriented Assembly of Gold Nanorods on the Single-Particle Level *Adv. Funct. Mater.* 2012, *22*, 702–708.

104. Kraus, T.; Malaquin, L.; Schmid, H.; Riess, W.; Spencer, N. D.; Wolf, H. Nanoparticle Printing with Single-Particle Resolution *Nat. Nanotechnol.* **2007**, *2*, 570–576.

105. Liu, Z.; Huang, H.; He, T. Large-Area 2D Gold Nanorod Arrays Assembled on Block Copolymer Templates *Small* **2013**, *9*, 505–510.

106. Zhou, X.; Zhou, Y.; Ku, J. C.; Zhang, C.; Mirkin, C. A. Capillary Force-Driven, Large-Area Alignment of Multi-Segmented Nanowires *ACS Nano* **2014**, *8*, 1511–1516.

107. Xiao, J.; Li, Z.; Ye, X.; Ma, Y.; Qi, L. Self-Assembly of Gold Nanorods into Vertically Aligned, Rectangular Microplates with a Supercrystalline Structure *Nanoscale* **2014**, *6*, 996–1004.

108. Gordon, M. J.; Peyrade, D. Separation of Colloidal Nanoparticles Using Capillary Immersion Forces *Appl. Phys. Lett.* **2006**, *89*, 053112.

109. Thai, T.; Zheng, Y.; Ng, S. H.; Mudie, S.; Altissimo, M.; Bach, U. Self-Assembly of Vertically Aligned Gold Nanorod Arrays on Patterned Substrates *Angew. Chem. Int. Ed.* **2012**, *51*, 8732–8735.

110. Kawamura, G.; Yang, Y.; Nogami, M. Facile Assembling of Gold Nanorods with Large Aspect Ratio and Their Surface-Enhanced Raman Scattering Properties *Appl. Phys. Lett.* **2007**, *90*, 261908.

111. Fontana, J.; Livenere, J.; Bezares, F. J.; Caldwell, J. D.; Rendell, R.; Ratna, B. R. Large Surface-Enhanced Raman Scattering from Self-Assembled Gold Nanosphere Monolayers *Appl. Phys. Lett.* **2013**, *102*, 201606.

112. Alvarez-Puebla, R. A.; Agarwal, A.; Manna, P.; Khanal, B. P.; Aldeanueva-Potel, P.; Carbo-Argibay, E.; Pazos-Perez, N.; Vigderman, L.; Zubarev, E. R.; Kotov, N. A.; Liz-Marzan, L. M. Gold Nanorods 3D-Supercrystals as Surface Enhanced Raman Scattering Spectroscopy Substrates for the Rapid Detection of Scrambled Prions *Proc. Natl. Acad. Sci.* **2011**, *108*, 8157–8161.

113. Huang, X.; Neretina, S.; El-Sayed, M. A. Gold Nanorods: From Synthesis and Properties to Biological and Biomedial Applications *Adv. Mater.* **2009**, *21*, 4880–4910.

114. Liu, M.; Guyot-Sionnest, P. Optical Properties of Rodlike and Bipyramidal Gold Nanoparticles from Three-Dimensional Computations *Phys. Rev. B* **2007**, *76*, 235410–235428.

115. Zhu, Y.; Kuang, H.; Xu, L.; Ma, W.; Peng, C.; Hua, Y.; Wang, L.; Xu, C. Gold Nanorod Assembly Based Approach to Toxin Detection by SERS *J. Mater. Chem.* **2012**, *22*, 2387–2391.

116. Zhong, L.; Zhou, X.; Bao, S.; Shi, Y.; Wang, Y.; Hong, S.; Huang, Y.; Wang, X.; Xie, Z.; Zhang, Q. Rational Design and SERS Properties of Side-by-Side, End-to-End and End-to-Side Assemblies of Au Nanorods *J. Mater. Chem.* **2011**, *21*, 14448–14455.

117. Peng, B.; Li, G.; Li, D.; Dodson, S.; Zhang, Q.; Zhang, J.; Lee, Y. H.; Demir, H. V.; Yi Ling, X.; Xiong, Q. Vertically Aligned Gold Nanorod Monolayer on Arbitrary Substrates: Self-Assembly and Femtomolar Detection of Food Contaminants *ACS Nano* **2013**, *7*, 5993–6000.

118. Kao, J.; Thorkelsson, K.; Bai, P.; Rancatore, B. J.; Xu, T. Toward Functional Nanocomposites: Taking the Best of Nanoparticles, Polymers, and Small Molecules *Chem. Soc. Rev.* **2013**, *42*, 2654–2678.

119. Deshmukh, R. D.; Liu, Y.; Composto, R. J. Two-Dimensional Confinement of Nanorods in Block Copolymer Domains *Nano Lett.* **2007**, *7*, 3662–3668.

120. Thorkelsson, K.; Nelson, J. H.; Alivisatos, A. P.; Xu, T. End-to-End Alignment of Nanorods in Thin Films *Nano Lett.* **2013**, *13*, 4908–4913.

121. Son, J. G.; Bae, W. K.; Kang, H.; Nealey, P. F.; Char, K. Placement Control of Nanomaterial Arrays on the Surface-Reconstructed Block Copolymer Thin Films *ACS Nano* **2009**, *3*, 3927–3934.

122. Chan, D. Y. C.; jr., J. D. H.; White, L. R. The Interaction of Colloidal Particles Collected at Fluid Interfaces *J. Colloid Interface Sci.* **1981**, *79*, 410–418.

123. Kralchevsky, P. A.; Paunov, V. N.; Ivanov, I. B.; Nagayama, K. Capillary Meniscus Interaction between Colloidal Particles Attached to a Liquid—fluid Interface *J. Colloid Interface Sci.* **1992**, *151*, 79–94.

124. Kralchevsky, P. A.; Paunov, V. N.; Denkov, N. D.; Ivanov, I. B.; Nagayama, K. Energetical and Force Approaches to the Capillary Interactions between Particles Attached to a Liquid-Fluid Interface *J. Colloid Interface Sci.* **1993**, *155*, 420–437.

125. Kralchevsky, P. A.; Nagayama, K. Capillary Forces between Colloidal Particles *Langmuir* **1994**, *10*, 23–36.

126. Xu, Z.-C.; Shen, C.-M.; Xiao, C.-W.; Yang, T.-Z.; Chen, S.-T.; Li, H.-L.; Gao, H.-J. Fabrication of Gold Nanorod Self-Assemblies from Rod and Sphere Mixtures via Shape Self-Selective Behavior *Chem. Phys. Lett.* **2006**, *432*, 222–225.

127. Mathur, A.; Brown, A.-D.; Erlebacher, J. Self-Ordering of Colloidal Particles in Shallow Nanoscale Surface Corrugations *Langmuir* **2006**, *22*, 582–589.

128. Ye, X.; Jin, L.; Caglayan, H.; Chen, J.; Xing, G.; Zheng, C.; Doan-Nguyen, V.; Kang, Y.; Engheta, N.; Kagan, C. R.; et al. Improved Size-Tunable Synthesis of Monodisperse Gold Nanorods through the Use of Aromatic Additives *ACS Nano* **2012**, *6*, 2804–2817.

129. Meena, S. K.; Sulpizi, M. Understanding the Microscopic Origin of Gold Nanoparticle Anisotropic Growth from Molecular Dynamics Simulations *Langmuir* **2013**, *29*, 14954–14961.

130. Cui, Y.; Björk, M. T.; Liddle, J. A.; Sönnichsen, C.; Boussert, B.; Alivisatos, A. P. Integration of Colloidal Nanocrystals into Lithographically Patterned Devices *Nano Lett.* **2004**, *4*, 1093–1098.

131. Wei, H.; Xu, H. Hot Spots in Different Metal Nanostructures for Plasmon-Enhanced Raman Spectroscopy *Nanoscale* **2013**, *5*, 10794–10805.

132. Caldwell, J. D.; Glembocki, O.; Bezares, F. J.; Bassim, N. D.; Rendell, R. W.; Feygelson, M.; Ukaegbu, M.; Kasica, R.; Shirey, L.; Hosten, C. Plasmonic Nanopillar Arrays for Large-Area, High-Enhancement Surface-Enhanced Raman Scattering Sensors *ACS Nano* **2011**, *5*, 4046–4055.

133. Papanu, J. S.; Soane, D. S.; Bell, A. T.; Hess, D. W. Transport Models for Swelling and Dissolution of Thin Polymer Films. *J. Appl. Polym. Sci.* **1989**, *38*, 859-885.

134. Soppimath, K. S.; Aminabhavi, T. M.; Kulkarni, A. R.; Rudzinski, W. E. Biodegradable Polymeric Nanoparticles as Drug Delivery Devices. *J. Control. Release* **2001**, *70*, 1−20.

135. Lalia, B. S.; Kochkodan, V.; Hashaikeh, R.; Hilal, N. A Review on Membrane Fabrication: Structure, Properties and Performance Relationship. *Desalination* **2013**, *326*, 77−95.

136. Flory, P. J.; Rehner, J. Statistical Mechanics of Cross-Linked Polymer Networks II. Swelling. *J. Chem. Phys.* **1943**, *11*, 521−526.

137. Flory, P. J. Statistical Mechanics of Swelling of Network Structures. *J. Chem. Phys.* **1950**, *18*, 108−111.

138. Bruck, S. D. Extension of the Flory-Rehner Theory of Swelling to an Anisotropic System. *J. Polym. Sci.* **1961**, *55*, S29−S31.

139. Shiomi, T.; Kuroki, K.; Kobayashi, A.; Nikaido, H.; Yokoyama, M.; Tezuka, Y.; Imai, K. Dependence of Swelling Degree on Solvent Composition of Two-Component Copolymer Networks in Mixed Solvents. *Polymer* **1995**, *36*, 2443−2449.

140. Toomey, R.; Daniel, F.; Rühe, J. Swelling Behavior of Thin, Surface-Attached Polymer Networks. *Macromolecules* **2004**, *37*, 882−887.

141. Bates, F. S.; Fredrickson, G. H. Block Copolymer Thermodynamics: Theory and Experiment. *Annu. Rev. Phys. Chem.* **1990**, *41*, 525−557.

142. Mansky, P.; Chaikin, P.; Thomas, E. L. Monolayer Films of Diblock Copolymer Microdomains for Nanolithographic Applications. *J. Mater. Sci.* **1995**, *30*, 1987−1992.

143. Sinturel, C.; Vayer, M.; Morris, M.; Hillmyer, M. A. Solvent Vapor Annealing of Block Polymer Thin Films. *Macromolecules*, **2013**, *46*, 5399-5415.

144. Park, W. I.; Kim, J. M.; Jeong, J. W.; Jung, Y. S. Deep-Nanoscale Pattern Engineering by Immersion-Induced Self-Assembly. *ACS Nano* **2014**, *8*, 10009-10018.

145. Modi, A.; Bhaway, S. M.; Vogt, B. D.; Douglas, J. F.; Al-Enizi, A.; Elzatahry, A.; Sharma, A.; Karim, A. Direct Immersion Annealing of Thin Block Copolymer Films. *ACS Appl. Mater. Interfaces* **2015**, *7*, 21638-21645.

146. Lodge, T. P.; Pudil, B.; Hanley, K. J. The Full Phase Behavior for Block Copolymers in Solvents of Varying Selectivity. *Macromolecules* **2002**, *35*, 4707−4717.

147. Hayward, R. C.; Chmelka, B. F.; Kramer, E. J. Template Cross-Linking Effects on Morphologies of Swellable Block Copolymer and Mesostructured Silica Thin Films. *Macromolecules* **2005**, *38*, 7768−7783.

148. Alfrey, T.; Gurnee, E. F.; Lloyd, W. G. Diffusion in Glassy Polymers. *J. Polym. Sci., Part C* **1966**, *12*, 249−261.

149. Thomas, N. L.; Windle, A. H. A Deformation Model for Case II Diffusion. *Polymer* **1979**, *21*, 613−619.

150. Thomas, N. L.; Windle, A. H. A Theory of Case II Diffusion. *Polymer* **1982**, *23*, 529−542.

151. Hori, K.; Matsuno, H.; Tanaka, K. Sorption Kinetics of Methanol in Thin Poly(Methyl Methacrylate) Films Studied by Optical Reflectivity. *Soft Matter*, **2011**, *7*, 10319-10326.

152. Ogieglo, W.; Wormeester, H.; Wessling, M.; Benes, N. E. Probing the Surface Swelling in Ultra-Thin Supported Polystyrene Films During Case II Diffusion of *n*-Hexane. *Macromol. Chem. Phys.* **2013**, *214*, 2480−2488.

153. Peppas, N. A.; Urdahl, K. G. Anomalous Penetrant Transport in Glassy Polymers VII. Overshoots in Cyclohexane Uptake in Crosslinked Polystyrene. *Polym. Bull.* **1986**, *16*, 201−207.

154. Urdahl, K. G.; Peppas, N. A. Anomalous Penetrant Transport in Glassy Polymers V. Cyclohexane Transport in Polystyrene. *J. Appl. Polym. Sci.* **1987**, *33*, 2669−2687.

155. Kim, D.; Caruthers, J. M.; Peppas, N. A. Penetrant Transport in Cross-Linked Polystyrene. *Macromolecules* **1993**, *26*, 1841−1847.

156. Paredes, J. I.; Villar-Rodil, S.; Tamargo-Martínez, K.; Martínez-Alonso, A.; Tascón Real-Time Monitoring of Polymer Swelling on the Nanometer Scale by Atomic Force Microscopy. *Langmuir* **2006**, *22*, 4728−4733.

157. Anastasiadis, S. H.; Russell, T. P.; Satija, S. K.; Majkrzak, C. F. Neutron Reflectivity Studies of the Surface-Induced Ordering of Diblock Copolymer Films. *Phys. Rev. Lett.* **1989**, *62*, 1852−1855.

158. Russell, T. P.; Coulon, G.; Deline, V. R.; Miller, D. C. Characteristics of the Surface-Induced Orientation for Symmetric Diblock PS/PMMA Copolymers. *Macromolecules* **1989**, *22,* 4600−4606.

159. Coulon, G.; Russell, T. P.; Deline, V. R.; Green P. F. Surface-Induced Orientation of Symmetric, Diblock Copolymers: A Secondary Ion Mass-Spectrometry Study. *Macromolecules* **1989**, *22*, 2581−2589.

160. Turner, M. S. Equilibrium Properties of a Diblock Copolymer Lamellar Phase Confined between Flat Plates. *Phys. Rev. Lett.* **1992**, *69*, 1788−1791.

161. Coulon, G.; Collin, B.; Ausserré, D.; Chatenay, D.; Russell, T. P. Islands and Holes on the Free Surface of Thin Diblock Copolymer Films. I. Characteristics of Formation and Growth. *J. Phys.* **1990**, *51*, 2801−2811.

162. Cleveland, J. P.; Anczykowski, B.; Schmid, A. E.; Elings, V. B. Energy Dissipation in Tapping-Mode Atomic Force Microscopy. *Appl. Phys. Lett.* **1998**, *72*, 2613−2615.

163. Knoll, A.; Magerle, R.; Krausch, G. Tapping Mode Atomic Force Microscopy on Polymers: Where Is the True Sample Surface? *Macromolecules* **2001**, *34*, 4159-4165.

164. Carvalho, B. L.; Thomas, E. L. Morphology of Steps in Terraced Block Copolymer Films. *Phys. Rev. Lett.* **1994**, *73*, 3321−3324.

165. Liu, Y.; Rafailovich, M. H.; Sokolov, J.; Schwarz, S. A.; Bahal, S. Effects of Surface Tension on the Dislocation Structures of Diblock Copolymers. *Macromolecules* **1996**, *29*, 899−906.

166. Turner, M. S.; Maaloum, M.; Ausserré, D.; Joanny, J.-F.; Kunz, M. Edge Dislocations in Copolymer Lamellar Films. *J. Phys. II* **1994**, *4*, 689−702.

167. Stasiak, P.; McGraw, J. D.; Dalnoki-Veress, K.; Matsen, M. W. Step Edges in Thin Films of Lamellar-Forming Diblock Copolymer. *Macromolecules* **2012**, *45*, 9531−9538.

168. Schuld, N.; Wolf, B. A. Polymer-Solvent Interaction Parameters. In *Polymer Handbook* 4th ed.; Brandrup, J; Immergut, E. H.; Grulke, E. A., Eds.; John Wiley & Sons: New York, 1999; VII/247−VII/264.

169. Candau, S.; Bastide, J.; Dalsanti, M. Structural, Elastic, and Dynamic Properties of Swollen Polymer Networks. *Adv. Polym. Sci.* **1982**, *44*, 27−71.

125

170. Briscoe, B. J.; Fiori, L.; Pelillo, E. Nano-Indentation of Polymeric Surfaces. *J. Phys. D: Appl. Phys.* **1998**, *31*, 2395−2405.

171. Halperin, A.; Tirrell, M.; Lodge, T. P. Tethered Chains in Polymer Microstructures. *Adv. Polym. Sci.* **1992**, *100*, 31−71.

172. Meier, W. Polymer Networks with Lamellar Structure. *Macromolecules* **1998**, *31*, 2212−2217.

Appendix

Raw Data Referenced for Figures

This appendix includes images of the raw data files used for the figures throughout this report. These files include image data acquired with the Asylum MFP-3D AFM, Asylum Cypher AFM, and Horiba LabRam Evolution confocal Raman microscope. Each appendix figure has received minimal image processing and includes multiple images from a set of related data. The figure captions include a reference to the associated thesis figure(s) alongside the corresponding file names to facilitate data retrieval.

Figure A.2.1
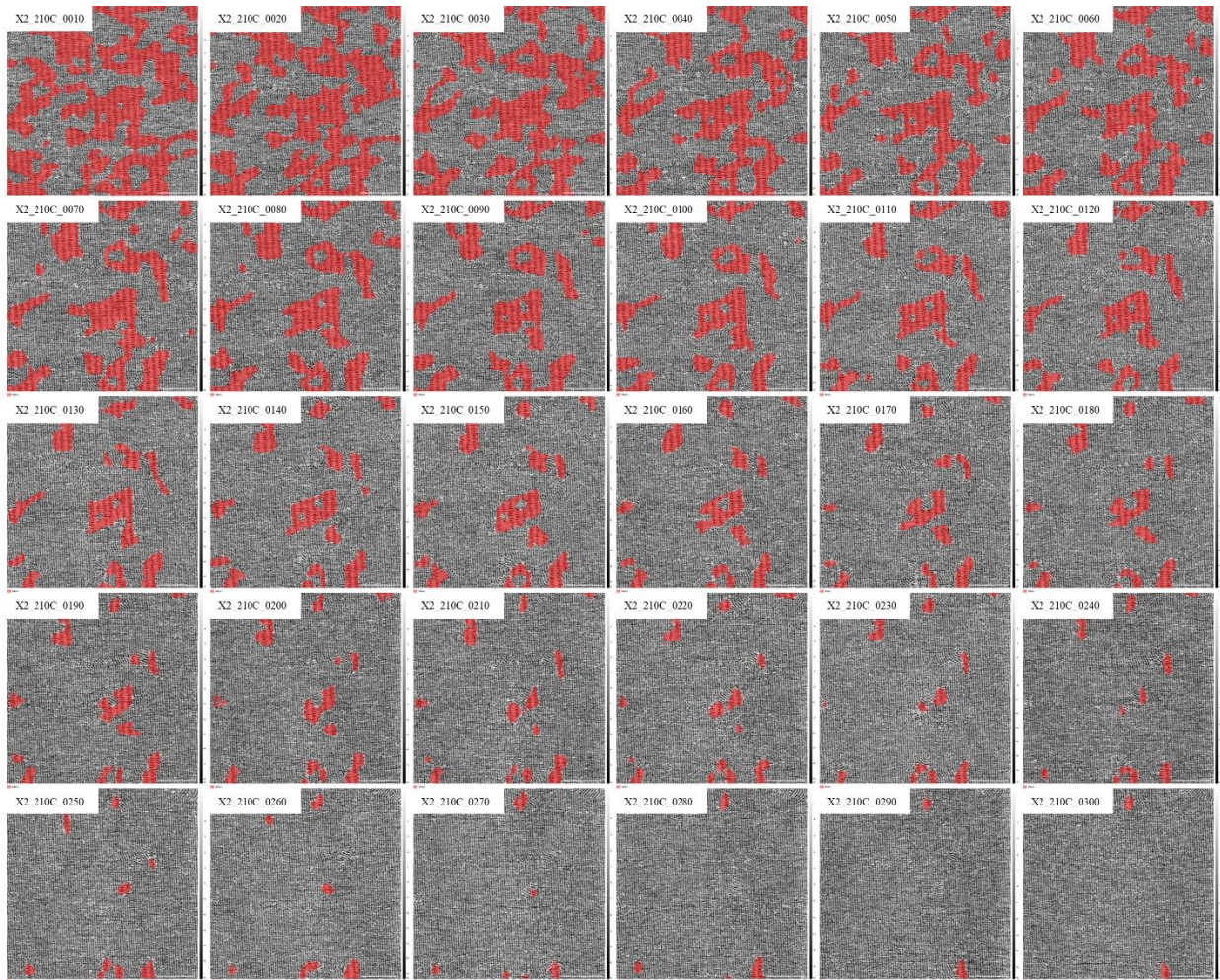
Thermal annealing at 210 °C. Asylum Cypher AFM images of thermal annealing at 210 °C with the stitched morphology masked in red used to create **Figure 2.4**.

Directory: 160509

Filename: X2_210C_0010 – X2_210C_0300

Figure A.2.2
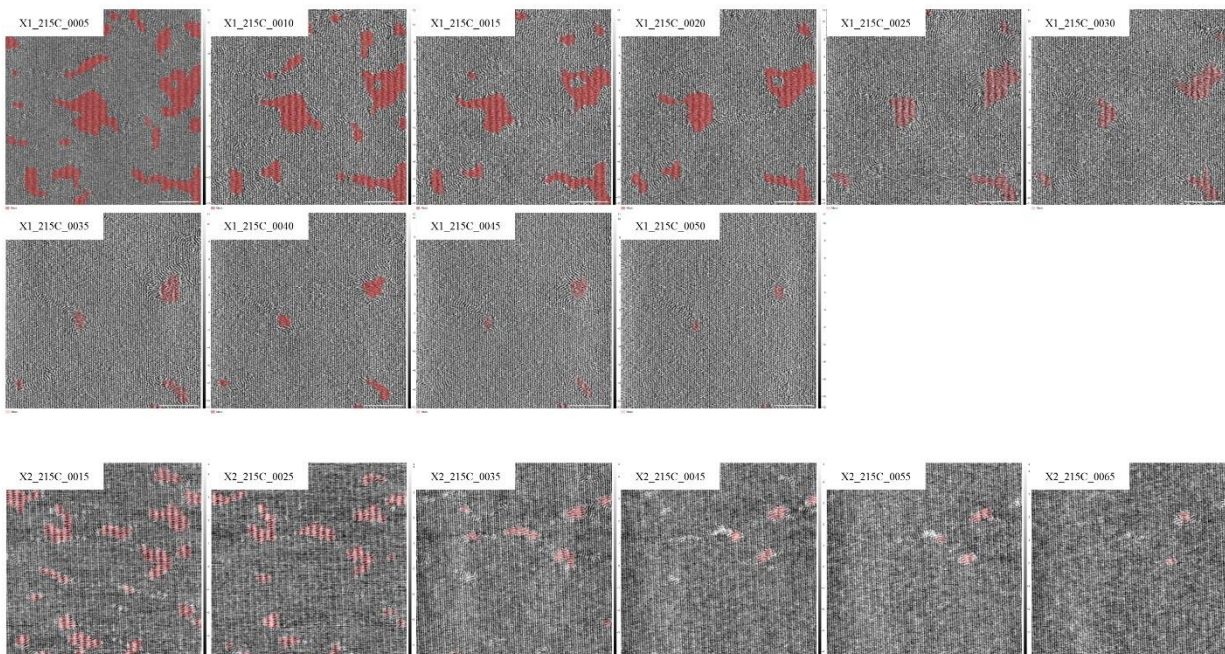
Thermal annealing at 215 °C. Asylum Cypher AFM images of thermal annealing at 215 °C with the stitched morphology masked in red used to create **Figure 2.4**.

Directory: 160615 and 160617

Filename: X1_215C_0005 – X1_215C_0050 and X2_215C_0015 – X2_215C_0065

Figure A.2.3
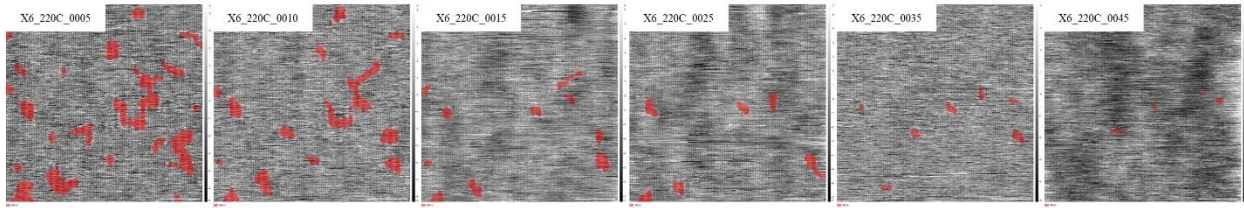
Thermal annealing at 220 °C. Asylum Cypher AFM images of thermal annealing at 220 °C with the stitched morphology masked in red used to create **Figure 2.4**.

Directory: 160623

Filename: X2_220C_0005 – X2_210C_0045

Figure A.2.4
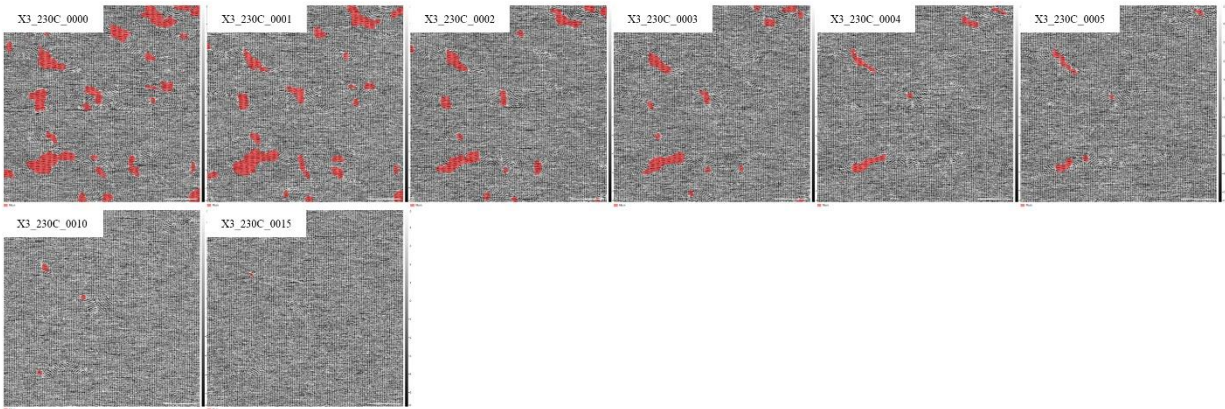
Thermal annealing at 230 °**C.** Asylum Cypher AFM images of thermal annealing at 230 °C with the stitched morphology masked in red used to create **Figure 2.4**.

Directory: 160509

Filename: X3_230C_0000 – X3_230C_0015

Figure A.2.5
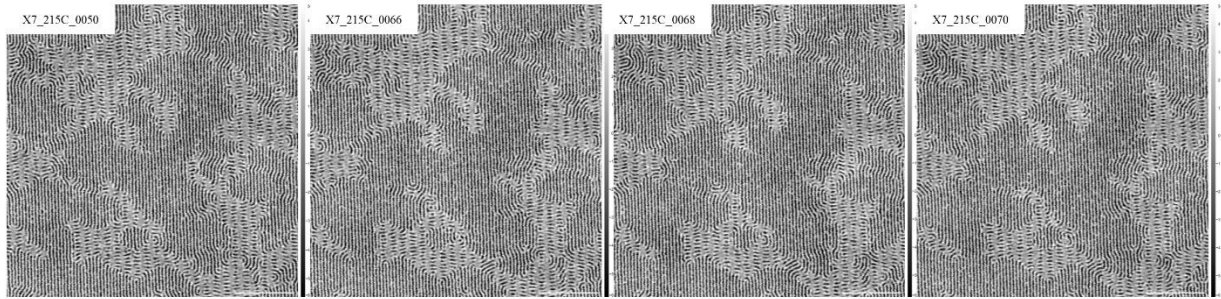
Defect evolution at 215 °C. Asylum Cypher AFM images of thermal annealing on a chemical pattern at 215 °C tracking defect evolution, as used for **Figure 2.5**.

Directory: 160601

Filename: X7_215C_0050 – X7_215C_0070

Figure A.2.6
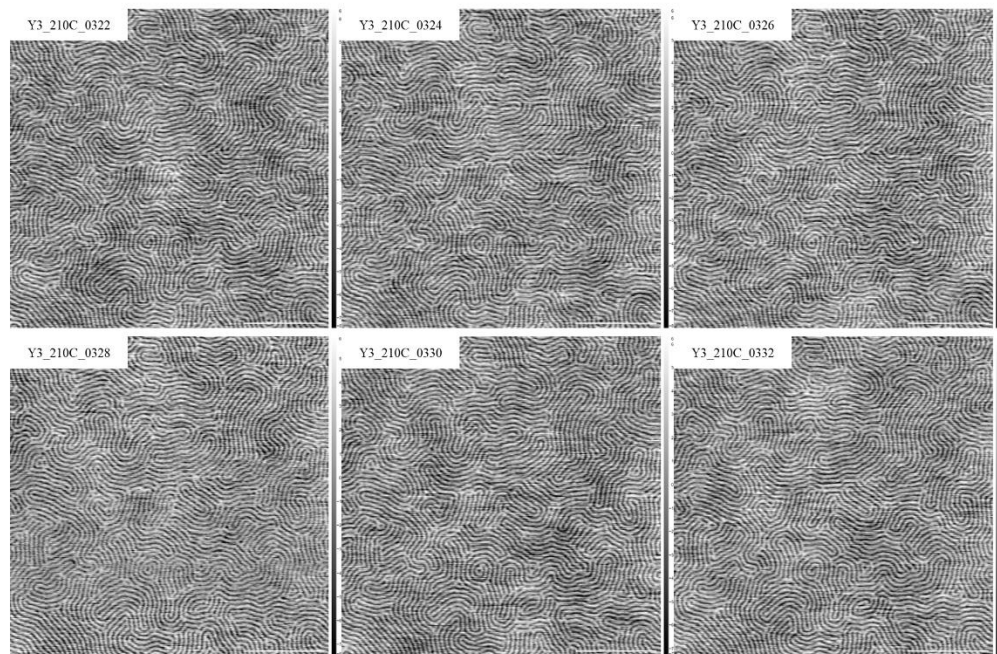
Annealing on an unpatterned substrate. Asylum Cypher AFM images of thermal annealing of a fingerprint pattern at 210 °C showing slow grain growth, as used in **Figure 2.3**.

Directory: 160606

Filename: Y3_210C_0322 – Y3_210C_0332

Figure A.2.7
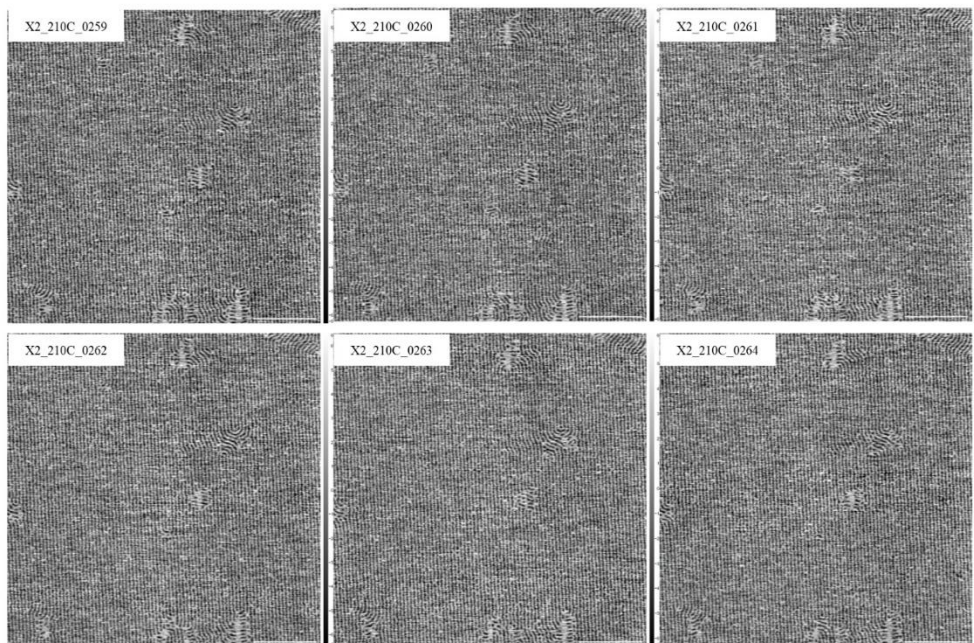
Irreversible annealing on a chemically-patterned substrate. Asylum Cypher AFM images of thermal annealing on a chemical pattern at 210 °C showing irreversible lamellar alignment, as used in **Figure 2.3**.

Directory: 160509

Filename: X2_210C_0259 – X2_210C_0264

Figure A.3.1
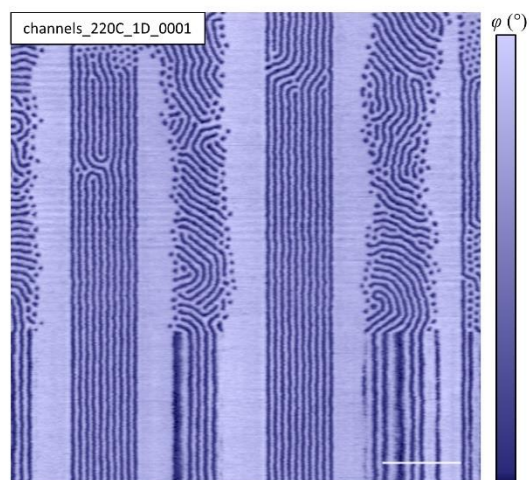
Slow-scan-disabled AFM imaging. Asylum Cypher AFM image during thermal annealing at 220 °C with the slow-scan axis disabled midway through, as used for **Figure 3.2**.

Directory: 170824

Filename: channels_220C_1D_0001

Figure A.3.2
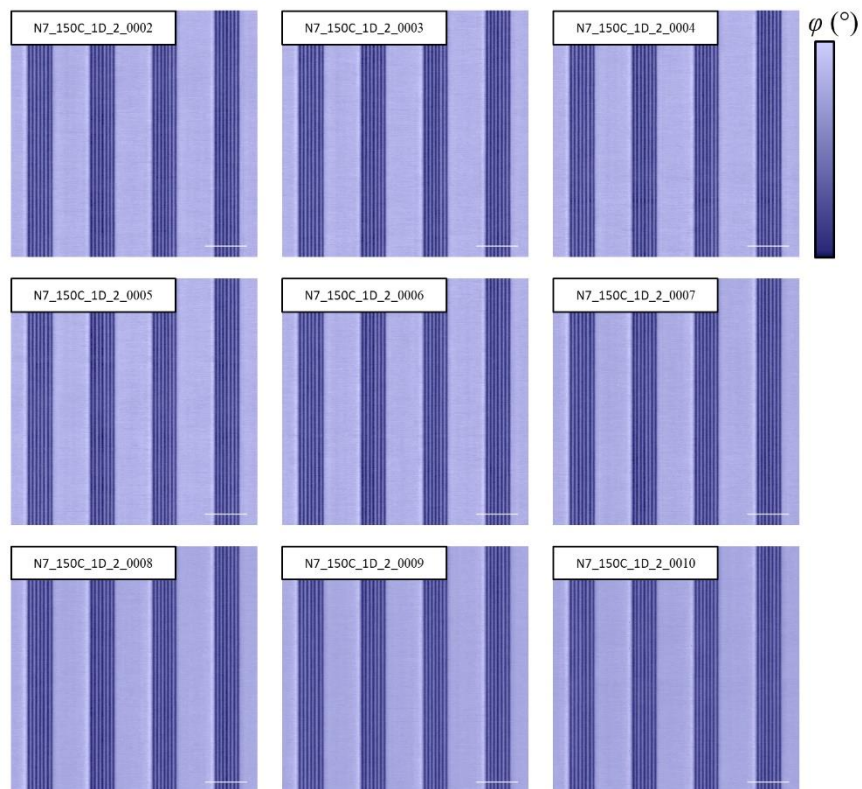
SSD images at 150 °C. Asylum Cypher AFM SSD images during thermal annealing at 150 °C. These data were used for **Figures 3.3**, **3.4**, **3.5**, **3.6**, **3.7**, and **3.8**.

Directory: 170824

Filename: N7_150C_1D_2_0002 – N7_150C_1D_2_0010

Figure A.3.3
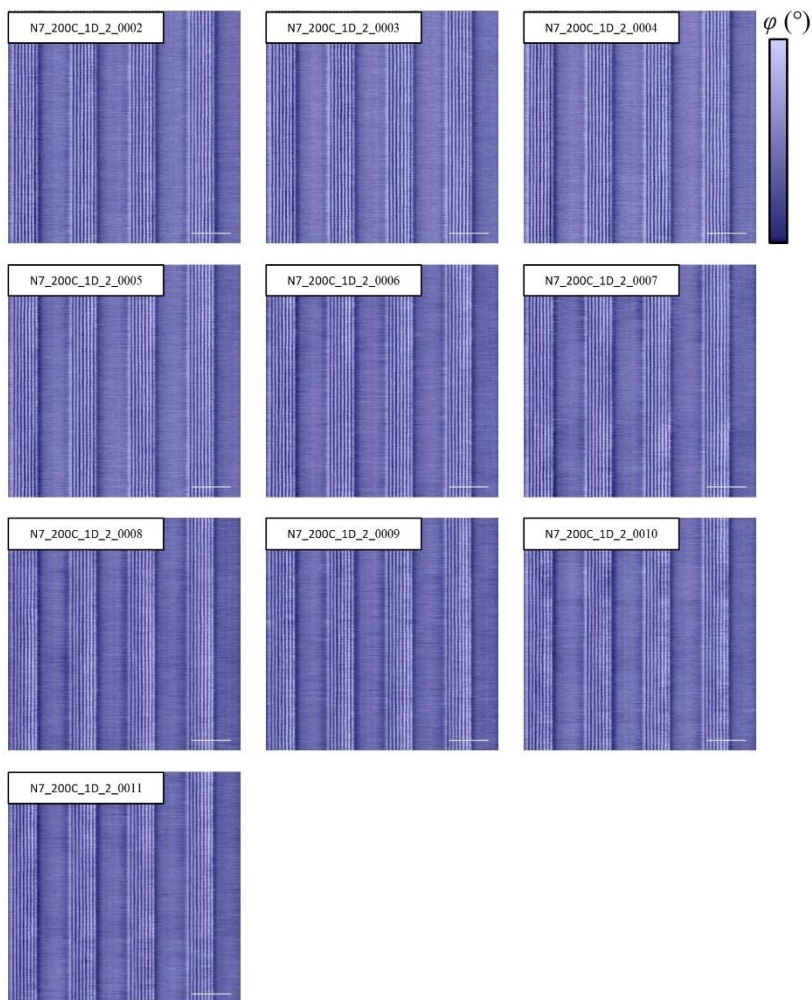
SSD images at 200 °C. Asylum Cypher AFM SSD images during thermal annealing at 200 °C. These data were used for **Figure 3.5**.

Directory: 170824

Filename: N7_200C_1D_2_0002 – N7_200C_1D_2_0011

Figure A.3.4
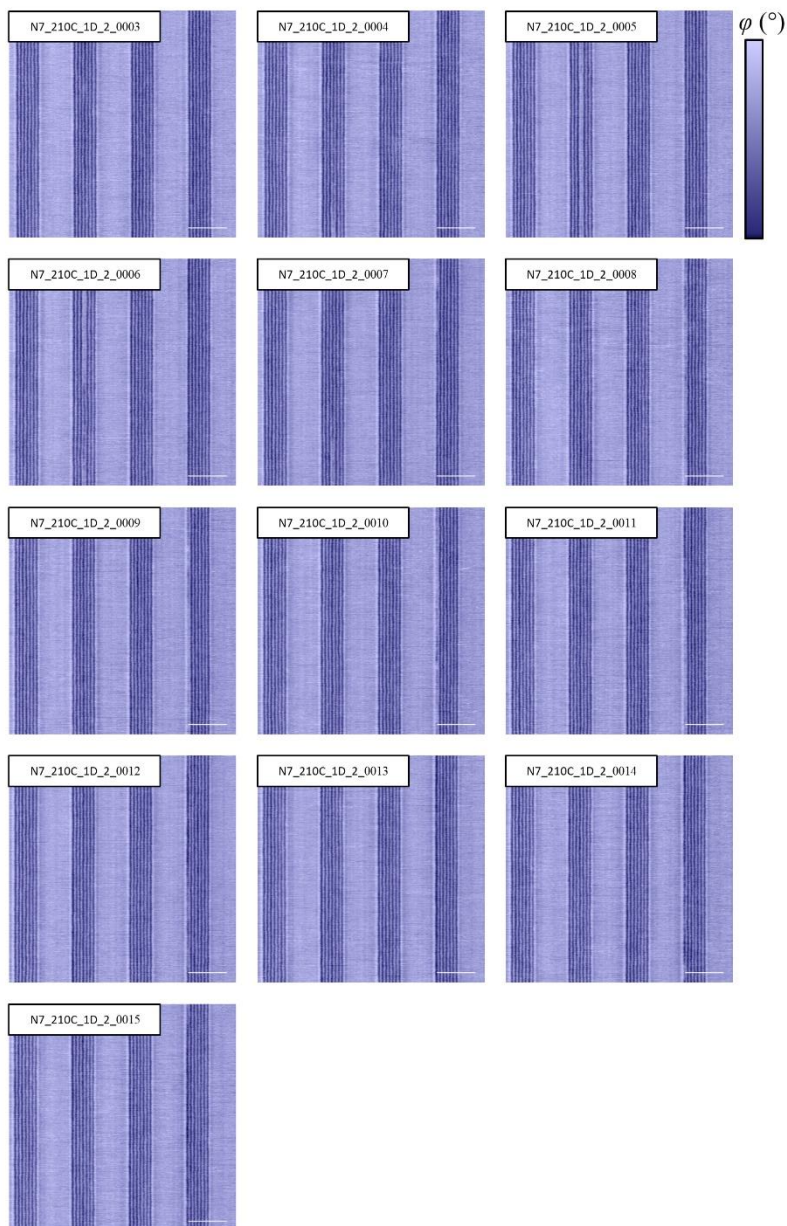
SSD images at 210 °C. Asylum Cypher AFM SSD images during thermal annealing at 210 °C. These data were used for **Figures 3.5**, **3.6**, **3.7**, and **3.8**.

Directory: 170824

Filename: N7_210C_1D_2_0003 – N7_210C_1D_2_0015

Figure A.3.5
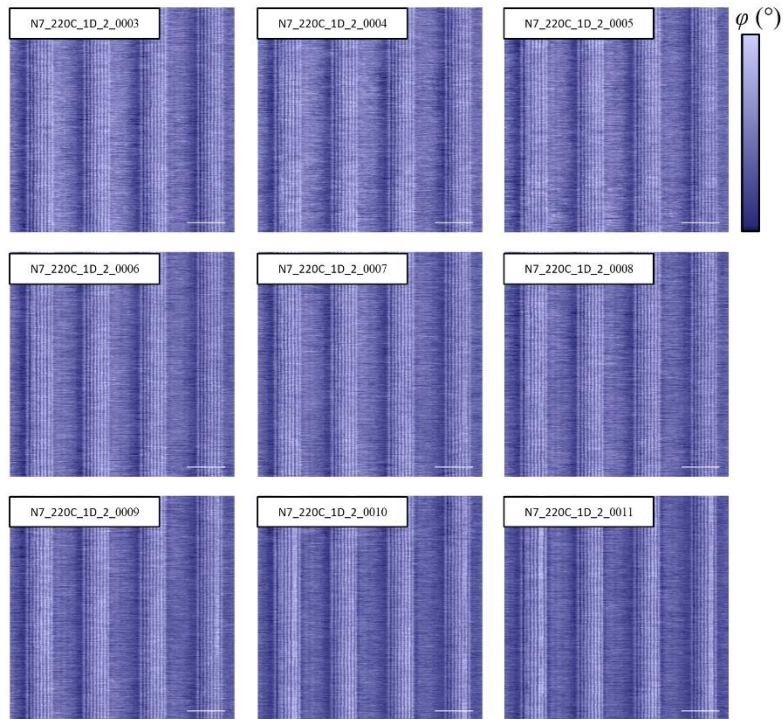
SSD images at 220 °C. Asylum Cypher AFM SSD images during thermal annealing at 220 °C. These data were used for **Figure 3.5**.

Directory: 170824

Filename: N7_220C_1D_2_0003 – N7_220C_1D_2_0011

Figure A.3.6
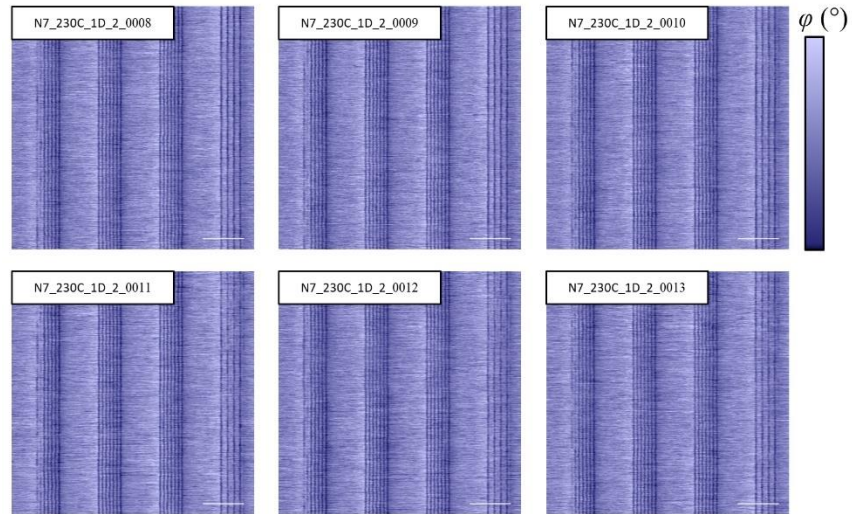
SSD images at 230 °C. Asylum Cypher AFM SSD images during thermal annealing at 230 °C. These data were used for **Figure 3.5**.

Directory: 170824

Filename: N7_230C_1D_2_0008 – N7_230C_1D_2_0013

Figure A.3.7
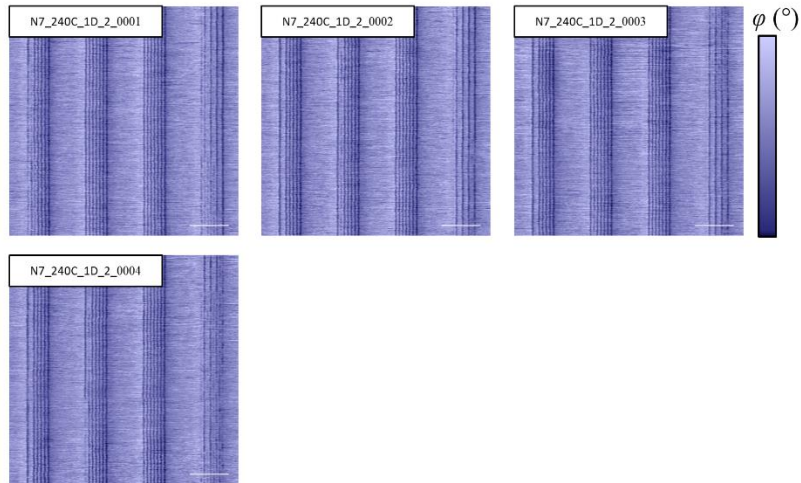
SSD images at 240 °C. Asylum Cypher AFM SSD images during thermal annealing at 240 °C. These data were used for **Figures 3.5**, **3.6**, **3.7**, and **3.8**.

Directory: 170824

Filename: N7_220C_1D_2_0001 – N7_220C_1D_2_0004

Figure A.4.1
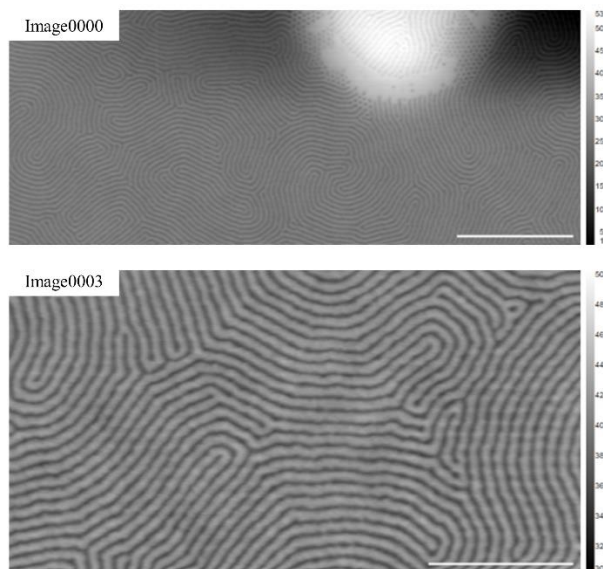
Acetic acid vapor annealing. Asylum MFP-3D AFM images (acquired by Qianqian Tong) of PS-*b*-PMMA fingerprint pattern following acetic acid vapor treatment. These data were used for **Figure 4.1**.

Directory: 130630

**Filename**: Image0000 and Image0003

Figure A.4.2
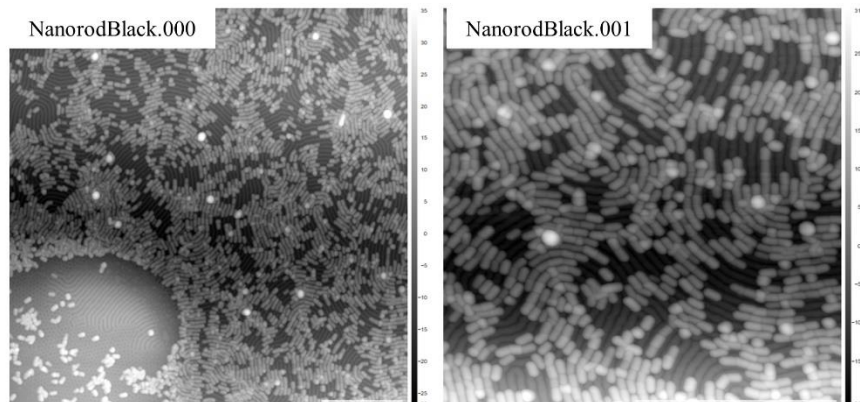
AuNR black on PS-*b*-PMMA. Asylum MFP-3D AFM images (acquired by Qianqian Tong) of AuNRs on a topographically-enhanced PS-*b*-PMMA fingerprint pattern. These data were used for **Figure 4.2** and **Figure 4.3**.

Directory: alignment on flat samples

**Filename**: NanorodBlack.000 and NanorodBlack.001

Figure A.4.3
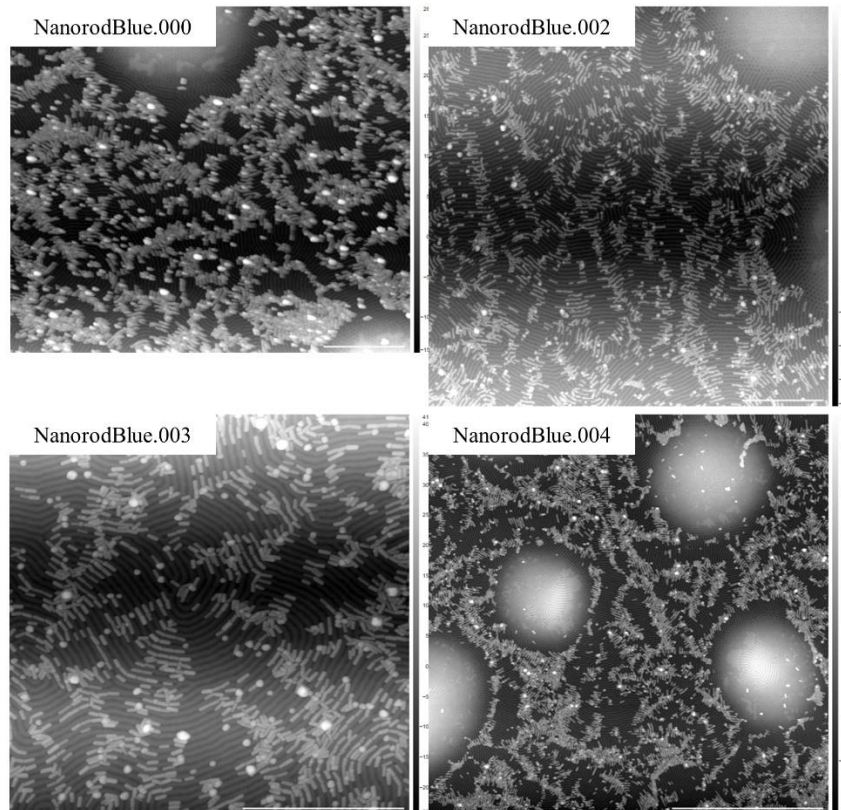
AuNR blue on PS-*b*-PMMA. Asylum MFP-3D AFM images (acquired by Qianqian Tong) of AuNRs on a topographically-enhanced PS-*b*-PMMA fingerprint pattern. These data were used for **Figure 4.2** and **Figure 4.3**.

Directory: alignment on flat samples

Filename: NanorodBlue.000 – NanorodBlue.004

Figure A.4.4
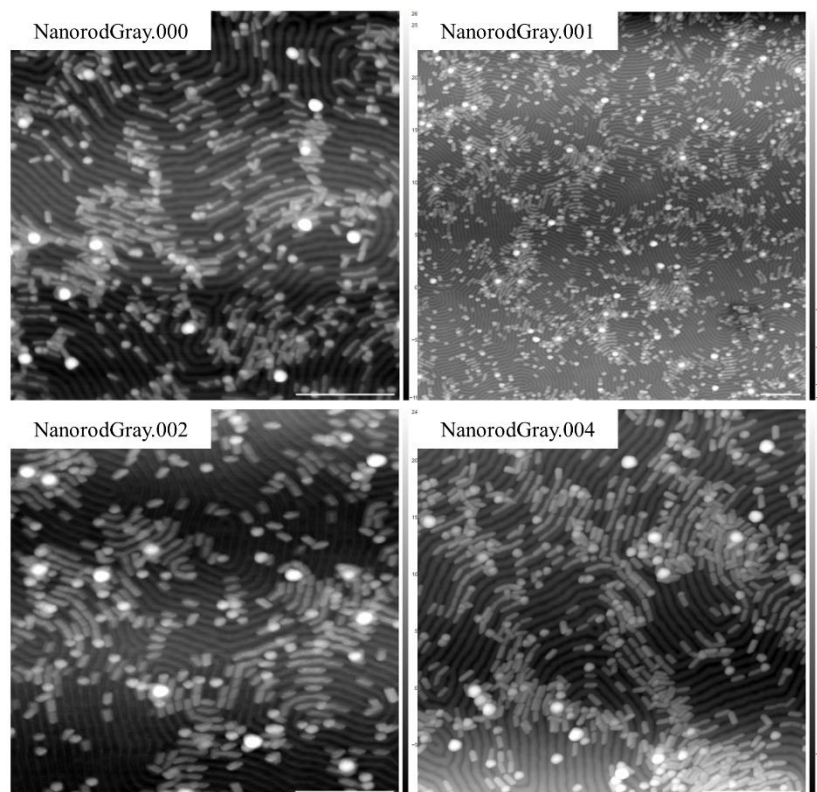
AuNR gray on PS-*b*-PMMA. Asylum MFP-3D AFM images (acquired by Qianqian Tong) of AuNRs on a topographically-enhanced PS-*b*-PMMA fingerprint pattern. These data were used for **Figure 4.2** and **Figure 4.3**.

Directory: alignment on flat samples

Filename: NanorodGray.000 – NanorodGray.004

Figure A.4.5
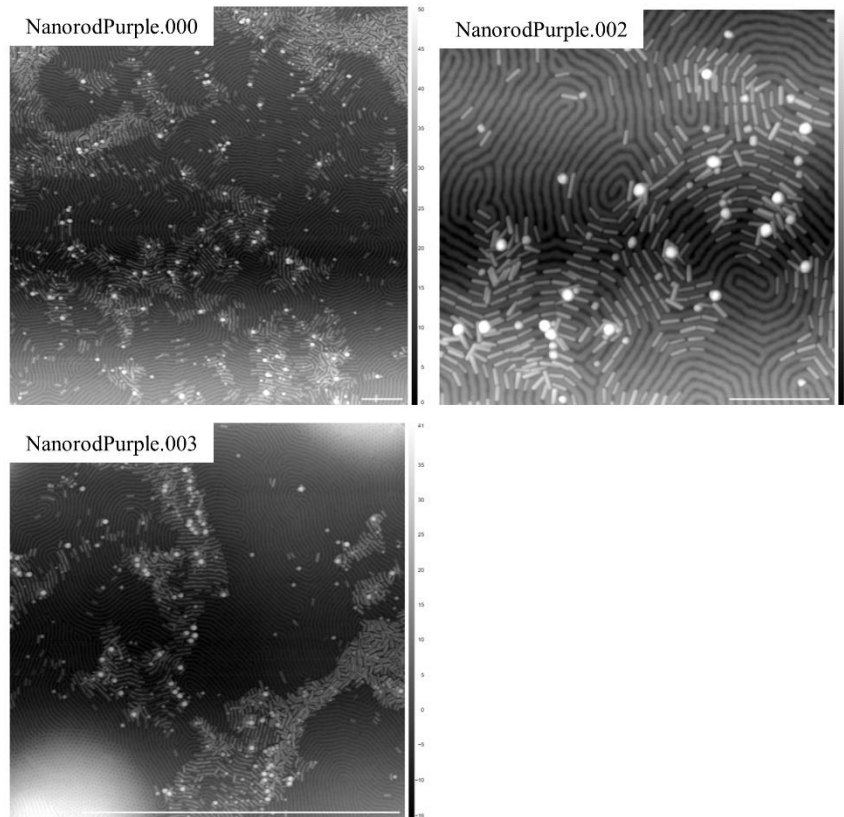
AuNR purple on PS-*b*-PMMA. Asylum MFP-3D AFM images (acquired by Qianqian Tong) of AuNRs on a topographically-enhanced PS-*b*-PMMA fingerprint pattern. These data were used for **Figure 4.2** and **Figure 4.3**.

Directory: alignment on flat samples

Filename: NanorodPurple.000 – NanorodPurple.003

Figure A.4.6
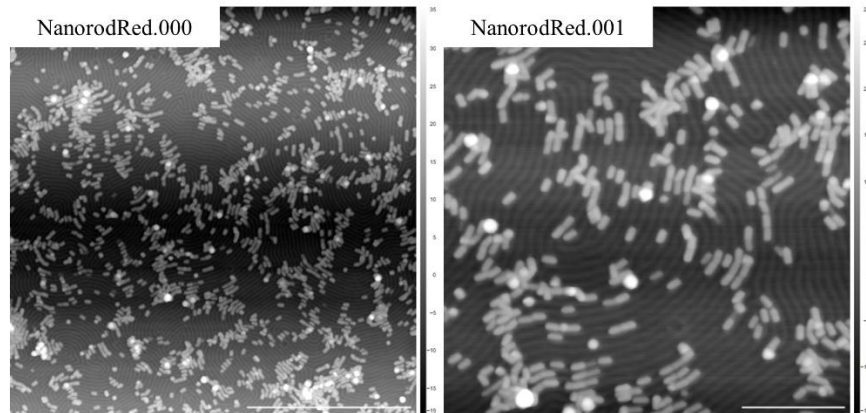
AuNR red on PS-*b*-PMMA. Asylum MFP-3D AFM images (acquired by Qianqian Tong) of AuNRs on a topographically-enhanced PS-*b*-PMMA fingerprint pattern. These data were used for **Figure 4.2** and **Figure 4.3**.

Directory: alignment on flat samples

Filename: NanorodRed.000 and NanorodRed.001

Figure A.4.7
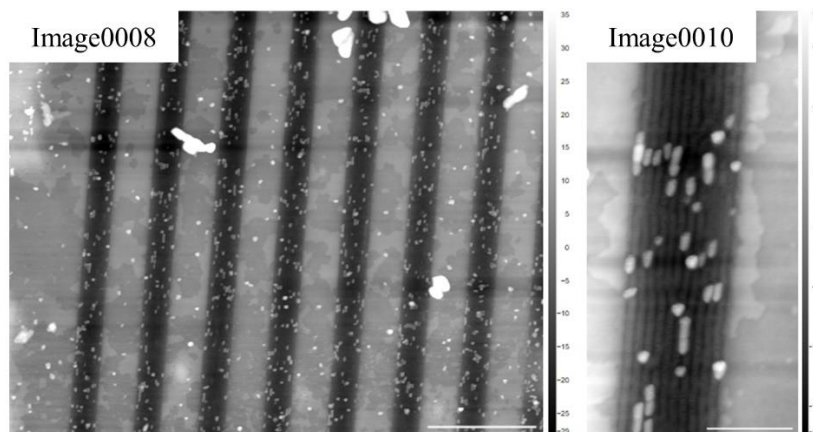
Low coverage AuNR in channels. Asylum MFP-3D AFM images (acquired by Qianqian Tong) of AuNRs on aligned, topographically-enhanced PS-*b*-PMMA in lithographic channels at low coverage. These data were used for **Figure 4.7**.

Directory: 130919

Filename: Image0008 and Image0010

Figure A.4.8
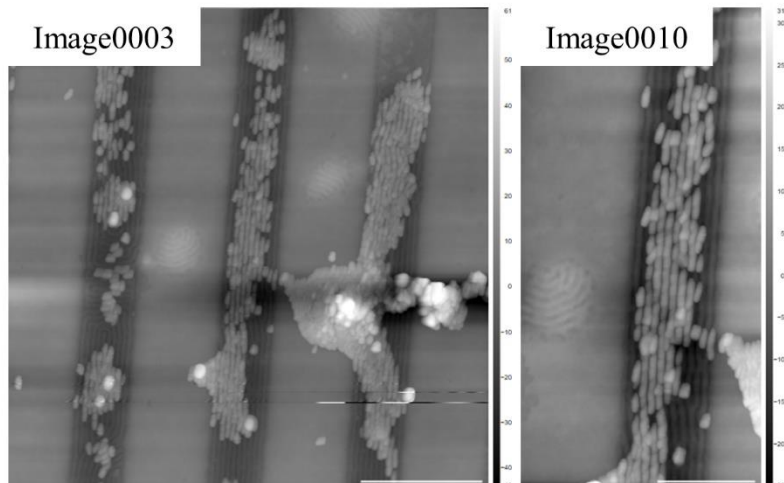
Medium coverage AuNR in channels. Asylum MFP-3D AFM images (acquired by Qianqian Tong) of AuNRs on aligned, topographically-enhanced PS-*b*-PMMA in lithographic channels at medium coverage. These data were used for **Figure 4.7**.

Directory: 131001

Filename: Image0003 and Image0010

Figure A.4.9
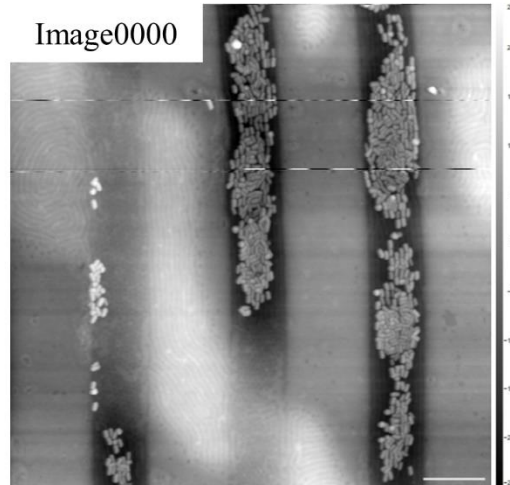
High coverage AuNR in channels. Asylum MFP-3D AFM images (acquired by Qianqian Tong) of AuNRs on aligned, topographically-enhanced PS-*b*-PMMA in lithographic channels at high coverage. These data were used for **Figure 4.7**.

Directory: 131007

Filename: Image0000

Figure A.4.10
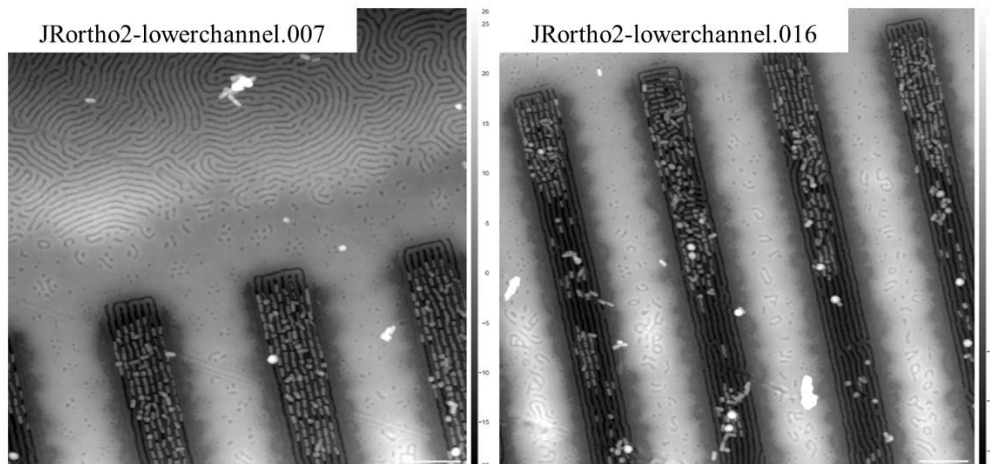
Spatial distribution of AuNR in channels. Asylum MFP-3D AFM images of AuNRs on aligned, topographically-enhanced PS-*b*-PMMA in lithographic channels for correlation with Raman imaging. These data were used for **Figure 4.9**.

**Directory**: 140522

Filename: JRortho2-lowerchannel.007 and JRortho2-lowerchannel.016
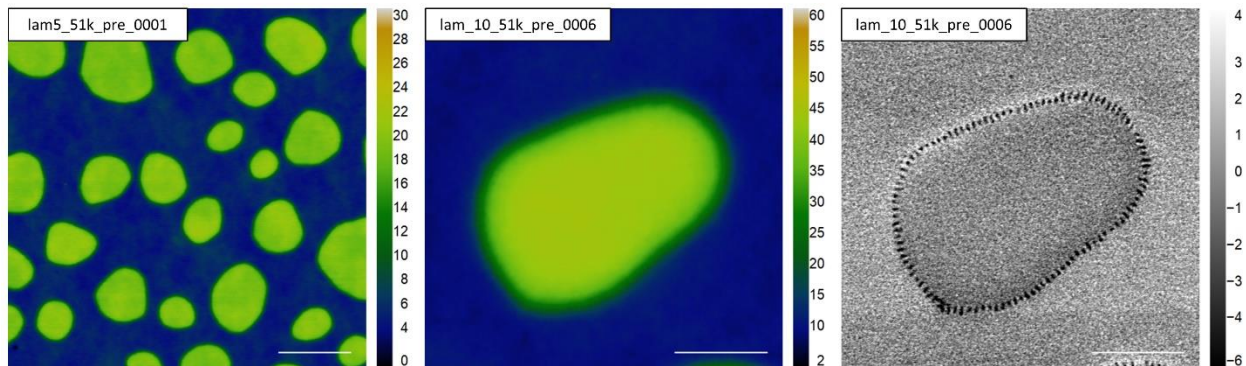
51k PS-*b*-PMMA islands in air. Asylum Cypher AFM images of 51k MW lamellar PS-*b*-PMMA islands in air. These data were used for **Table 5.2**.

Directory: 170905 and 170924

Filename: lam5_51k_pre_0001 and lam_10_51k_pre_0006

Figure A.5.2
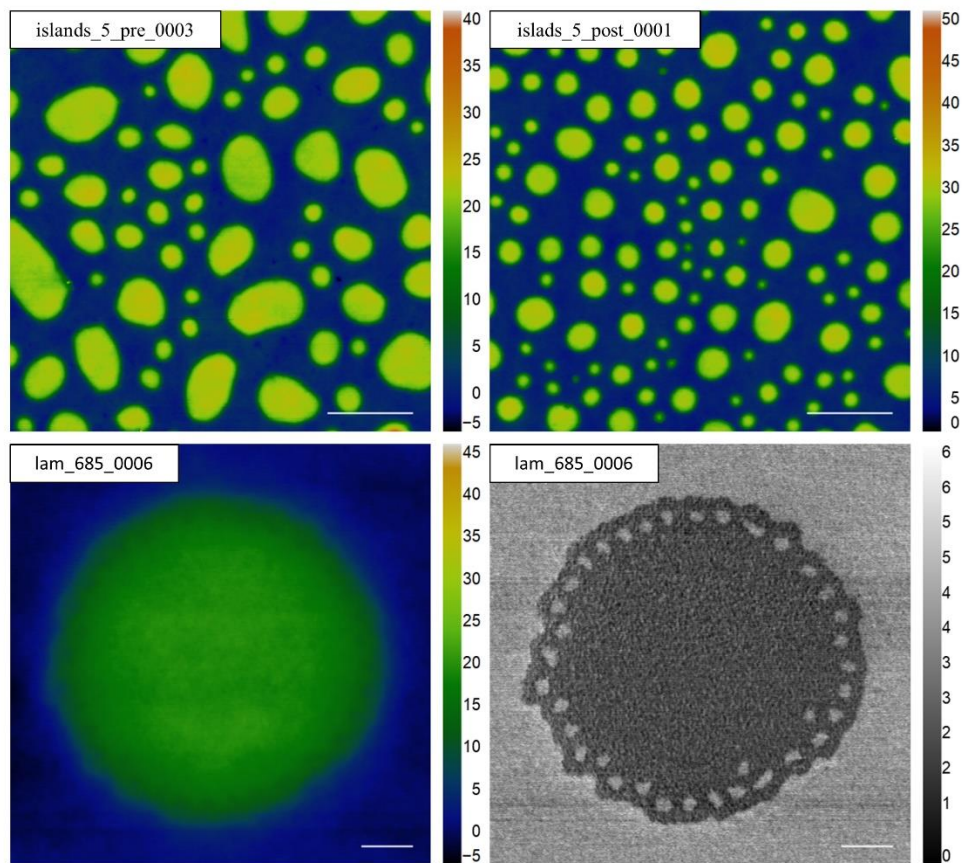
68.5k PS-*b*-PMMA islands in air. Asylum Cypher AFM images of 68.5k MW lamellar PS-*b*-PMMA islands in air. These data were used for **Figure 5.1**, **Figure 5.2**, and **Table 5.2**.

Directory: 170709 and 180505

Filename: islands_5_pre_0003 and islads_5_post_0001 and lam_85_0006

Figure A.5.3
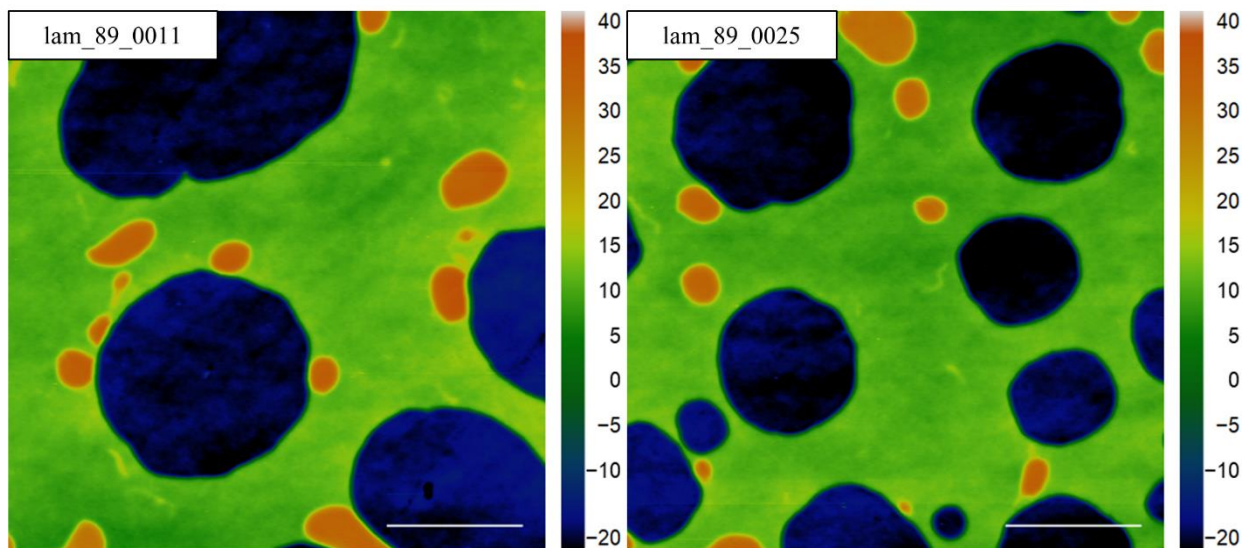
89k PS-*b*-PMMA islands in air. Asylum Cypher AFM images of 59k MW lamellar PS-*b*-PMMA islands in air. These data were used for **Table 5.2**.

Directory: 180108

Filename: lam_89_0011 and lam_89_0025

Figure A.5.4
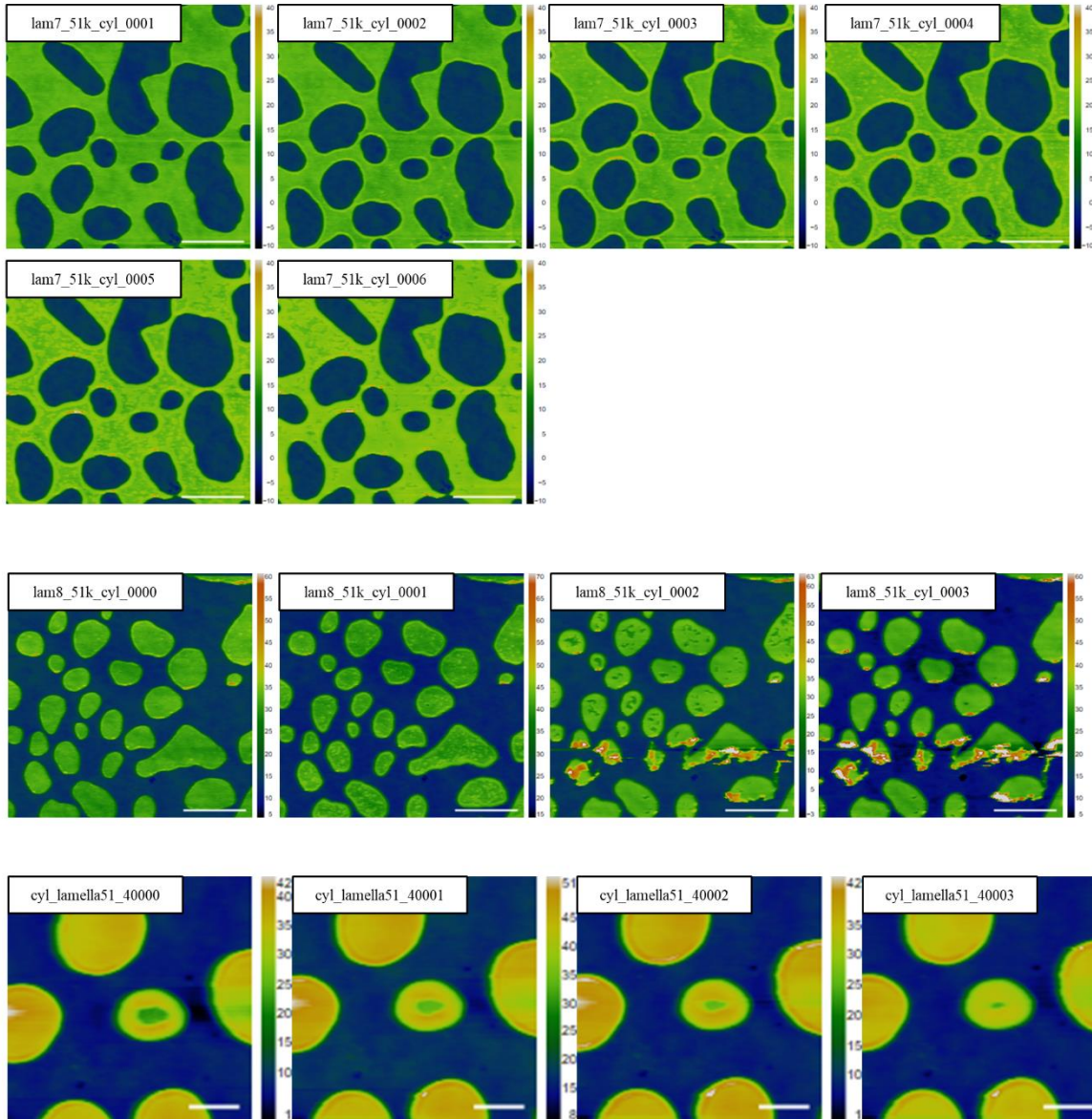
**51k PS-*b*-PMMA island swelling.** Asylum MFP-3D AFM images of 51k MW lamellar PS-*b*-PMMA islands during solvent swelling under cyclohexane. These data were used for **Figure 5.6**.

Directory: 170906 and 150204

Filename: lam7_51k_cyl_0001 – lam7_51k_cyl_0006 and lam8_51k_cyl_0001 – lam8_51k_cyl_0001 and cyl_lamella51_40000 – cyl_lamella51_40003
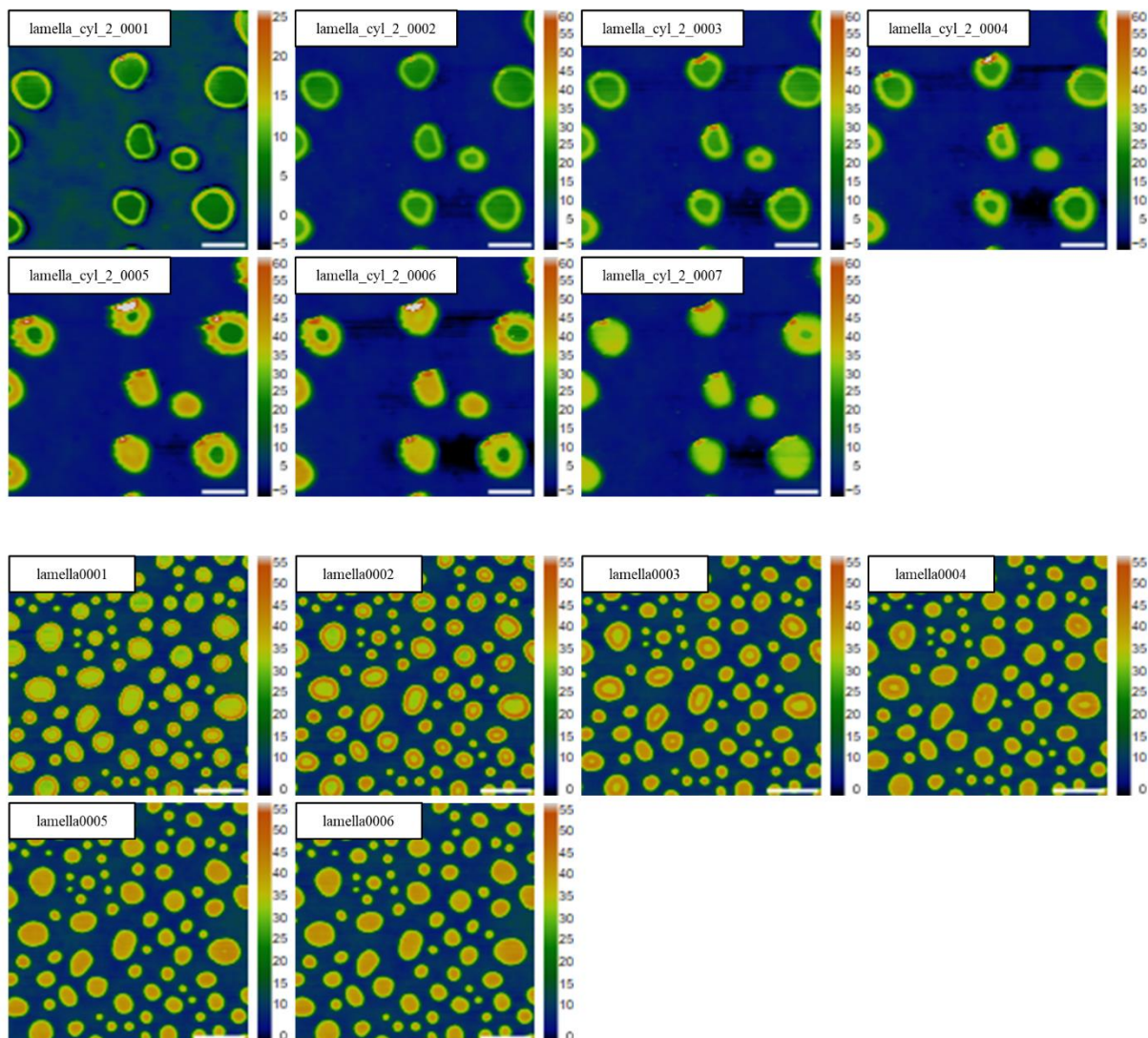
68.5k PS-*b*-PMMA island swelling. Asylum MFP-3D AFM images of 68.5k MW lamellar PS-*b*-PMMA islands during solvent swelling under cyclohexane. These data were used for **Figure 5.2**, **Figure 5.5**, and **Figure 5.6**.

Directory: 141015 and 151030

Filename: lamella_cyl_2_0001 – lamella_cyl_2_0007 and lamella0001 – lamella0006

Figure A.5.6
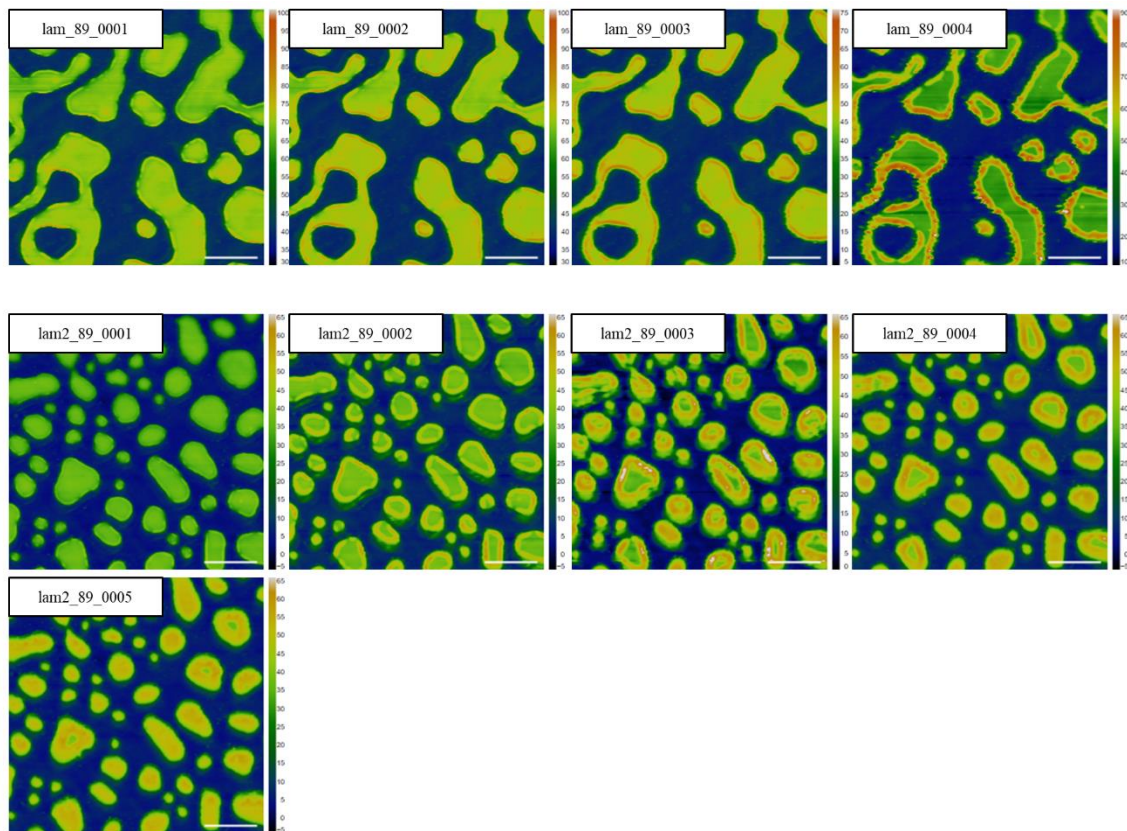
89k PS-*b*-PMMA island swelling. Asylum MFP-3D AFM images of 89k MW lamellar PS-*b*-PMMA islands during solvent swelling under cyclohexane. These data were used for **Figure 5.6**.

Directory: 181001

Filename: lam2_89_0001 – lam2_89_0005 and lam_89_0001 – lam_89_0004

Figure A.5.7
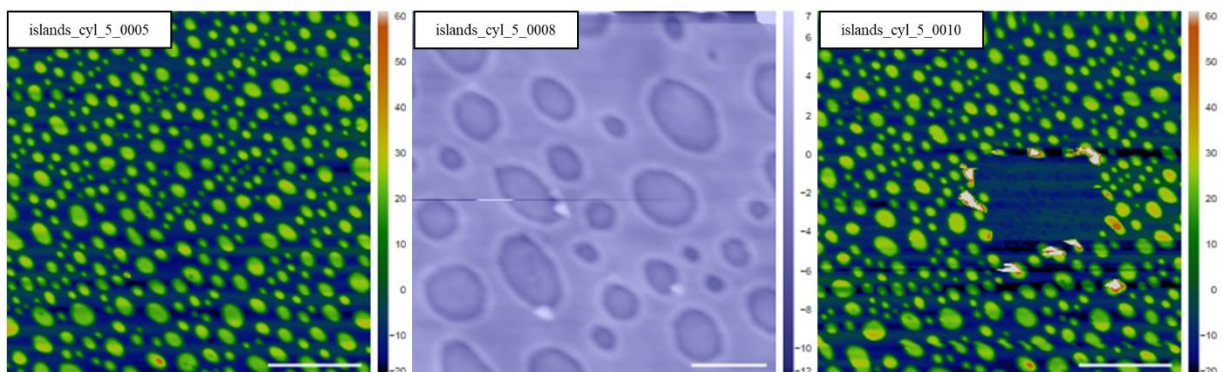
AFM damage of swollen islands. Asylum MFP-3D AFM images of 68.5k MW lamellar PS-*b*-PMMA islands under cyclohexane for AFM tip abrasion experiments. These data were used for **Figure 5.4**.

Directory: 170709

Filename: islands_cyl_5_0005 and islands_cyl_5_0008 and islands_cyl_5_0010

Figure A.5.8
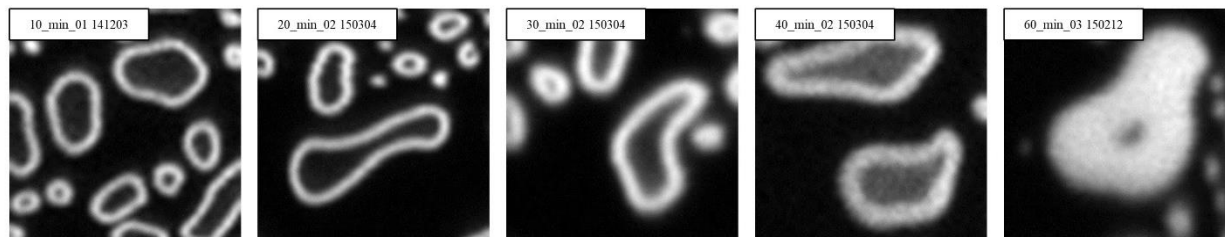
Fluorescent doping of PS-*b*-PMMA islands. Horiba LabRAM Evolution confocal microscopy images of the fluorescent signal of PS-*b*-PMMA islands following immersion in BODIPY-saturated cyclohexane. These data were used for **Figure 5.7**.

Directory: Raman Images

Filename: 10_min_01 and 20_min_02 and 30_min_02 and 40_min_02 and 60_min_03